University of Nevada, Reno

# Investigation of the Ablation and Implosion Phases in 1 MA Wire Array Z-Pinches with UV and X-ray Diagnostics

A dissertation Submitted in Partial Fulfillment of the Requirements

for the Degree of Doctor of Philosophy

in Physics

by

Austin Anderson

Dr. Vladimir V. Ivanov - Dissertation Advisor

May 2015

THE GRADUATE SCHOOL

We recommend that the dissertation
prepared under our supervision by

**AUSTIN ANDERSON**

Entitled

**Investigation of the Ablation and Implosion Phases in 1 MA Wire Array Z-Pinches with UV and X-ray Diagnostics**

be accepted in partial fulfillment of the
requirements for the degree of

DOCTOR OF PHILOSOPHY

Vladimir Ivanov, Ph. D., Advisor

Roberto Mancini, Ph. D., Committee Member

Bruno Bauer, Ph. D., Committee Member

Yasuhiko Sentoku, Ph. D., Committee Member

Sergey Varganov, Ph. D., Graduate School Representative

David W. Zeh, Ph. D., Dean, Graduate School

May, 2015

# Abstract

Z pinches are a class of plasma configuration in which a large electrical current pulse magnetically compresses and confines a cylindrical plasma column. Z-Pinches are the most powerful laboratory producer of X-ray power and energy in the world. They are unstable and inhomogeneous plasma formation, and subject to strong instabilities. Plasma conditions during the ablation and implosion stages can determine the quality of the stagnating Z-Pinch and radioactive properties. New plasma diagnostics were fielded to study the ablation and implosion stages of the Z-Pinch. Experiments were performed using the 1 MA Zebra pulsed power generator and 50 TW Leopard laser at the Nevada Terawatt Facility and the University of Nevada, Reno.

Ultraviolet (UV) laser diagnostics at the wavelength of 266 nm were applied to study the ablation and implosion stages of the wire array Z-Pinch. UV interferometry with an air-wedge differential interferometer was used to measures electron density during the ablation and implosion stage of a wire array Z-Pinch, and measured electron densities up to (1-3) x $10^{20}$ $cm^{-3}$. Faraday rotation was used to measure magnetic fields and derive current distribution in the Z-Pinch during the ablation stage.

X-ray imaging was also fielded to study the wire cores during the ablation stage. The high penetration of the X-rays allows the diagnostic to image the dense solid-liquid wire cores inside the ablating plasma columns in wire array Z-Pinches. Wire cores were backlit by silica He-α spectral line with a wavelength of 6.65 Å, and then imaging with a spherically bent quartz 1011 crystal. Fielding the X-ray imaging couple with UV

shadowgraphy and interferometry allows for the study of Z-Pinch plasma in a wide range of electron density.

X-ray absorption spectroscopy was used to study the electron temperature, ionization stage, and areal density of the plasma in Zebra-Leopard coupled shots. A single ray in aluminum star-like wire arrays was studied during the ablation stage. A samarium backlighting target was struck with the Leopard laser, producing a quasi-continuum emission of X-rays in the 8-9 Å range used for backlighting the wire ray. Two focusing conical spectrometers with mica crystals recorded absorption and reference spectra onto X-ray sensitive film. Absorption spectra was visible in the region of 8.2 - 8.4 Å. Electron temperature was determined using atomic kinetic codes and a two-temperature model of plasma.

# Acknowledgements

First, I would like to thank my advisor Dr. Vladimir Ivanov for his continuous support and for sharing with me his knowledge and insight in plasma research. I am truly grateful for the valuable skills and lessons you have taught me. I'd also like to thank my committee members Dr Roberto Mancini, Dr. Bruno Bauer, Dr. Yasuhiko Sentoku, and Dr. Sergey Varganov.

I am indebted to my numerous professors at UNR, from who I have learned so much in my 5 years here at UNR. I would also like to thank the support staff at the NTF, Alexey Astanovitskiy, Vidya Nalajala, Oleg Dmitriev, Piotr Wiewior, Oleksandr Chalyy, and the numerous student workers that have helped with experiments over the years. I would also like to thank the administrative staff Phyllis Schmidt and Geri Ferguson, without whom nothing would get done, and Dr. Aaron Covington for his continuous assistance.

I'd also like to acknowledge and thank my former and current student colleagues, Daniel Papp, Sara Altemara, Eric McKee, and Bjorn Talbot for their help with experiments and their friendship. I'd like to thank Kim Schultz for her ever-present support, Heman Gharibnejad for the long weeks of studying for classes and the comps, and all the friends I've made during my time at UNR.

I'd like to show my appreciation to my family and friends. I owe everything to my mother and father, Nancy and Michael, and my brother Dallas for their love, patience and support throughout the years.

# TABLE OF CONTENTS

# List of Figures

# Chapter 1

# Introduction

## 1.1 History of Z-Pinches

Z-Pinch refers to a class of plasma in which a large current is driven through the "z" axis, and the J x B force from the resulting magnetic fields compresses or confines the plasma along that same axis. The first analysis of Z-Pinches was performed by W. H. Bennett [Bennett 1934], who published a paper on the equilibrium conditions of a stream of charged particles with a finite temperature in 1934.

Bennett studied a system of charged particles moving with a uniform axial velocity, in which the radial pressure exerted by the confined particles, $\Delta p$, is equal to the J x B force restricting the particles on axis. Using Ampère's circuital law $\Delta \times \mathbf{B} = \mu_0 \mathbf{J}$, and the ideal gas law $p = nkT$ for the confined ions and electrons, he derived what would be known as the Bennett relation,

$$2Nk(T_e + T_i) = \frac{\mu_0}{4\pi} I^2 , \qquad [1.1]$$

where $T_e$ and $T_i$ are the electron and ion temperatures, respectively, and I is current. The formula states the average temperature of the stagnated pinch can be derived by knowing the number density and current strength. In addition, he derived the Bennett equilibrium, which gives the electron density, $n_e$, as a function of radius for a system

of electrons with a spatially uniform axial velocity $v_{ez}$ and no ion movement. This equation is

$$n_e(r) = \frac{n_{e0}}{(1 + br^2)^2}, \quad [1.2]$$

where $n_{e0}$ is the initial electron number, and b is given by

$$b = \frac{n_{e0}\mu_0 e^2 v_{ez}^2}{8k_b(T_e + Z^{-1}T_i)}. \quad [1.3]$$

In the 1950's, Z-Pinches were proposed as a method for controlled nuclear fusion research [Haines]. The proposed fusion method would consist of a deuterium-tritium (DT) mixture that would be adiabatically heated and compressed by the Z-Pinch in the equilibrium state until the reaction was complete. Under the Lawson criterion for fusion [Lawson 1957], this would require electron densities ($n_e$), and time ($\tau$) on the scale of $\tau N_e \geq 1.5 \cdot 10^{20}$ s/m$^3$ for DT fusion. However, it was quickly discovered that magnetohydrodynamic instabilities, such as sausage and kink instabilities, quickly disrupted the stagnated current before fusion could occur.

Research on Z-Pinches at major laboratories was largely abandoned at this point, until the 1970's and 1980's and the development of fast pulse power technology at AWE (Atomic Weapons Establishment) [Martin 1970]. Pulse power machines are powered by a Marx capacitor bank, in which capacitors are charged in parallel and then released in series, allowing for a large voltage multiplication. Pulse power machines take advantage of the fact that over small enough time frames, insulators behave perfectly, making them ideal for short current pulses on the order of a few 100 ns. The new technology allowed for the creation of pinches with power of the order

of 1-300 TW over a typical pinch duration of a 80-250 ns. This made it an efficient experimental platform for creating a large volume of plasma at high energy density.

Currently there are multiple TW scale Z-Pinch facilities located around the world. Sandia National Laboratories has the Z-Machine, currently the most powerful Z-Pinch machine, with 27 MA of current with a rise time of 95 ns, giving approximately 350 TW of power. The Saturn machine, also at Sandia, has a maximum current of 7 MA and a rise time of 100 ns. Three 1 MA pulsed power machines are located in universities. The Nevada Terawatt Facility (NTF) at the University of Nevada Reno features Zebra, formerly named HDZP-II, a 1 MA pulse power generator with 100 ns rise time, which was the pulse power generator used in the research covered in this dissertation. Imperial College in the United Kingdom features MAGPIE, a pulse power generator with 1.4 MA of current with 150 ns rise time. Cornell runs experiments on two pulse power machines: COBRA, with 1 MA of current and 95-230 ns rise time, and XP, with 500 kA of current with a 50 ns rise time.

Pulse power machines are one of the experimental platforms being explored for developing Inertial Confinement Fusion (ICF). Direct methods use the collapse of the Z-Pinch plasma to compress and heat fusion fuel. One such method being research is the Magnetized Liner Indirect Fusion (MAGlif) concept, in which a thin Be cylindrical liner compresses a deuterium-tritium fuel mixture to create fusion [Cuneo 2012]. Indirect methods involve using the radiation from the Z-Pinch to compress and ignite the fusion fuel source, typically with a hohlraum [Sanford 2007, Cuneo 2001].

## 1.2 Wire Array Z-Pinches

Wire array Z-Pinches use fine wires, typically with diameters of 4-25 microns in multi-wire arrays and diameters of 100 microns or more in single wires and X-pinches, in a variety of load geometries. An example of a wire array load is shown in Figure 1.1 (a). The geometry of the load changes the behavior of the implosion dynamics of the pinch, and therefore have different applications in experiments. A few types of load geometries are shown in Figure 1.1. The most common is cylindrical load, shown in Figure 1.1(b), in which the wires are evenly spaced out at the same radius from the center of the load. These loads feature strong and short X-ray pulses. Planar arrays, shown in Figure 1.1(e), consist of wires arranged into a line. Another load is the star-like wire array shown in Figure 1.1(d), in which 3 or more planar arrays extend out radially from the center of the pinch [Ivanov 2008].

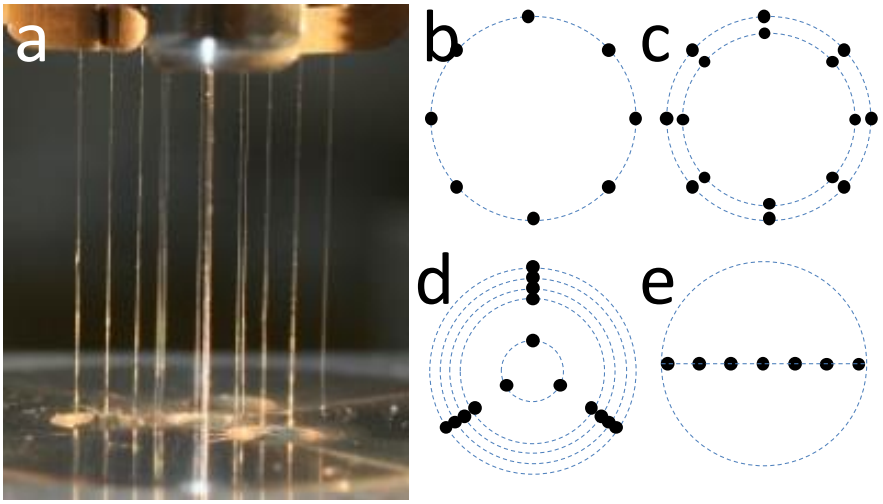


Figure 1.1 (a) Image of a 15 wire array load used in z-pinch experiments. There are many different load geometries, including (b) cylindrical (c) nested cylindrical (d) star-like and (e) linear.

Wire array Z-Pinches are excellent producers of X-ray radiation. At the Sandia National Laboratory, the Z-Machine, an 11 MJ pulse power generator with a 20 MA peak current, used a double nested cylindrical wire array Figure 1.1(c), to produce over 1.8 MJ of X-rays over a 5 ns span, producing the largest laboratory source of X-rays in record, and at a remarkable 15% conversion from electrical energy to X-ray radiation [Deeney 98]. Due to the high efficiency at converting X-rays, many Z-Pinches are used as a driver for X-ray experiments.

## 1.3 Stages in the Wire Array Z-Pinch

Wire Array Z-Pinches have four primary stages. The first is the initiation stage [Sarkisov 1997], in which a current pre-pulse travels through the wire array. This relatively low current, only 5 kA in Zebra generator compared to the peak current of 1 MA, creates the initial ohmic heating of the wires. Surface breakdown and heating forms a low density plasma sheath around the wires which eventually breaks down and the current switches from the wire core to this plasma sheath. This marks the beginning of the second stage, the ablation stage when plasma ablates off the wire cores and begins to get pulled by the global magnetic field [Ivanov 2006, Lebedev 2000], as shown in Figure 1.2(a). The third stage is the implosion stage, shown in Figure 1.2(b), when the wire cores are fully ablated and are pulled into the center of the pinch. Finally there's the stagnation stage, when the imploding plasma collides in the center of the pinch and forms a single plasma column as shown in Figure 1.2 (c).

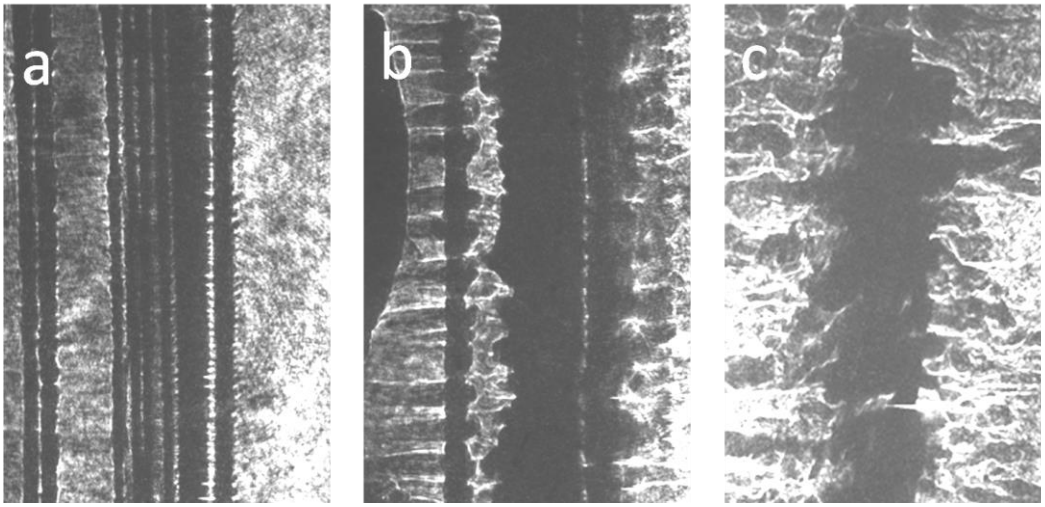


Figure 1.2 Shadowgrams depicting three stages of wire array z-pinch implosions. (a) The ablation stage where plasma is ablating off the wire (b) The implosion stage when the bulk of the wire mass has turned to plasma and is pulled to the center of the pinch (c) Stagnation, where the plasma forms a dense plasma column until instabilities cause it to breakdown and dissipate

### 1.3.1 Ablation stage

The ablation stage of an imploding Z-Pinch occurs near the start of the main Z-Pinch current pulse. At this point the current is mostly confined to plasma sheath surrounding the wire cores. The current pulse causes the wires to ohmically heat, and the plasma core of the wire expands to 3-8 times its initial diameter. This wire core is surrounded by a hot expanding coronal plasma, which ablates off the surface of the wire core. The current creates a global magnetic field in the azimuthal direction, perpendicular to the wires and the current flow, and the resulting **J** x **B** force pulls the ablated coronal plasma towards the center of the Z-Pinch. The current is concentrated in the region just surrounding the wire cores, which remain stationary during this process. The ablating plasma is continually replenished from the wire core by the

radiation of the hot corona plasma. Many wire arrays accumulate the ablated plasma into a column of plasma, known as the precursor plasma, into the center of the Z-Pinch [Lebedev 2000, Ivanov 2007a].

In linear and star-like arrays, ablation begins on the edge wires, which are subjected to the largest global magnetic field. When the start of the implosion stage occurs for the outer wires, the inner wires are still in the ablation stage and remain in their initial position. In cylindrical arrays, the symmetric distribution of the wires causes all wires to ablate over a similar time scale.

The mass removal rate for the ablating plasma can be described by using the Rocket model [Lebedev 2001a]. For a wire core of radius $R_0$ and ablated plasma with constant ablation velocity $V_{abl}$, momentum balance gives the rate of mass removal from the cores as

$$\frac{dm}{dt} = -\frac{\mu_0 I^2}{4\pi R_0 V_{abl}}. \qquad [1.4]$$

The ablation velocity $V_{abl}$ depends heavily on material, current and wire array radius.

According to semi-empirical theory [Lebedev 2001a], the core-coronal plasma structure of the ablating Z-Pinch leads to the development of instabilities. Periodic perturbations can be seen in the ablating plasma. These perturbations are typically of 0.4 mm to 0.5 mm in aluminum and 0.2-0.25 in tungsten. The wire core size determines the spatial scale of these instabilities, which seed development of Rayleigh-Taylor instabilities in the implosion stage.

### 1.3.2 Implosion stage

Once the wire cores have exhausted their mass from the plasma ablation, breaks in the plasma column begin to form along the axis. The wire cores then start to implode towards the center of the pinch. This implosion is characterized by large plasma bubbles which form at the implosion front and accelerate towards the center of the pinch [Ivanov 2007b]. The implosion plasma bubbles are seeded by the periodic axial perturbations seen in the ablation stage. These bubbles collide with ablated plasma which has filled the inner volume of the Z-Pinch during the ablation stage, and pushes the newly accumulated plasma into the center of the z-axis, in a manner characterized as the “snow plow” model of implosion [Lebedev 2002].

For cylindrical wire arrays, the axial perturbations of 0.4 mm to 0.5 mm in Al merge to form a larger bubble 3-5 times larger during the implosion stage [Lebedev 2000, Ivanov 2007b]. These bubbles expand radially and axially, radially distributing a significant portion of the mass of the wire array and transporting it towards the center of the pinch. The implosion of these bubbles leave behind streams of trailing mass, which contain a significant portion of the plasma of the wire array. The bulk of the trailing mass doesn't implode onto the axis until the stagnation stage.

In contrast to cylindrical wire arrays, linear and star-like wire arrays feature "cascading" implosions [Ivanov 2007b]. Implosion bubbles form on the edge wires, and accelerate towards the center of the pinch. The bubbles from the outer wires collide with the plasma columns formed by the inner wires, and implosion bubbles form anew, effectively resetting the axial instability growth. This causes the

imploding plasma to arrive on axis with axial perturbations with a shorter periodic scale, which helps to mitigate large scale MHD instabilities and improve X-ray yields.

Nested cylindrical wire arrays, which are two concentric cylindrical wire arrays with different diameters, have two implosion modes. In the non-transparent, or hydrodynamic mode, the plasma from the outer wires collide with the plasma from the inner wires, then merge and implode together. Similar to cascading implosions, this decreases instability growth and improves X-ray yields [Sanford 1996].

The transparent mode for nested cylindrical arrays occurs when plasma from the outer cylindrical array implodes and passes through the inner array without interacting. The current then switches to the inner wires, which then begin to ablate. This results in a two-stage implosion, with the plasma from the outer wires imploding slightly before the plasma from the inner wires [Sanford 1996]. This effect occurs in nested cylindrical arrays with low wire numbers and large interwire gaps on MA scale machines, or in nested wire arrays with large wire numbers of 100 or more on higher current machines such as the Z-Machine and Saturn, where the inner wire array is effectively Faraday screened by the outer wire array.

### 1.3.3 Stagnation stage

The final stage is the stagnation stage, in which the plasma forms a dense column. Plasma is compressed and confined on the Z-axis by the **J** x **B** force, and is heated by the conversion of kinetic energy. During this stage the majority of Z-Pinch radiation is created. Three types of radiation free-free, free-bound, and bound-bound.

Free-free radiation, or Bremsstrahlung continuum radiation, is formed by the deflection of charged particles, typically electrons deflected by ions. The change in direction results in a loss of kinetic energy, which is emitted as a photon. Free-bound continuum radiation is caused by the capture of a free electron into an empty orbital of an ion. The difference between the free electrons kinetic energy and the bound state energy determine the energy of the photon. Variations in the electron's energy prior to recombination creates the continuum effect.

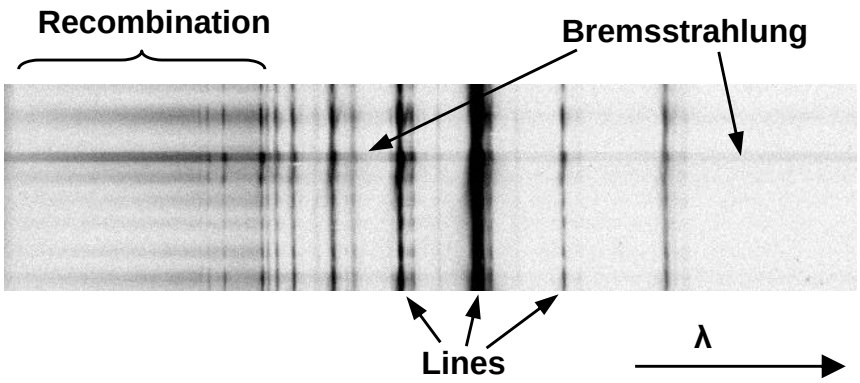


Figure 1.3. X-ray spectrum from stagnation stage of Z-pinch, depicting regions of spectral lines, electron recombination, and Bremsstrahlung radiation.

Bound-bound linear radiation is caused by an electron transitioning from a higher energy bound state to a lower energy one. For both the free-bound and bound-bound radiation, the ionization state of the atom determines the energy of the radiation. Low atomic numbers elements, such as aluminum and magnesium, have lower ionization thresholds, which causes higher levels of ionization (Z=10-11), allowing for more K-shell emission than heavier elements such as copper or stainless steel. In 1-MA pulse power machines, heavy elements, such as gold and tungsten, typically

have no K-shell radiation, and only radiate in M-shell and L-shell. Figure 1.3 shows emission spectrum recorded from the stagnation stage, showing the three types of radiation. The bound-free or recombination radiation occupies shorter wavelengths than the bound-bound spectral lines, due to a free electron having more energy than a bound electron.

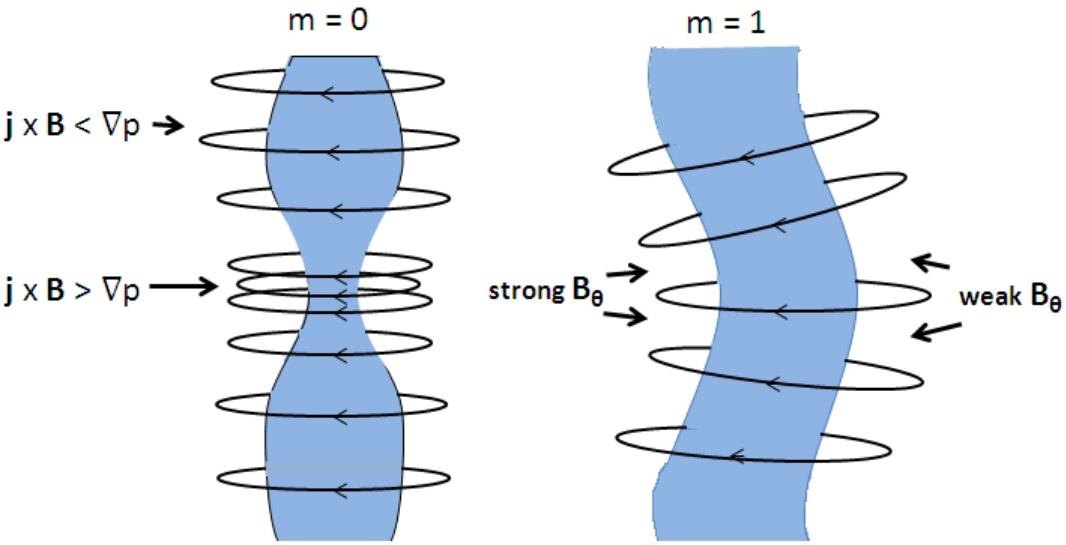


Figure 1.4. Two of the most common MHD instabilities. The m=0, or sausage instability, thin necks in the plasma column have a larger **j** x **B** force, which further compresses the neck and increases the force further. In the m=1, or kink instability, a bend in the plasma column increases the magnetic field on the concave side and weakens it on the convex side, pushing the column out and increasing the bend.

The stagnation stage persists until instabilities destroy in the plasma column. Two of the most common instabilities are the magnetohydrodynamic (MHD) m=0 sausage instabilities and m=1 kink instabilities, shown in Figure 1.4. Theory states that sausage instabilities form on the plasma column from azimuthal perturbations along the axis. Small necks of plasma condense the current and produce stronger **j** x **B** force, which in turn compress and squeeze out plasma, resulting in a smaller neck

until the column breaks. Kink instabilities are caused by a bend in the shape of the plasma column. The bend condenses the magnetic field on the concave side, causing it to push the bend of plasma column further out until it breaks the plasma column. In the real Z-Pinch, instabilities are induced onto the pinch during the implosion stage. A Z-Pinch is formed initially inhomogeneous and instabilities grow on this inhomogeneous plasma column.

## 1.4 Zebra pulsed power generator at UNR

The Zebra generator located at NTF has a peak current of 1 MA with a 100 ns rise time [Bauer 1999], or up to 1.6 MA using a Load Current Multiplier (LCM)


Figure 1.5. The Zebra generator at the NTF facility.

[Chuvatin 2009]. An overhead view of the Zebra generator can be seen in Figure 1.5.

The Marx capacitor bank comprises of 32 1.3 µF capacitors, stored in a mineral oil tank acting as an insulator. These capacitors are typically charged to 85 kV, with a total stored power of 150 kJ. The Marx SF6 gas switches are triggered by a TG70 high voltage pulse generator. The capacitors are discharged in series, so the individual electric potential across each capacitor is combined together, resulting into one high-voltage discharge. The next stage is intermediate storage, which is a 27 nF water capacitor. This capacitor helps compress the current pulse shape. This

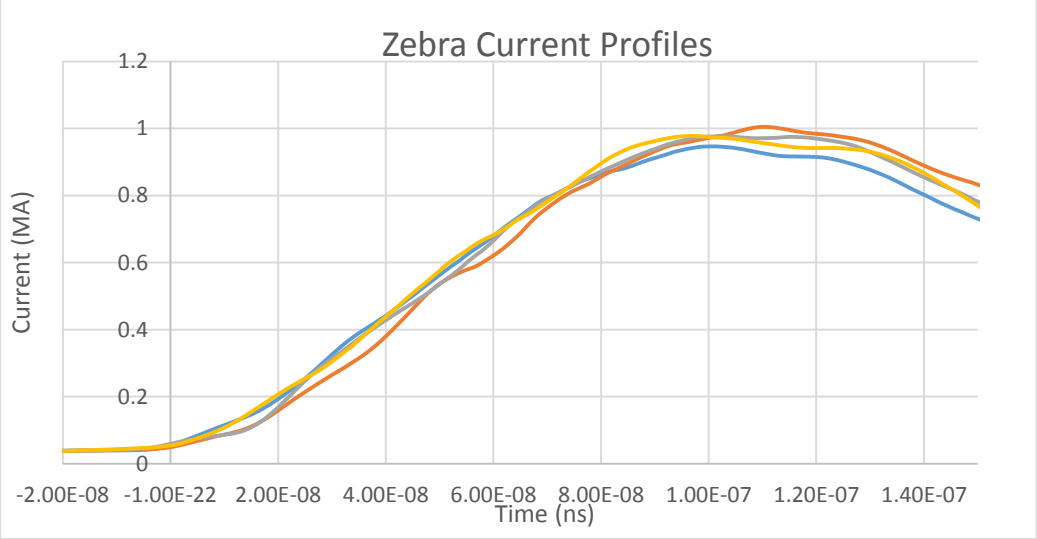


Figure 1.6. The current profiles for Zebra shots #3343-#3346. The current profile is reproducible during the 0-100 ns rise time.

intermediate storage is also triggered by a gas switch. The next stage is a 300 ns water-transmission line, with an impedance of 1.9 Ω, triggered by a self-breaking water switch. A short Magnetically Insulated Transmission Line (MITL) transports the current pulse to the experimental chamber. The current passes through the wire array which connects the anode to cathode, typically separated by 1-2 cm, and then

dissipates out through the chamber [Bauer 1999]. The reproducibility of the Zebra current profile over the course of four consecutive shots is shown in Figure 1.6.

## 1.5 Leopard Laser at UNR

The Leopard laser is a 1057 nm diagnostic laser for coupled laser-Zebra experiments. It is a high intensity hybrid Ti:Saphhire / Nd:glass laser capable of operating in two modes, 40J with a .6 nspulse length, or 12J with a .35 ps pulse length. The presence of both a Z-Pinch generator and high energy laser greatly expands experimental capability for high energy

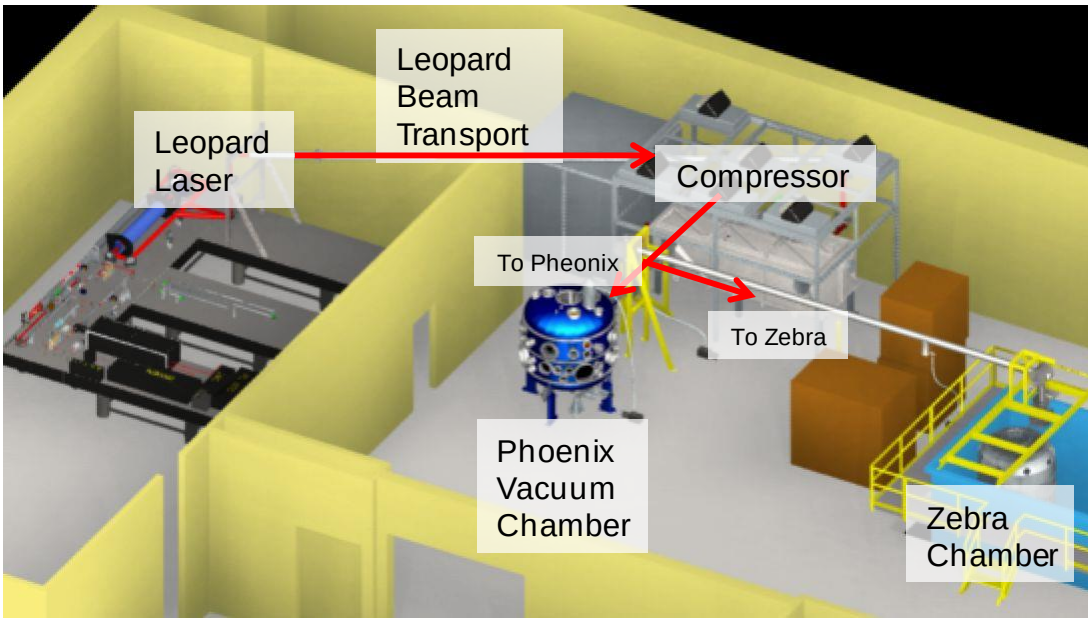


Figure 1.7. Leopard beam path to Zebra and Phoenix Vacuum Chambers. Leopard can be directed into a dedicated Phoenix Vacuum chamber for Leopard only experiments, or into the Zebra Chamber for Zebra-Leopard coupled experiments

density physics. The Leopard laser can be relayed into the Zebra chamber for Z-Pinch coupled laser experiments, where the Leopard laser can be used as a driver for several diagnostics, such as in X-ray backlighting, X-ray absorption spectroscopy, proton

radiography. It can also be used to study laser interaction with exotic environments created by the Zebra machine, like strongly magnetized plasmas or plasma jets. In addition, it can be used with the Phoenix vacuum chamber to do stand-alone intense laser plasma experiments [Wiewior 2010]. The Leopard beampaths for Phoenix and Zebra experiments is shown in Figure 1.7.

The Leopard laser Ti:Sa oscillator creates pulses 80 fs in duration, and is optically

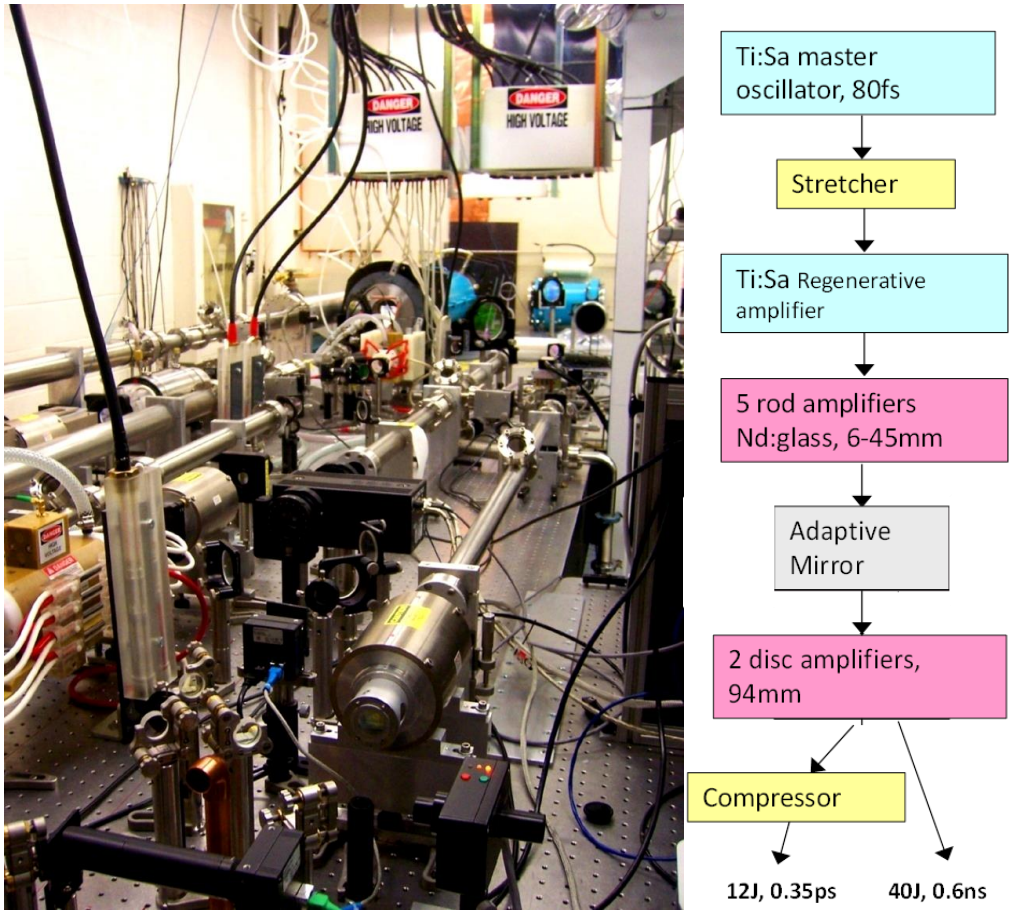


Figure 1.8. Leopard Laser and accompanying schematic of components. Two modes are possible, a short-pulse mode with a 0.35ps laser pulse with 12J of energy, and a long-pulse mode which bypasses the compressor, resulting in a 40J, 0.6 ns pulse.

pumped with a 9.2 W CW Nd: YVO3 laser. The oscillator pulses are then amplified using chirped pulse amplification techniques. Chirped pulse amplification allows lasers to reach intensities which would otherwise exceed the tolerance for the amplifiers. This is accomplished by first stretching the pulse duration, decreasing the overall intensity, then amplifying it, and then recompressing the pulse. In the Leopard laser, a Offner-type stretcher increases the oscillator's pulse duration from 80 fs to 1.3 ns. It is then amplified by a Ti:Sa regenerative amplifier to an energy of 1.2 mJ. The pulse is further amplified by 5 rod amplifiers made of Nd:glass, ranging from 6mm to 45 mm in diameter, and by two 94 mm disc amplifiers. Faraday isolators and Pockels cells separate the amplifiers, preventing back reflection and improving contrast ratio of the beam. After amplification, an adaptive mirror corrects the wavefront of the pulse. At this point a compressor can reduce the pulse duration of 0.35 ps and 12 J of energy, or the compressor can be bypassed, resulting in a pulse duration of 0.6 nswith 40 J of energy. Figure 1.8 shows a picture of the Leopard laser, and a diagram of the different stages of the Leopard laser.

For Zebra-Leopard coupled shots, the short 100 ns current rise-time for the Zebra generator makes having accurate timing between the two machines an important issue. Zebra has a jitter of about ±20 ns, caused by the breakdown of the gas switch for the Marx capacity bank. The Leopard laser is much more consistent, on the order of a couple nanoseconds, but due to a long delay time in the regenerative amplifiers of approximately 1 μs, Leopard has to be triggered before Zebra is triggered, and so the Zebra-Leopard jitter is caused primarily by the breakdown of the gas switch in Zebra. Zebra swing arm initiates the trigger, which sends a firing signal to the Leopard laser, which after a 1

second programmed delay, sends a signal back to the Marx TG70 gas switch pulser to trigger Zebra.

## 1.6 Zebra Core Diagnostics

The NTF facility offers a suite of core diagnostics for experiments in the Zebra generator. Core diagnostics represent diagnostics native to NTF and available to all researchers. These include B-dot probes, fast X-ray detectors, bolometers, laser and optical diagnostics, and X-ray imaging and spectroscopy diagnostics.

### 1.6.1 B-Dot Probes

The Zebra current is calculated using three pairs of B-dot probes located within the Zebra chamber. B-dot probes are small loops of wire, which are used to measure the time-varying magnetic field inside the chamber. The time derivative of the magnetic field in the B-dot probe induces an electric field along the wire according to the Maxwell-Faraday equation

$$\nabla \times \mathbf{E} = -\frac{\partial \mathbf{B}}{\partial t}. \qquad [1.5]$$

The coil gives an output voltage that is proportional to the cross-sectional area, number of loops, and the time derivative magnetic field, or "B-dot", hence the name. Integrating the B-dot signal gives the magnetic field strength as a function of time, allowing for the calculation of the Zebra pulse current as a function of time as seen in Figure 1.5.

### 1.6.2 Fast X-ray Detectors and Bolometers

Core diagnostics for the Zebra pulse power generator include fast X-ray detectors located in a five-channel head attached side-on to the Zebra chamber. This five-channel head measures X-ray yields of the Z-Pinch using absolutely calibrated X-ray Diodes (XRDs) Photoconductive Detectors (PCDs), and a bolometer.

Ni and Au bolometers are used to measure the total emission of radiation in the range of 10 eV to 5 keV. The bolometer is a thin strip of metal, 200 microns thick, with a voltage bias applied across the strip. The resistivity of the metal strip changes linearly with the energy of the absorbed photons. The change in resistance at a known current results in a voltage drop, which can be used to calculate the energy of absorbed radiation.

An X-ray Diode (XRD) is a carbon photocathode with a anode mesh, which measures the photoionization of electrons from incident X-rays to measure the X-ray radiation yields from the wire array Z-Pinch plasmas [Spielman 1995]. The spectral response of the XRD depends heavily on photon energy, as well as surface quality of the photocathode, thus requiring frequent replacement and cleaning during experiments. The time response for XRDs is less than 500 ps. Kimfol and Kapton filters can be attached to the XRD to limit the sensitivity of the diagnostic with certain wavelengths.

Diamond Photoconductive Detectors (PCDs) are an X-ray detecting diagnostic with a flat spectral response that is linearly dependent on the incident photon energy in the range of 10 eV to 6 keV [Spielman 1995], which offers an advantage compared to XRDs. The time response is approximately 200 ps, making it slightly faster than XRDs

as well. A 8mm Be filter can be attached to cut off soft X-rays with energy below 1 keV, limiting its detection to hard X-rays in the 1 keV to 6 keV range.

### 1.6.3 Laser and Optical Diagnostics

A 532 nm Nd:YAG commercial laser from the company EKSPLA, with a pulse duration of 150 ps and energy of 80 mJ, is available as a core diagnostic for the Zebra generator. The short pulse duration and easily adjustable timing allows it to be used as a probe in all stages of the Z-Pinch. This laser also works in a 266 nm regime by using another frequency doubling crystal. The 266 nm diagnostics are not a core diagnostic, and are covered in detail in chapter 2. Laser diagnostics used to study Z-Pinch plasma include 4-frame shadowgraphy, interferometry, Faraday rotation diagnostics, and Schlieren interferometry at 532 nm. "Core" laser diagnostics are shown in Figure 1.9.

An in-depth analysis for shadowgraphy, interferometry and Faraday rotation diagnostics is given in Chapter 2. Briefly, in shadowgraphy the plasma is backlit by the laser. The plasma absorbs and refracts the laser, leaving shadows on the image which reveal the structure of the plasma. Interferometry is used to measure the phase shift of the beam after traveling through the plasma in order to derive the electron density of the plasma. Different types of interferometers can be used, such as Mach-Zender and shearing interferometers. Faraday rotation diagnostics can be used to measure the magnetic field of the pinch. Schlieren Interferometry measures the gradient of the electron density of a plasma. A knife-edge blocks the primary beam path of the unaltered

laser beam, allowing only the refracted beams to pass.

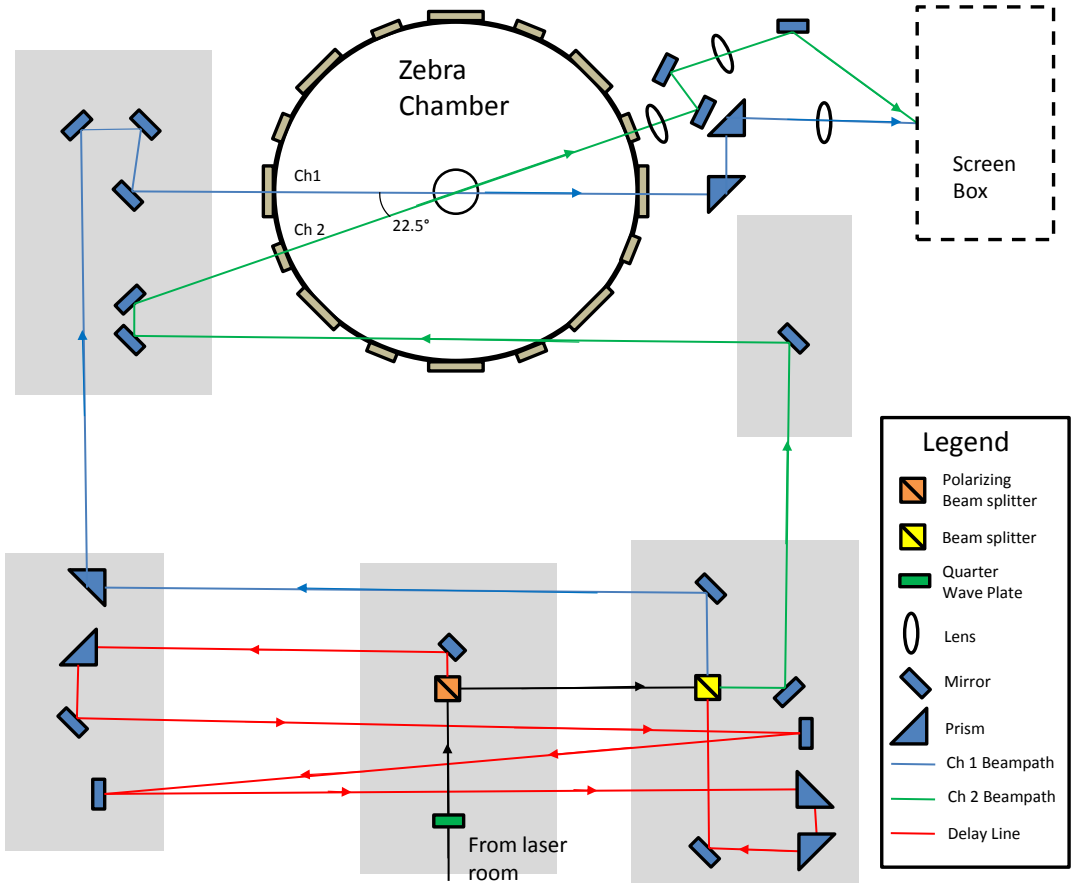


Figure 1.9. Schematic of a 2-frame 532 nm laser beam path for Zebra Chamber Channel 1 and Channel 2. The beam comes into the Zebra lab from the laser room which houses the EXSPLA 532 nm laser. A quarter wave plate circularly polarized the light. A polarizing beam splitter splits the laser into two separate, linearly polarized beams. The primary beam (black) then travels to a beam splitter, which splits the beam into Channel 1 (blue) and Channel 2 (green). The secondary beam travels along the delay line (red) before recombining with the original beam, giving each channel two perpendicularly polarized pulses which are later separated by polarizers inside the diagnostic screen box.

An Intensified Charged-Coupled Device (ICCD) system is available to measure low intensity emission. A multi-channel plate (MCP) is shown in Figure 1.10, and it is composed of tiny fused glass channels, each of which act as a photomultiplier tube. A large voltage is applied on the plate front-to-back. Photons emitted from the plasma strike

the front of the plate, and photoionize electrons inside the channels. Secondary electrons are created and accelerated by the voltage difference. These tubes isolate the electrons, transferring the image from the front of the plate onto the back of the plate. Electrons are converted to photons by the phosphor plate. This allows for a large increase in sensitivity while still maintaining high spatial resolution of 10-20 μm, which is useful for low intensity emissions such as plasma self-emission during the implosion stage. A CCD camera then records the emission.

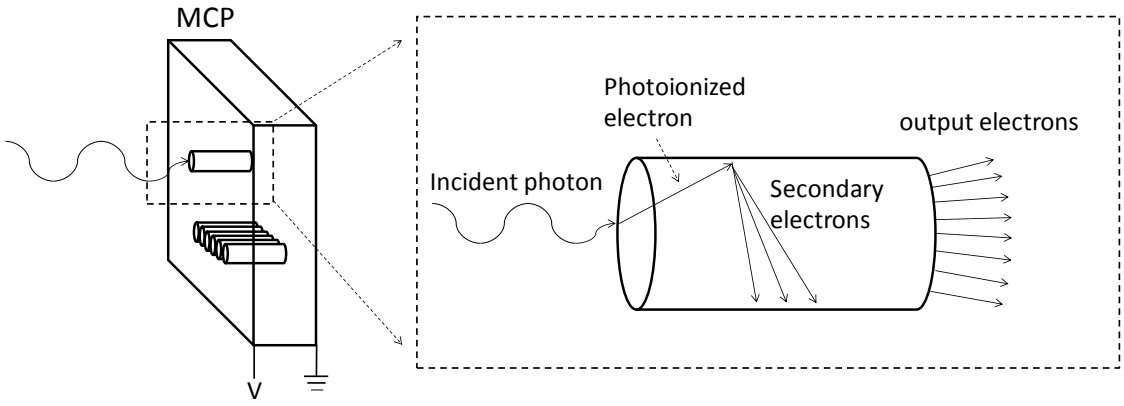


Figure 1.10. Multi-Channel Plate (MCP) schematic. An incident photon strikes a single tube of the MCP. The tube acts as a photomultiplier, creating multiple secondary electrons which exit the back-end. The tube confines the electrons within the cell, preserving spatial resolution.

An optical streak camera is a diagnostic to study the 1-D temporal profile of Z-Pinch emission through a slit. A photocathode converts incident photons to photoionized electrons, which accelerate down the cathode tube. These electrons pass through two plates which generate a time-varying electric field, which deflect the electrons and sweep them across a phosphor screen. This converts the temporal profile of the photon pulse into a spatial profile of the electrons swept across the surface of the detector.

### 1.6.4 X-ray Pinhole Imaging

A pinhole camera is the simplest imaging system, consisting of a single aperture which creates an image. The main advantages of pinhole cameras are their durability, a near infinite depth of focus, and the ability to image X-rays, as there are currently no lenses that can image X-rays. The magnification M of a pinhole camera is given as the ratio of q/p, where p is the object to pinhole distance, and q is the pinhole to detector distance. The resolution limit Δl for a pinhole of diameter D can be determined using the formula [Hecht 2002]

$$\Delta l = \frac{p}{p+q} D \,. \qquad [1.6]$$

The resolution can be increased by decreasing the diameter of the pinhole, or increasing the magnification. The diameter can only be decreased until circular diffraction limits become a concern. This occurs when the wavelength of the light becomes a significant fraction of the diameter of the pinhole. The Rayleigh criterion for diffraction-limited resolution of a circular aperture is given by [Hecht 2002]

$$\Delta l = 1.22 \, \frac{q\lambda}{D} . \qquad [1.7]$$

A six-frame time-gated pinhole X-ray imaging system is available as a diagnostic, using an MCP as detector. Six gold photocathodes are located on the surface of input side of the MCP. A sheet with six pinholes is placed so that the image created by each pinhole is on a photocathode. Gating is achieved by sending a voltage pulse across each plate sequentially. Imaging is only possible in locations where the voltage is present.

The 6 frames have a variable duration of 1-6 ns. The channels in the MCP have a diameter of 10-12 microns, resulting in a spatial resolution of approximately 50 microns.

### 1.6.5 X-ray Emission Spectroscopy

X-ray emission spectroscopy is used to measure electron temperature and density of plasma in the stagnated Z-Pinch. The stagnation stage of the Z-Pinch highly ionizes plasma of light elements, such as Al, resulting in K-shell emission. The intensity of the individual K-shell spectral lines depends on the electron temperature and density, which can be calculated using atomic codes such as PrismSPECT.

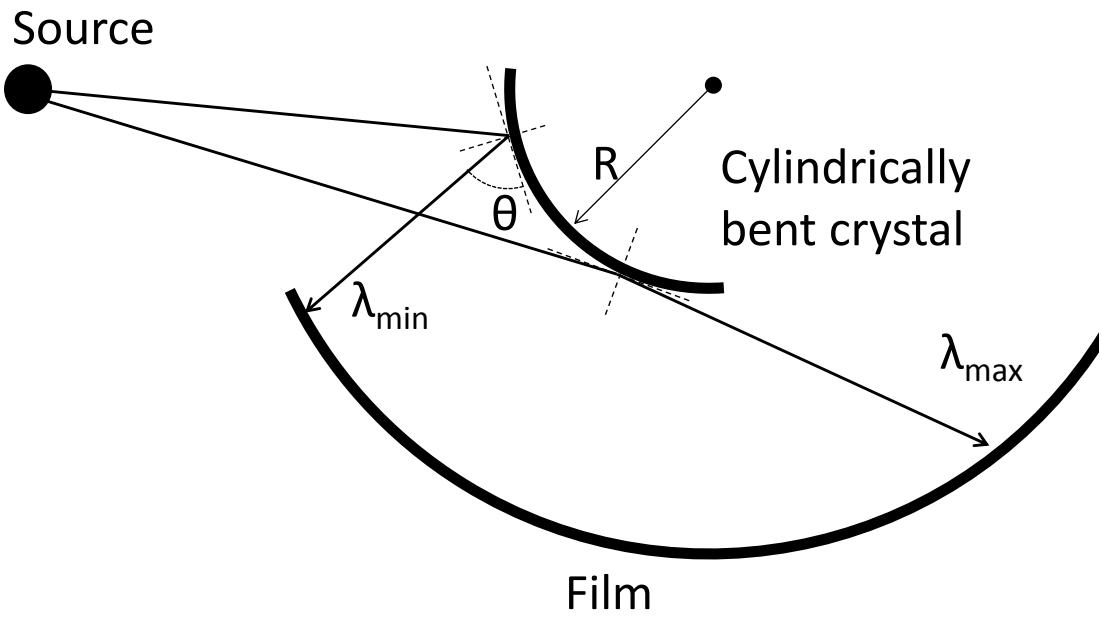


Figure 1.11 X-ray spectrometer using cylindrically bent crystal

A time-integrated convex KAP (potassium acid phthalate) crystal spectrometer, shown in Figure 1.11, is used to measure X-ray emission. The crystal has a radius of

curvature 25.4 mm and a interplanar spacing of 2d =26.6 Å. Spectral dispersion is achieved using Bragg crystal diffraction. Bragg diffraction for an X-ray incident on a crystal is given by

$$m \cdot \lambda = 2d \sin\theta\,, \qquad [1.8]$$

where d is the spacing of the planes in the crystal lattice, θ is the angle of incidence, λ is the wavelength, and m is a positive integer representing the order of diffraction. The crystal uses first order (m=1) Bragg diffraction. Convex crystal spectrometers have the advantage of having wide spectral range in comparison to flat or concave crystal spectrometers, capable of working with X-rays with wavelengths of approximately 2d to almost 0, due to the large variation in angle of incidence.

## 1.7 Van Hamos Spectrometer

The van Hamos spectrometer is a spectrometer which uses focusing geometry to increase the collection efficiency of the spectrometer, making it ideal in situations with small X-ray sources with low intensity. The spectrometer features a concave crystal, which uses Bragg X-ray diffraction (Eq. 1.8). The geometry of the crystal collects X-ray emissions from a point source located on the cylindrical axis of the crystal and focuses them onto that same axis.

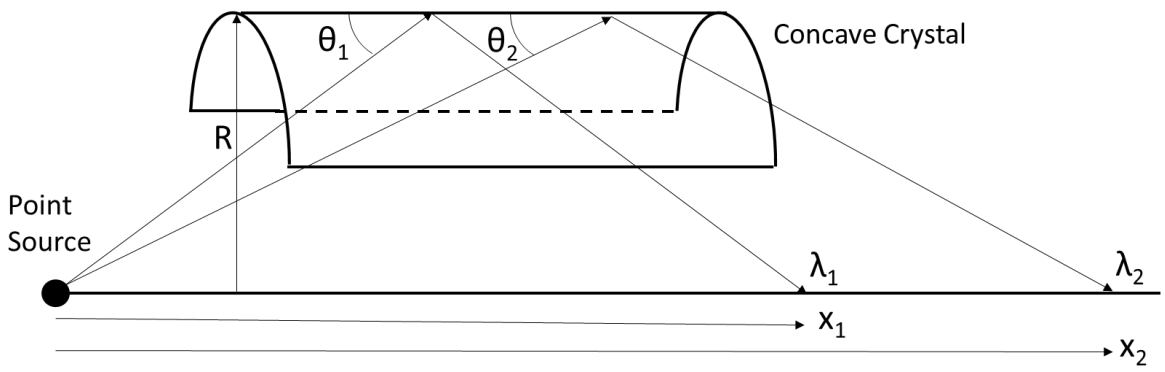


Figure 1.12 Schematic for van Hamos crystal spectrograph using a cylindrically bent concave crystal

The distance x from the souce to the image is given by the equation

$$x = 2R\cot\theta = 2R\sqrt{(\frac{2d}{n\lambda})^2 - 1}, \quad [1.9]$$

where R is the radius of curvature of the crystal, θ is the angle of incidence, d is the spacing of the planes in the crystal lattice and λ is the wavelength [Shevelko 1998].

The spectral resolution δλ is limited by three contributors, the width of the rocking curve, the broadening caused by a finite source (as opposed to point source), and finally from astigmatism. The resolution of the spectrometer is defined as the lowest resolution of the above contributors. The resolving power of the spectrometer limited by the width of rocking curve is given by

$$\frac{\lambda}{\delta\lambda} = \frac{\tan\theta}{\delta\theta}, \quad [1.10]$$

where $\delta\theta$ is the width of rocking curve of the crystal. The broadening of a finite source of size a gives a resolving power of

$$\frac{\lambda}{\delta\lambda} = \frac{2R}{a \cdot \sin\theta \cos\theta}. \quad [1.11]$$

And finally, the resolving power limited by astigmatism is given as

$$\frac{\lambda}{\delta\lambda} = \frac{2R}{\Delta x_1 \cdot \sin\theta \cos\theta} \quad [1.12]$$

Where $\Delta x_1$ is an effective width caused by the astigmatism. In most cases with a quasi-point source, the spectral resolution is limited by the finite source size [Shevelko 1998].

# Chapter 2

# Investigation of Ablation and Implosion Stages of Wire Array Z-Pinches using UV Laser Diagnostics

## 2.1 UV Laser Diagnostics

The effectiveness of a laser-based diagnostics for probing plasmas is limited by several factors. In order for a laser to propagate through a plasma, the electron density must be below the theoretical limit defined as the critical density. For EM wave propagation through a plasma, the dispersion relation is given as [Hutchinson 2002]

$$kc = \sqrt{\omega - \frac{n_e e^2}{\varepsilon_0 m_e}}. \tag{2.1}$$

When the term inside the radical becomes negative, light no longer propagates through the plasma, and instead becomes evanescent and exponentially falls off as it gets absorbed and reflected from the boundary $n_e = n_c$. The density at which this occurs for a given wavelength of laser is given by

$$n_c = \frac{4\pi^2 \varepsilon_0 m_e c^2}{e^2 \lambda^2}. \tag{2.2}$$

This is known as the critical density, and is the theoretical maximum electron density for a laser propagating through a plasma.

However, for practical purposes, the electron density limit for laser light propagation is typically much lower than the critical density. Strong plasma density gradients, often seen in Z-Pinch produced plasma refract laser light. If this refraction

angle is larger than the acceptance angle of the optical scheme, the light is lost. The refraction angle θ for a 1-dimensional plasma gradient can be written as [Hutchinson]

$$\theta = \int \frac{1}{\eta}\frac{d}{d\eta}\eta(x,y) = \frac{1}{\eta}\left(\frac{\Delta\eta}{\Delta y}\right)l\,, \qquad 2.3$$

where η(x,y) is the refraction index as a function of position x and y, and l is the interaction length in the y direction.

In addition to refraction, there are three types of absorption which can also affect laser transmission. Bound-bound absorption involves the absorption of a photon by a bound electron, which causes the electron to leap to a higher energy bound state. These spectral lines have discreet energy levels which are determined by the energies of the quantum states of atoms, and can be affected by Doppler, Stark, and Zeeman broadening. Bound-bound absorption is only of concern if the spectral lines of atoms are at the same as energy as the probing laser. For highly ionized plasmas, absorption lines are typically in the X-ray range.

Bound-free continuum absorption occurs when a bound electron absorbs a photon with enough energy that it escapes the bound state and becomes a free electron, thus ionizing the atom. This requires that the energy of the photon is higher than the energy of the bound state of the atom. This range is also typically in the X-ray range for highly ionized plasmas.

For high energy density plasmas, the limiting factor for laser light transmission is often determined by a third type of absorption, known as inverse Bremsstrahlung absorption, or free-free absorption. This occurs when a free electron absorbs an

incoming photon. In the absence of other charged particles, an electron would oscillate with the frequency of the laser beam. In a steady state, there is no transfer in energy from this interaction. However, in the presence of other charged particles, the electron interacts with nearby charged particles, which interrupts the oscillation of the electron and converts the photon energy into kinetic energy. This inverse Bremsstrahlung is modeled by the equation [Johnson 1973]

$$T = e^{-\gamma L}, \tag{2.4}$$

where T is the transmission, L is the length of the plasma, and $\gamma$ is the Bremsstrahlung constant, which is given as

$$\gamma = 8.73 \cdot 10^{-30} \cdot \lambda^2 \frac{n_e^2 \cdot Z \cdot \Lambda}{T_e^{3/2}(1 - \frac{n_e}{n_c})^{1/2}}, \tag{2.5}$$

where Z is the ionic charge, and $\Lambda$ is the Coulomb logarithm. The inverse Bremsstrahlung absorption depends on electron temperature, unlike the critical density which depends only on density. This dependence on temperature is important for high energy density plasmas, like in a typical Z-Pinch. The Bremsstrahlung absorption constant scales as $\sim\lambda^2$ of the laser. The advantage of using a shorter wavelength laser to decrease Bremsstrahlung absorption motivated upgrading 1064 nm Nd:YAG laser at the NTF facility from the 2$^{nd}$ harmonic of 532 nm to the 4$^{th}$ harmonic of 266 nm.

The effects of that upgrade can readily be seen in the shadowgraph in Fig 2.1. Shadowgraphy is a laser diagnostic technique in which the plasma is backlit by a laser beam and difference in opacity for different regions of the pinch is imaged. In the 532 nm image on the left, the stagnated Z-Pinch is seen as a large opaque column. In the 266

nm image on the right, the shorter wavelength laser allows the inner structure of the denser plasma to become studied. Kink and sausage instabilities not seen in the 532 nm image are plainly visible.

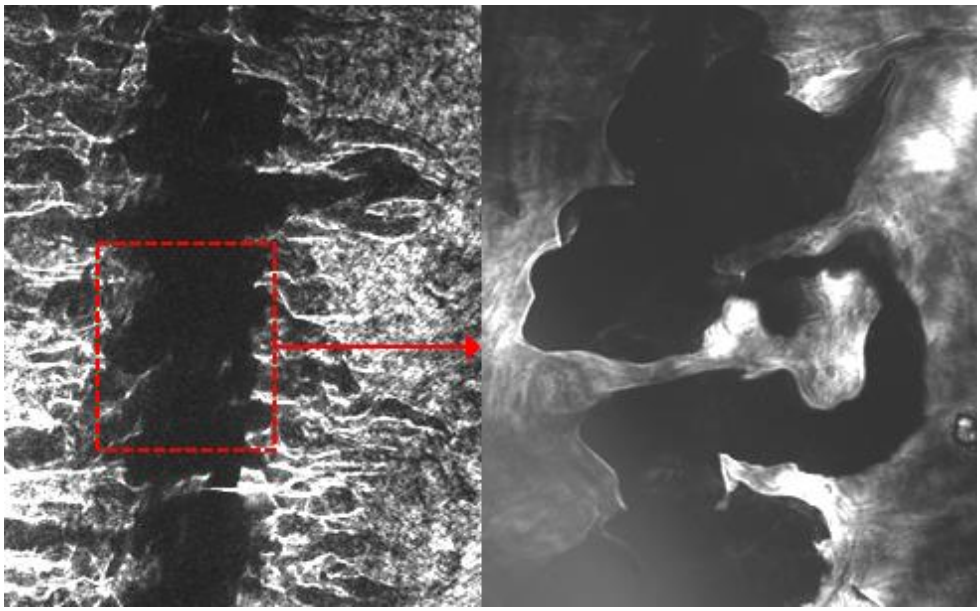

Fig. 2.1 (a) Shadowgram of stagnating z-pinch using 532nm probing laser. (b) Shadowgram of boxed area using 266nm probing laser. The inner structure of denser plasma is visible, revealing kink instabilities not seen with the 532 nm laser [Ivanov 2011a].

The UV laser probe also has the ability to create effective interferometry and Faraday rotation diagnostics for dense Z-Pinch plasmas. Interferometry allows measurement of the electron density, $n_e$, of a plasma. The Faraday rotation diagnostic is a 3-channel system capable of measuring the magnetic field strength, when coupled with a shadowgraphs and interferometry.

### 2.1.1 UV Interferometry

UV interferometry was developed to study the electron density of the Z-Pinch. In addition to lower Bremsstrahlung absorption, laser interferometry at the wavelength of 266 nm allows for the measurement of denser plasmas than 532 nm laser interferometry. The phase shift of an interferometric fringe in a plasma slab is given by a line integral in Gaussian units [Hutchinson 2002]

$$\varphi = \frac{c}{4\pi\lambda n_c}\int n_e \cdot dl = \lambda \cdot 4.46 \cdot 10^{-14}\int n_e \cdot dl\,, \qquad 2.6$$

where $\varphi$ is the phase shift in fringes (i.e. units of $2\pi$), $\lambda$ is the laser wavelength and $n_e$ is electron density per $cm^3$. As plasma density increases, interference fringes become thinner and the distance between fringes decreases. At high enough densities, fringes may not be able to be spatially resolved by optical apparatus, resulting in lost fringes and loss of information, even if the transmittance of the probing laser in that plasma is high. A shorter wavelength laser probe results in a smaller phase shift, allowing for higher electron densities to be measured. This effect makes 266 nm laser interferometry more appropriate for higher density plasmas than 532 nm laser interferometry.

The type of interferometer used in the experiments covered by this dissertation was an air-wedge shearing interferometer [Sarkisov 1996]. A schematic is shown in Figure 2.2. The interferometer is made of two quartz wedges, which are slightly offset resulting in an "air wedge" forming between them (see Figure 2.2). A lens (or lens system) in front of the wedge allows for imaging. This type of interferometer has a couple of advantages as a diagnostic for dense plasmas. First, the air-wedge shearing

interferometer is a differential interferometer, which is sensitive to the slope of the phase shift of a wavefront, and is therefore less sensitive to dense plasmas than an interferometer which measures the absolute phase shift, such as the Mach-Zender interferometer. In addition, it's a common path interferometer, so the probing laser requires only a single beam path to use.

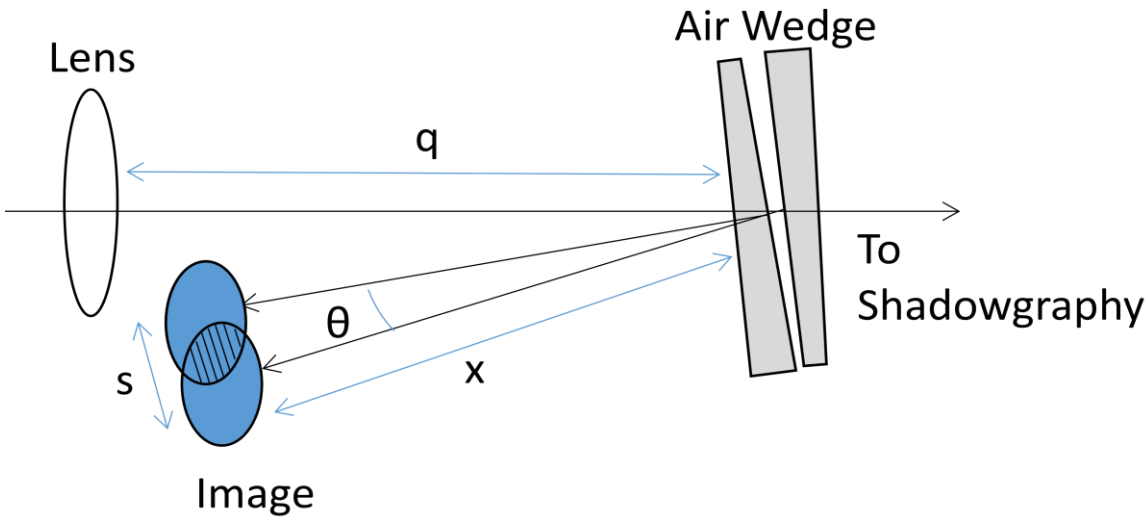


Figure 2.2 Optical schematic for air-wedge interferometer. Two glass wedges, offset at an angle θ, form an air-wedge in the center. The two reflections from the inner air wedge create two images offset at a shearing distance of s, which provides the differential interference fringes. The initial beam passes through the air wedge, allowing it to be used for other laser diagnostics.

The air wedge interferometer measures the differential phase shift, which is the difference in phase between two overlapped images. In Figure 2.3, two identical phases are offset by a distance s. The difference between the two phases, $\varphi(y)$ and $\varphi(y-s)$, is the differential phase $\Delta\varphi$.

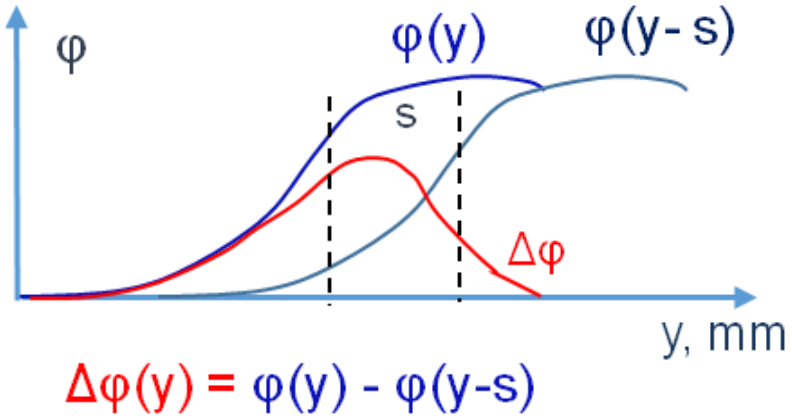


Figure 2.3. Two identical phases offset a distance s. The difference between the two phases ϕ(y) and shifted phase ϕ(y-s) create a differential phase shift Δϕ.

Once the differential phase shift is discovered, the absolute phase shift can be determined. The absolute phase shift φ at a point y can be determined by taking the differential phase shift Δφ at that point, and adding it to the known absolute phase shift at a distance equal to the shear distance s away,

$$\varphi(y) = \varphi(y - s) + \Delta\varphi(y). \qquad 2.7$$

This requires at least one known phase shift to start, and so at least one unaltered fringe is necessary to define a known absolute phase shift of zero. An example of this is shown in Figure 2.4. The phase (blue line) is recreated using differential phase (red line). The origin represents the location of the unshifted reference fringe. At the first shear distance, φ(s) and Δφ(s) are identical. At the second shear distance 2s, the value of the Δφ(2s) is added to φ(s) to determine φ(2s). This process is repeated to derive the absolute phase shift for the entire span of the measured differential phase shift.

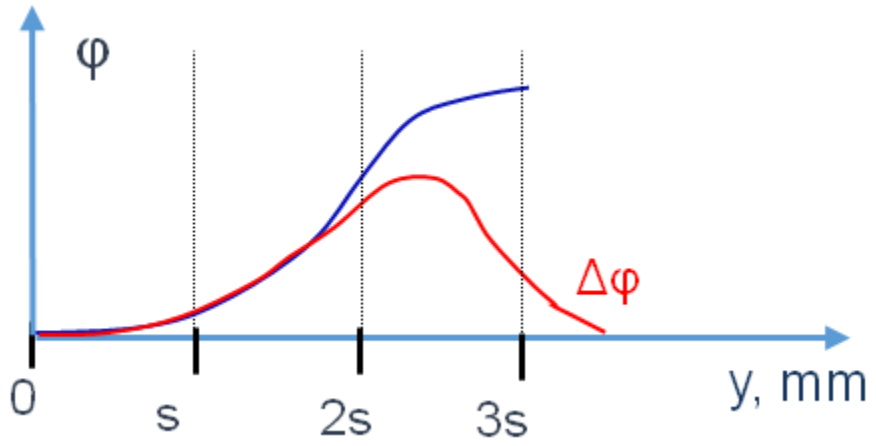


Figure 2.4. Reconstructing absolute phase ϕ using differential phase Δϕ. The phase ϕ at a point y is determined by adding the Δϕ at y to the ϕ at (y-s)

Differential phases measured at less than one shear length give the absolute phase shift, which can be taken advantage of by increasing the shear length to larger than the area of interest, but at the cost of losing the reduced sensitivity of differential interferometry.

The air-wedge has three main reflections. The first reflection is from the front face of the first glass wedge, the second is from the gap in the air wedge, which used as the interferometer, and the last is the back face of the second glass wedge. The wedge shape provides an angle difference between the inner air wedge reflections and the two reflections on the faces of the wedges. This creates a spatial separation between the beams used for imaging and the reflections off the face of the air-wedge interferometer. The angle and distance of the air wedge to the image plane determines the initial phase separation for interference fringes and the spatial shearing distance between the first and second reflected beam in the air wedge. For small angles, the spatial separation s

between the two images, also known as shear distance, is given by the formula [Sarkisov 1996]

$$s = 2\theta\,[(q - x) - F)]\,, \tag{2.8}$$

and the distance between fringes is given by

$$d_f = \frac{\lambda\,(q - F)}{2\theta \cdot x}\,, \tag{2.9}$$

where $\lambda$ is the wavelength of the probing laser, $\theta$ is the angle of the air wedge in radians, F is the focus length of the lens, q is the distance from the lens to image plane, and x is the distance from the wedge to image plane (see Figure 2.2).

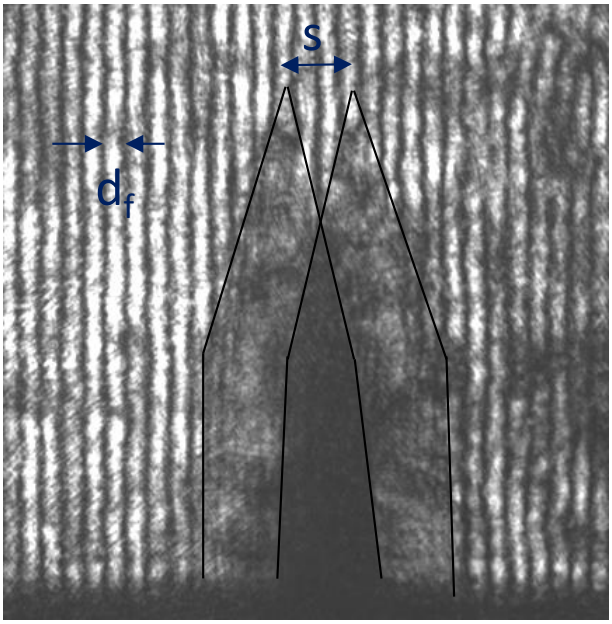


Figure 2.5. Air-Wedge shearing interferometer reference image using a single needle. Shown is fringe spacing $d_f$ and the shear distance s as measured from needle tip to needle tip

Reference images with a needle are used for two purposes. First, the needle is located at the location of the Z-Pinch, so it is also used as a reference to align the optical

system. Second, the reference image can be used to measure the shear distance and fringe distance directly. Figure 2.5 shows a sample reference image. The distance between the two needle points provides an easy method to measure the shear difference.

The procedure for measuring the differential phase shift is shown in Figure 2.6. First, a reference image is taken, which gives us the position of the wires and the distance, $d_f$, between the unaltered fringes. The locations of these reference fringes are

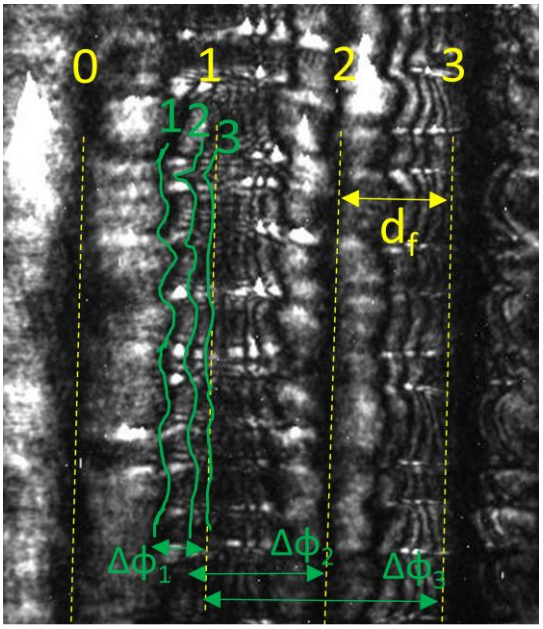


Fig. 2.6 Fringe counting. Yellow dotted lines represent pre-shot reference fringes locations with spacing $d_f$. Green lines are traces of thefringe locations during the shot. Differential phase shift $\Delta\phi$ is determined by measuring the distance to its reference fringe location and dividing by $d_f$.

shown by the yellow dotted line. An image taken during the experiment is then lined up with the reference image, and unaltered fringes are discovered. These unaltered fringes are required in order to give an initial absolute phase shift of zero which can be used as a starting point. In figure 2.6, the unaltered fringe is labeled as "0". Starting from the

unaltered fringe, fringes are then outlined for visibility and numbered in ascending order. In Figure 2.6, the first 3 fringes are traced with green lines. The locations of these fringes are then compared to the locations of the respective reference fringes, which is also counted starting from the unaltered fringe. The distance between a fringe and its reference, when the distance normalized to units of $d_f$, is the same as its differential phase shift, given in units of $2\pi$.

After recreating the phase shift, electron density can be determined using Abel inversion transformation with equation 2.6. The Abel inversion assumes cylindrical symmetry, making the electron density a function of radius only. The geometry makes this technique appropriate when the plasma is roughly cylindrical in shape, such as during the ablation and stagnation stage of a Z-Pinch.

The Abel transformation is derived as follows. For the a cylindrically symmetric function, f(r), and a second function F(y), which is the original function f(r) integrated from -∞ to +∞ in the x direction at the location y, are related by

$$F(y) = \int_{-\infty}^{\infty} f\left(\sqrt{x^2 + y^2}\right) dx = 2\int_{0}^{\infty} f\left(\sqrt{x^2 + y^2}\right) dx\,. \qquad 2.10$$

For a position y, by substituting

$$dx = \frac{rdr}{\sqrt{r^2 - y^2}}, \qquad r = \sqrt{x^2 + y^2}\,, \qquad 2.11$$

and changing the integration limits appropriately, the result is the forward Abel transform

$$F(y) = 2\int_{y}^{\infty} \frac{f(r)\, r\, dr}{\sqrt{r^2 - y^2}}. \qquad 2.12$$

The inverse Abel transform allows one to calculate f(r) given F(y), and it's given as

$$f(r) = -\frac{1}{\pi}\int_{r}^{\infty} \frac{dF(y)}{dy}\frac{dy}{\sqrt{y^2 - r^2}}. \qquad 2.13$$

Referring to equation 2.6, the line integral $\int n_e \cdot dl$ follows the path of the Abel transform, so assuming a cylindrically symmetric electron density, we can compare $n_e(r)$ to f(r) and $\varphi(y)$ to F(y) in equation 2.12. and 2.13. We derive, in Gaussian units, the phase as

$$\varphi(y) = \frac{e^2\lambda}{\pi m_e c^2}\int_{y}^{R_0} \frac{n_e(r)\, r\, dr}{\sqrt{r^2 - y^2}}, \qquad 2.14$$

and the electron density as

$$n_e(r) = -\frac{2m_e c^2}{e^2\lambda}\int_{r}^{R_0} \frac{d\varphi(y)}{dy}\frac{dy}{\sqrt{y^2 - r^2}}. \qquad 2.15$$

A limit of the inverse Abel transformation is that it requires a smooth phase shift curve. A small discontinuity in the derivative of $d\varphi(y)/dy$ can cause the value $n_e(y)$ to blow up at that point. Because of this, the phase is smoothed out before processing.

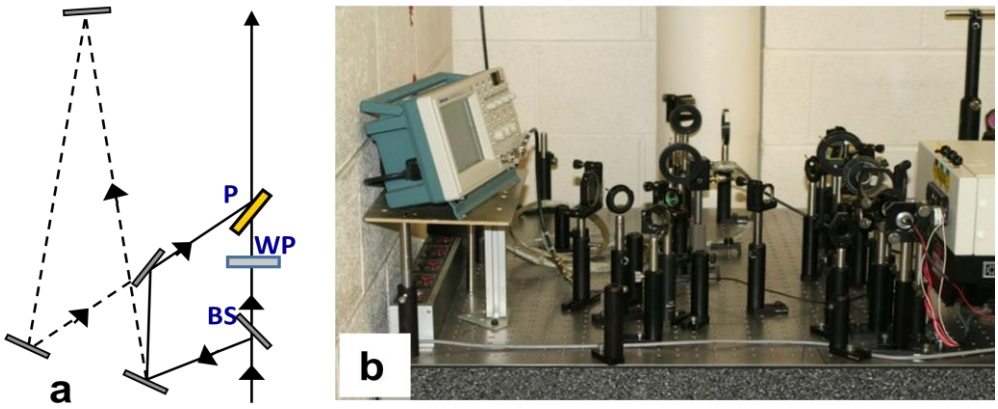


Figure 2.7. (a) Schematic for 266 nm delay line with a Beam-Splitter (BS) Wave-Plate (WP) and Polarizer (P). The beam splitter splits the delay line off the main line. Two possible delay paths are shown, one in the solid line, and a longer delay in the dotted line. (b) Photograph of the delay line.

To study the evolution of the electron density profile, it's useful to be able to measure the electron density of the plasma at two time frames. This was accomplished by adding a delay line to the UV channel as shown in Figure 2.7. A quarter wave plate followed by a polarization splitter divides the beam into two paths. One of the split beams travels around an additional optical path length, then recombines with the primary beam. This effectively creates two pulses with two orthogonal polarizations travelling through the chamber along the same optical path but with a customizable delay of several ns.

To separate the two polarized beams, two schemes were created. The first scheme, used polarizers in front of two CDD cameras, which separated the two beams by blocking the beam with the incorrect polarization. However, the Al mirrors used in the optical system depolarized the 266 nm laser beams, resulting in strong loss of contrast. A second scheme used a birefringent calcite crystal wedge after the chamber to separate the

two orthogonal polarizations of the laser beam. A birefringent crystal, such as calcite, has a index of refraction which depends on the polarization of the light. This angularly separates the two orthogonal components of the laser beam. A knife edge is also used to block any extra reflections caused by the mirrors.

### 2.1.2 UV Faraday Rotation Diagnostics

Another UV laser diagnostic developed uses the Faraday rotation of a polarized beam of light to measure the magnetic field of the wire array Z-Pinch. A polarized laser beam traveling through uniform plasma in the presence of a magnetic field will undergo a rotation in the polarization of the electric field according to the equation

$$\beta = \frac{e^3\lambda^2}{2\pi \cdot m_e^2 c^4} \int_0^L B_x(x) n_e(x) dx\,, \tag{2.16}$$

where $\beta$ is the Faraday rotation angle, *e* is the elementary charge, $m_e c^2$ is the electron's rest energy, $B_x(x)$ is the magnetic field component along the direction of propagation for the laser, and $n_e(x)$ is the electron density per $cm^3$. If one knows the electron density $n_e$, from interferometric techniques, magnetic field strength can be determined using the Abel inversion (eq 2.13) of the above equation to get

$$B(r) = \frac{r}{n_e(r)} \frac{2\pi \cdot m_e^2 c^2}{e^2\lambda^2} \int_r^{R_0} \frac{d}{dy} \frac{\beta(y)}{y} \frac{dy}{\sqrt{y^2 - r^2}}. \tag{2.17}$$

The experiment set-up for the Faraday rotation diagnostic used a three-channel UV polarimeter, shown in Figure 2.8. The polarimeter takes a shadowgram, interferogram, and Faraday image at one moment in time. First, a UV Glan prism polarizes the incident 266 laser beam prior to wire array Z-Pinch chamber. A thin calcite

crystal wedge is used as the second polarizer. It is set-up after the chamber, and is rotated a small angle $\alpha_0$ in respect to the polarization angle for the Glan prism. This rotation allows us to measure the direction of the rotation caused by the Faraday effect, in order to determine the direction of the magnetic field. The calcite crystal wedge splits the orthogonal polarizations into two angularly separated beams. One beam goes to the shadowgram channel, and the second goes to the Faraday channel. The shadowgram channel is split off to an interferometry channel, featuring an air-wedge shearing interferometer to measure electron density in plasma using the interferometry techniques listed in the previous section.

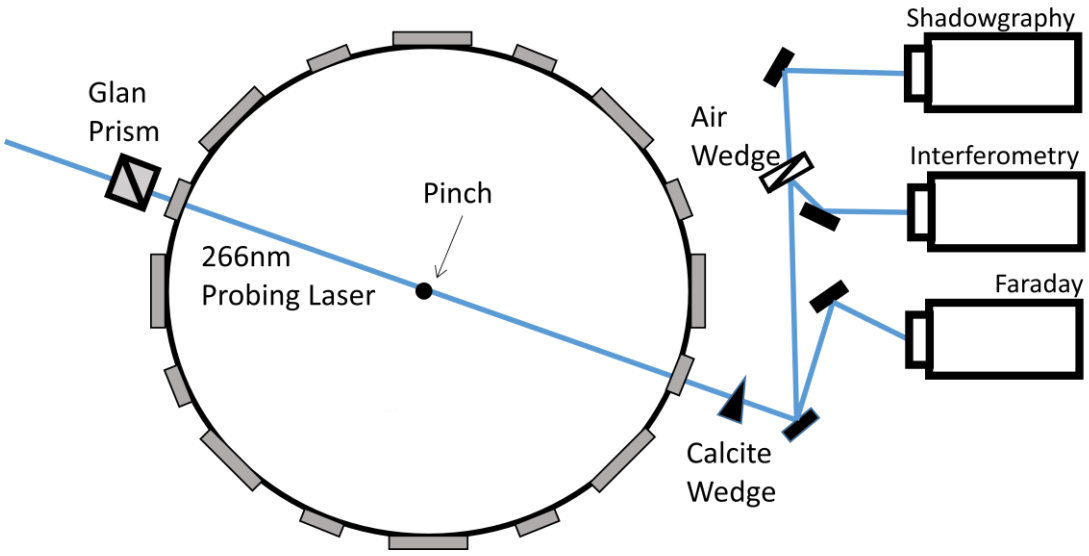


Figure 2.8. Schematic for 266 nm Faraday diagnostic. A UV Glan prism polarizes the beam before it enters the chamber. After the chamber, a crystal wedge separates the two orthogonal polarizations. One beam goes to shadowgraphy and interferometry channels, and the other goes to the Faraday channel.

The Glan prism and crystal wedge are aligned so that in the Faraday channel they act as crossed polarizers, so intensity scales as $\sin^2\beta$, and the shadowgram channel's

intensity scales as $\cos^2\beta$, where $\beta$ is the Faraday rotation angle. The Faraday rotation angle is small, and so in the small-angle approximation, intensity of the Faraday rotation scales as $\beta^2$, whereas the intensity of the shadowgram scales as $\cos^2(1-\beta)$ which is ~1. This allows us to better measure small differences in Faraday rotation angle.

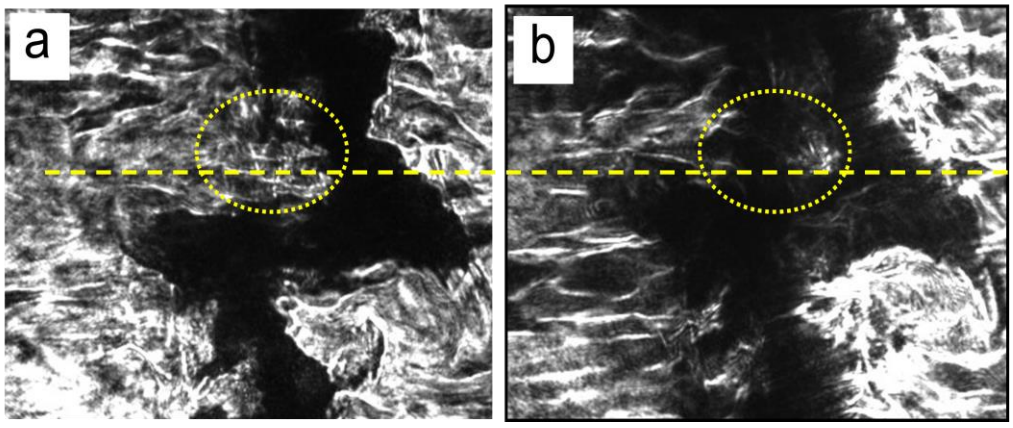


Figure 2.9. (a) Shadowgram and (b) complementary Faraday image at the wavelength of 266 nm. The yellow circle shows the region of darkening caused by the Faraday effect.

In order to preserve the direction of the magnetic field, an additional angle $\alpha_0$ is introduced between the Glan prism and crystal wedge. This modifies the Faraday intensity as $\sin^2(\alpha_0 \pm \beta)$. The plus and minus refer to magnetic fields parallel or anti-parallel to the propagation of the laser. This creates a lightening and darkening effect on the Faraday image, which can be seen by comparing the shadowgram and Faraday images in Figure 2.9(a )and Figure 2.9(b), respectively. Care should be taken to ensure $\alpha_0$ is greater than $\beta$.

The intensity of the shadowgram and Faraday image can be modeled as

$$I_F = I_0 * \sin^2(\alpha_0 \pm \beta + K) * K_F * T(x)\,, \quad 2.18$$

$$I_s = I_0 * K_S * T(x)\,. \quad 2.19$$

Where $I_F$ and $I_S$ are the intensity of the Faraday image and shadowgram, respectively, $I_0$ is the intensity of the laser, $K_F$ and $K_S$ are the attenuation factors for the neutral density filters in the optical paths of the Faraday image and shadowgram, and T(x) is the transmission rate through the plasma. The K is the polarimeter contrast. In this system, the polarimeter contrast is $10^{-4}$, and makes a negligible contribution.

For the reference images, if the filters are kept constant, the intensities of the image are

$$I_{Fref} = I_{0ref} * \sin^2(\alpha_0 + K) * K_F\,, \quad 2.20$$

$$I_{Sref} = I_{0ref} * K_s\,, \quad 2.21$$

where $I_{Fref}$ and $I_{Sref}$ are the intensity of the Faraday image and shadowgram, respectively, for the reference shot, and$I_{0ref}$ is the intensity of the laser during reference shot. Equations 2.18 through 2.21 can be combined into a single equation

$$\frac{I_F}{I_S} * \frac{I_{Sref}}{I_{Fref}} = \frac{\sin^2(\alpha_0 \pm \beta)}{\sin^2(\alpha_0)}\,. \quad 2.22$$

This primary advantage is that the effects caused by the neutral density filters and the transmission through the plasma both cancel out, leaving Faraday rotation angle to only depend on the intensities of the Faraday images, shadowgrams, and reference images.

### 2.2.1 Investigation of Wire Arrays at the Ablation Stage with UV Interferometry

During the ablation stage, the wire cores ablate a hot low-density coronal plasma that is pulled towards the center of the pinch, and a higher density wire core that remains stationary during this time. The inner solid-liquid wire core can be imaged using X-ray radiography [Lebedev 2000], and the lighter coronal plasma can be studied using a 532 nm laser probe. However, this leaves a portion of the outer part of the wire core plasma that's not dense enough to view with X-ray imaging, but which is dense enough to be opaque to 532 nm laser probing.

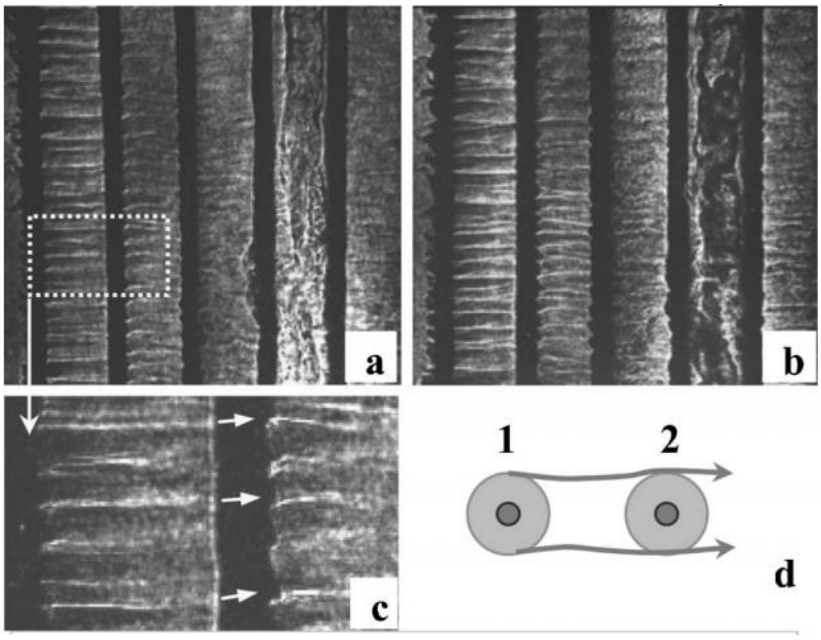


Figure 2.10. (a-c)532nm shadowgram of Wire Array Z-pinch during ablation stage. (d) Diagram showing the path of ablating plasma jets from the wire cores.

Figure 2.10 shows wire cores and ablating plasma jets seen during the ablation stage using 532 nm shadowgraphy of an 8-wire linear load. These jets have been measured to have a radial velocity of 2.0 x $10^7$ cm/s. The electron density of the plasma surrounding the wire core cannot be measured with 532 nm laser interferometry because the plasma is not transparent to wavelength. It is also completely transparent to X-ray imaging with photon energy > 1 keV. Upgrading to 266 nm laser compared to 532 nm allows for the measurement of electron density in this previously unexplored region of plasma in the ablating wire cores.

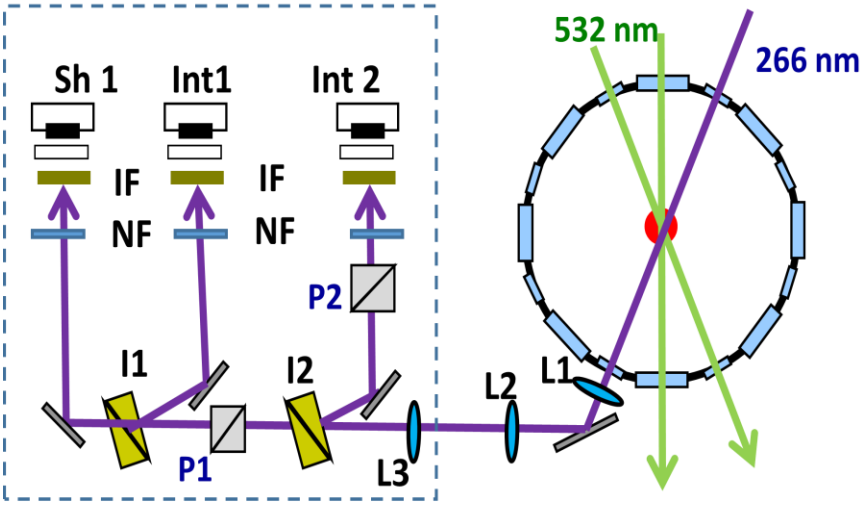


Figure 2.11. Schematic for 2-frame 266 nm interferometry. Two air wedges, I1 and I2, divert the probing beam for the 2 interferometry channels labeled Int 1 and Int 2. The shadowgram Sh 1 is made from the undeflected beam. The orthogonally polarized main and delay beams are selected by using two polarizers, P1 and P2, which block the delay beam and main beam, respectively. Neutral density filters (NF) attenuate the beam.

Experiments were performed with the 266 nm laser probing schematic shown in Figure 2.11. This is two-frame system, with shadowgraphy and an air-wedge shearing interferometer for the first frame, and an air-wedge shearing interferometer for the second

frame, which has a delay of 5 ns. Polarizers separate the orthogonally polarized main and delay beams.

Shot #2883 is shown in Figure 2.12, which shows (a) a shadowgram and (b) interferogram of two wires during the ablation stage. The experimental load was an 8-wire Al cylindrical wire array with wire diameters of 15 microns. An enlarged

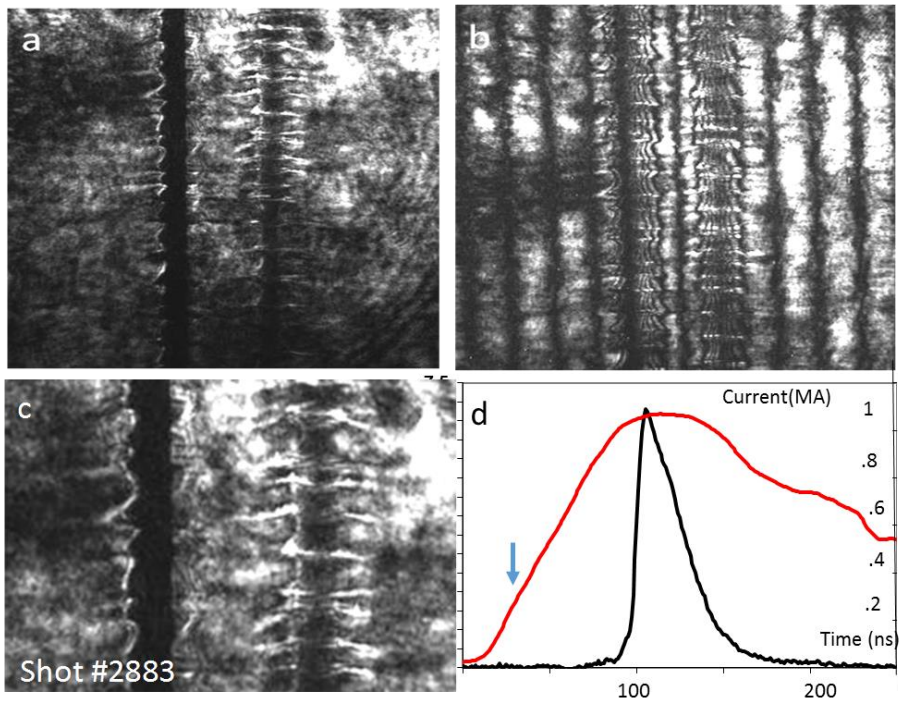


Figure 2.12. Shot #2883 (a)Shadowgram and (b) interferogram of two wires during the ablation stage. (c) Close up of wires in shadowgram. The wire core on the left is still opaque, but the wire core on the right has broken as is transparent to 266nm probing (d) timing diagram showing current (red line), X-ray burst from stagnated Z-pinch (black line) and laser pulse (arrow).

shadowgram in (c) reveals that the wire on the right has breaks in the core and is partly transparent to the UV, whereas the wire on the left has an intact core which is completely opaque to the probing laser. The differential interferogram agrees with this analysis. In the fringe structure on the left, the wire core creates a dark opaque line, which is absent in

the fringe structure on the right. This is the first time that the density of the ablating plasma column can be measured directly with interferometry.

The dynamics of plasma expansion was investigated by studying the electron density profile in the radial direction using two-frame 266 nm interferometry. This electron density of the plasma is determined by measuring the differential phase shift, and

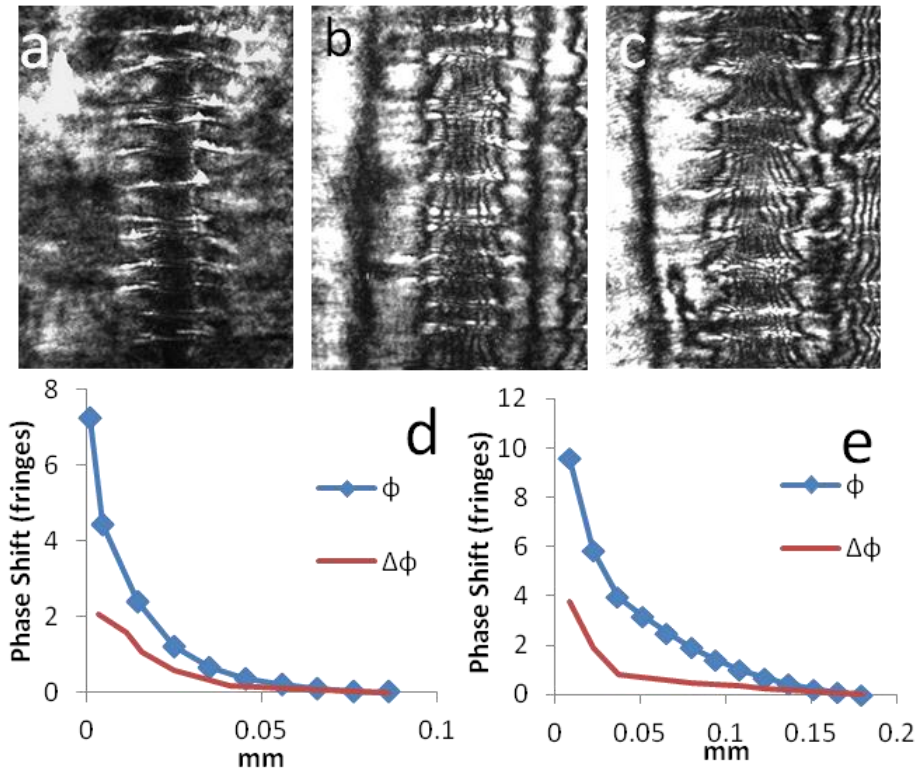


Figure 2.13. Shot #2883 2-frame differential interferometry (a) Shadowgram of wire during ablation stage with (b) accompanying interferometry image and (c) Interferometry image taken 5 ns later (d) and (e) are differential phase (red) and reconstructed phase (blue) plots for first frame and second frame respectively.

recreating the total phase shift as outlined in section 2.1.1. After the phase shift is determined, equation 2.15 is applied to derive the electron density. Figure 2.13 shows the (a) shadowgram (b) interferogram, and (c) delay-line interferogram for the transparent

wire in shot #2883. Figure 2.13(d) and (e) show the measured differential phase shift (red line) and calculated total phase shift for the interferograms in (b) and (c), respectively. The radius is measured from the center of the wire core in the shadowgram, which was confirmed to also be the original pre-shot location of the wires from reference shots.

The electron density was calculated using the Mathcad Prime 2.0 program. A high order polynomial fit function is used to plot the phase. This ensures the smoothness required for Abel inversion, and also makes the spatial derivative of the phase simple to calculate. The Mathcad program is then used to integrate equation 2.15 over the appropriate limits of integration and calculate the electron density of the plasma column.

The resulting electron density profiles can be seen in Figure 2.14, which shows the electron density profiles for the first frame (red) and delay frame (blue). $N_e(r)$ was approximated to the axis by dashed lines in Figure 2.14. The density of the wire core limits the minimum radius the electron profile can measure. The lower plasma density in first frame can measure electron density 40 microns from the center of the wire core, whereas the second frame has a slightly higher peak density measurement but a minimum radius of 80 microns. Assuming an electron temperature of 20-25 eV for the wire array z-pinch near the end of the ablation stage, and an ionization of Z=5-6, calculations for frame 2 account for ~72% of the total mass of the wire. The wire core can include small non-plasma portions, not seen by interferometry, and plasma ablated to the center of the pinch, as well as a distribution of the real temperature and ionization stage is not taken into account in this estimation. Integration of plasma density shows that 36% of the total mass of the wire is contained in the plasma column in frame 1 if Z=5. In this case the rest

of the mass is mostly contained in the non-plasma core.

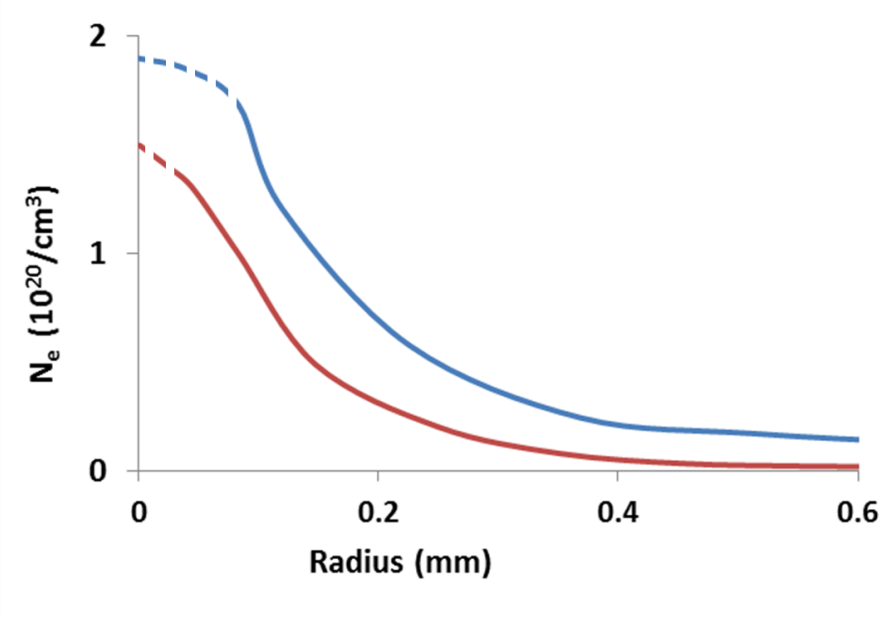


Figure 2.14. Shot #2883 graph of electron density profiles for the first frame (red) and the delayed frame (blue) Dashed lines represent approximated $n_e(r)$.

The two frame interferometry also reveals plasma expansion from the wire core. High density plasma at $10^{20}$ electrons cm$^{-3}$ can be seen at 80 microns in the first frame and 200 microns in the second, which is an expansion rate of 2.4 x $10^5$ cm/s. Plasma with electron density $10^{19}$ cm$^{-3}$ also expands from 320 microns to 800 microns between the two frames, resulting in an expansion speed 9.6 x $10^5$ cm/s. In a paper by Lebedev [1999], the outward expansion of the wire core was measured at 2x$10^5$ cm/s, and the coronal plasma expands at a rate between 1.6 x $10^6$ and 3.2 x $10^6$ cm/s. The core expansion measured by Lebedev agrees with the expansion rate seen for the wire core plasma with density $10^{20}$ electrons cm$^{-3}$.

## 2.2.2 Investigation of Wire Arrays at the Implosion Stage with UV Interferometry

As detailed in section 1.3.2, some load geometries can form plasma bubbles on the surface of the wires, which implode towards the center of the pinch during the implosion stage. Figure 2.15 shows two frames of a 532 nm shadowgraph depicting the formation of these plasma bubbles [Ivanov 2007b]. Fingers of trailing mass are often left behind due to the inhomogeneity of the implosion wavefront caused by these implosion bubbles. The trailing mass plasma bubbles are too dense to measure the electron density

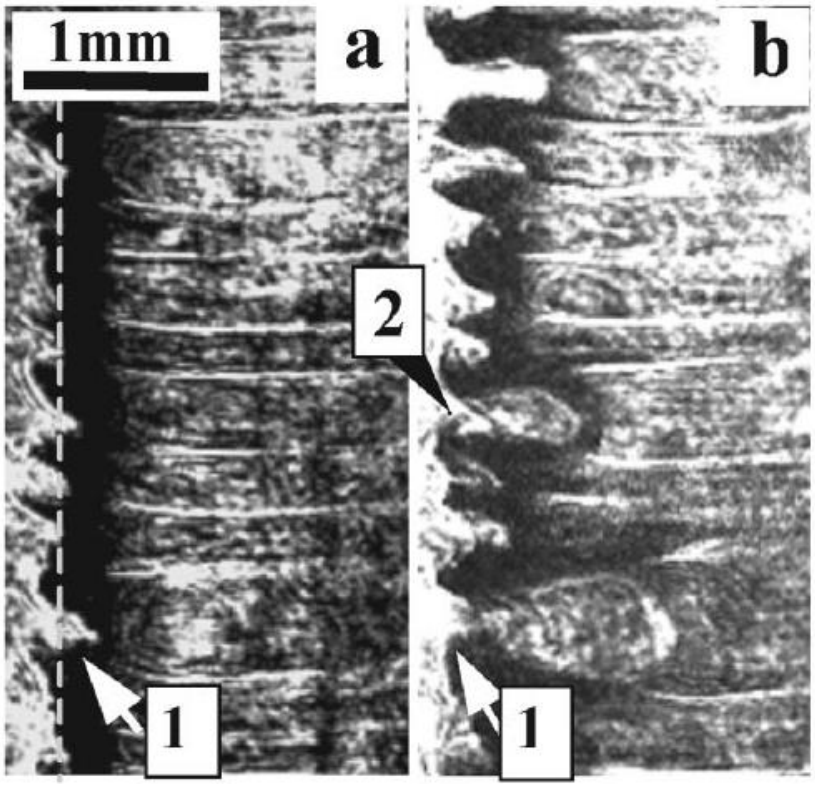


Figure 2.15 Laser shadowgraphy using 532 nm revealing evolution of plasma jets. Two frames (a) and (b) reveal initial formation and expansion of implosion bubble, labeled (1).

directly using 532 nm laser interferometry, and so 266 nm laser interferometry was used to investigate both the fingers of trailing mass, and the gaps between.

Fig 2.16(a) shows a shadowgram of Al linear load during the implosion stage. The outermost wire has formed plasma bubbles which imploded towards the inner wires. Imaged on the right side of the shadowgram is the trailing mass left behind by these imploding plasma bubbles. These fingers of trailing mass were studied along with the

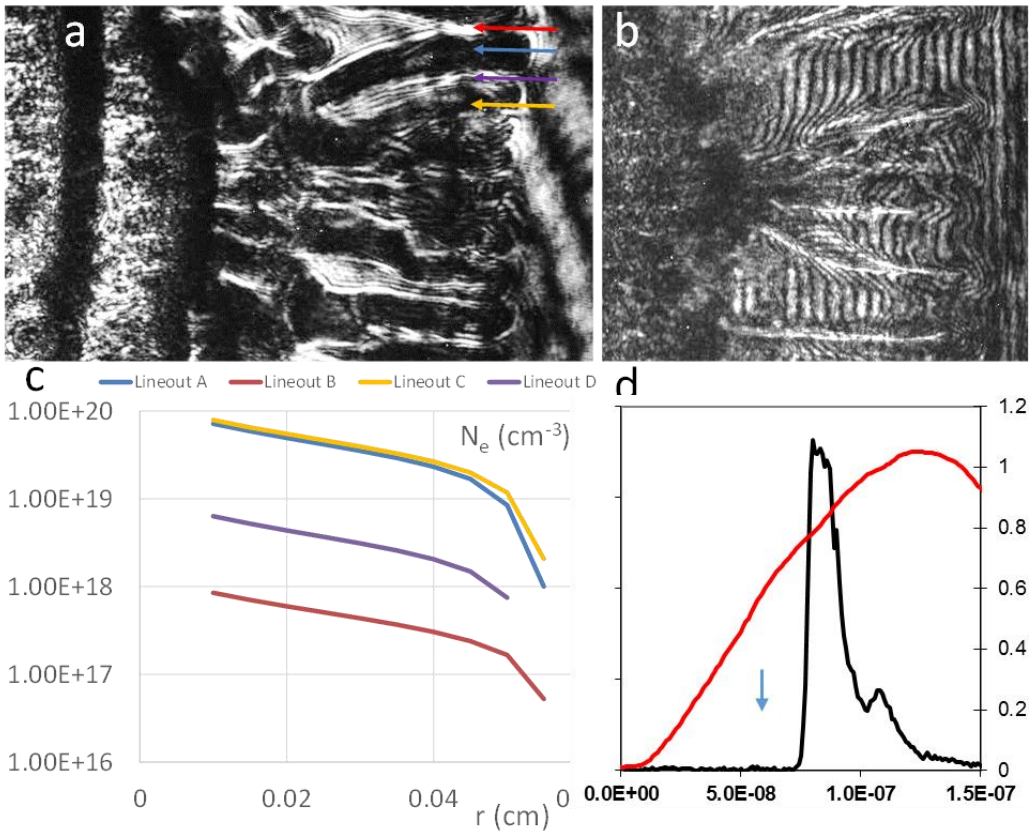


Figure 2.16. Shot #2816 (a) Shadowgram of linear wire array during implosion stage. Four portions were studied, two on fingers of trailing mass, and two in the area in between (b) Complementary interferometry image showing same region (c) Electron density profiles for the 4 line-outs (d) timing diagram with current (red line), X-ray burst from stagnated Z-pinch (black line) and laser (arrow)

gaps in between in order to determine the electron density distribution profile of the

trailing plasma. Four lineouts were taken, two on fingers of trailing mass (blue and orange), and two in the gaps in between (red and purple. The thicker areas have a peak electron density at $10^{20}$ per $cm^3$. The two gaps have electron density $10^{19}$ and $10^{18}$, showing that even the apparently empty gaps between plasma contain some plasma.

The plasma between the fingers of trailing mass may provide an alternate current path after the initial implosion. This would provide the mechanism for the implosion of the remaining trailing mass during stagnation. Z-Pinch X-ray emissions can have more energy than is accounted for using kinetic energy and Spitzer resistive heating [Deeney 1991, Ivanov 2009], and current switching in the trailing mass and re-implosion may account for some of the enhanced plasma heating.

## 2.3 Study of Magnetic Fields and Current Distributions with UV Faraday Rotation Diagnostics in Imploding Wire Arrays

Faraday Rotation diagnostics at the wavelength of 532 nm have been used to study precursor plasma formed during the ablation stage of a wire array Z-Pinch [Ivanov 2006b]. Referring to equation 2.16, the Faraday rotation angle depends on the wavelength of the probing laser, the magnetic field strength, and the electron density of the plasma. This limits the 532 nm Faraday rotation diagnostic's effectiveness in areas which have both high density and local current. Faraday rotation at the wavelength of 266 nm is less sensitive to the magnetic field strength and plasma density (see Figure 2.17), which allows it the ability to study the current distribution of the stagnation stage [Ivanov 2014] and implosion stage.

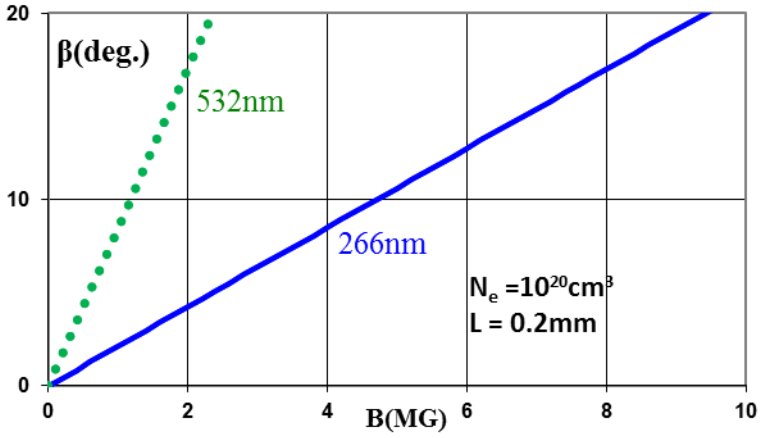


Figure 2.17. Faraday rotation angle as a function of magnetic strength for 532 and 266 nm lasers

The experimental schematic for 266 nm Faraday rotation is shown in Figure 2.18 and explained in detail in section 2.1.2. Simultaneous shadowgrams, interferograms, and

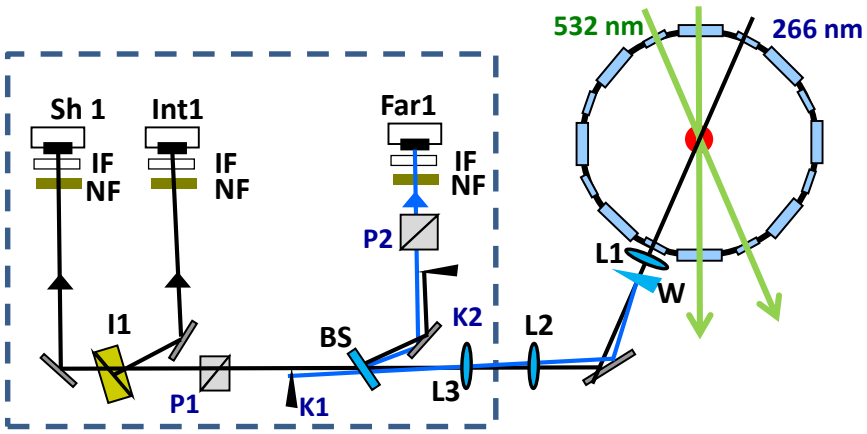


Figure 2.18. Experimental Schematic for Faraday Rotation diagnostic. A Beam-Splitter (BS) diverts the beam to the Faraday channel Far1, and an air wedge interferometer diverts the beam to the interferometry channel Int1. The shadowgraphy channel Sh 1 is made from the undeflected beam. The orthogonally polarized Faraday and Shadowgraphy/Interferometry channels are selected by using two polarizers, P1 and P2. Neutral density filters (NF) attenuate the beam.

Faraday Rotation images are recorded from a single pulse of the 266 nm laser. All three channels and their reference images are necessary for processing of the data.

Figure 2.19 features a shadowgram, interferogram and Faraday image of a star-like wire array with three radial arms, taken during the implosion stage. The arrow on the Faraday image in Figure 2.19(b) reveals a region of lightening on the left side of the right-most imploding plasma column. An area of darkening is located on the other side of the column, and can be readily seen by comparing width of the column in the Faraday image with the width of the column in shadowgram in Figure 2.19(a). This lightening and darkening effect is caused by a Faraday rotation of the polarization angle for the laser. The lightened region of the plasma column is the portion of the pinch that will be examined.

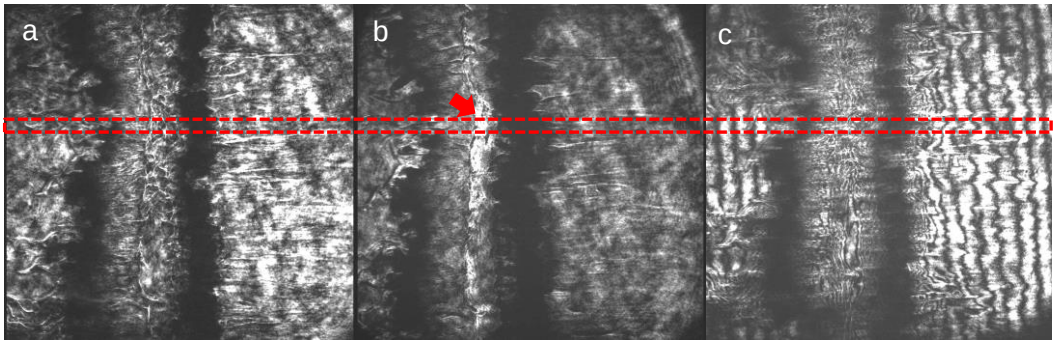


Figure 2.19. Shot #2947 (a) Shadowgram and (b) Faraday image and (c) interferogram of implosion stage. Red box shows lineout used to measure intensity of the two images. In addition, 2 reference images were also used.

To process the data, a lineout is taken of the shadowgram and Faraday image, and the shadowgram and Faraday reference images. The dotted red box in Figure 2.19 shows the location of the lineouts. These intensity profiles then have the background light and

emission from the Z-Pinch canceled out to isolate the probing laser's intensity. The corrected intensity profiles for Faraday image and shadowgram, $I_f$ and $I_s$ respectively, and their reference images, $I_{fref}$ and $I_{sref}$ are shown in Figure 2.20. Intensity plots of the $I_s/I_{sref}$ and $I_f/I_{fef}$ ratios are then created. These intensity profile ratios allow us to extract the Faraday rotation angle β by using equation 2.22.

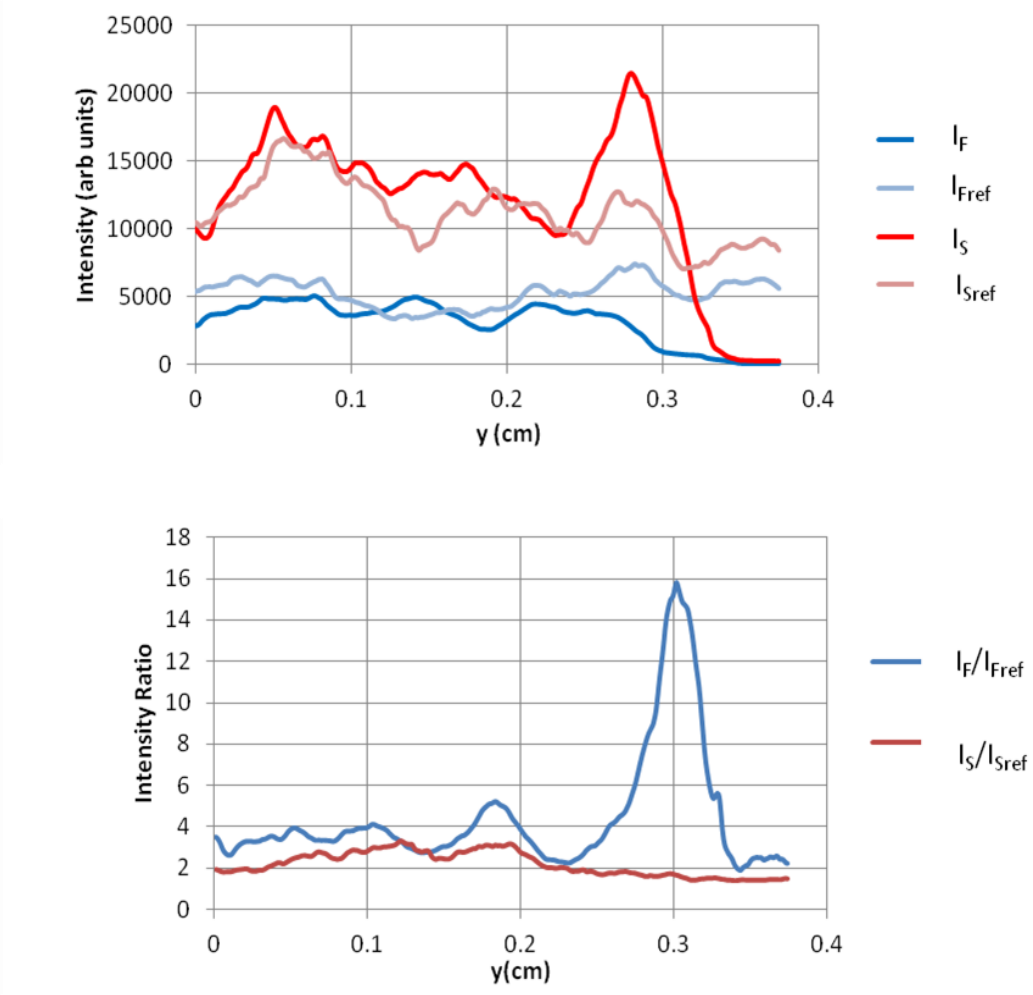


Figure. 2.20. Shot #2947 (a) Lineouts from the shadowgram and Faraday images (b) Intensity ratio profiles for Faraday image and shadowgrams compared to pre-shot reference images.

The intensity profile ratios in Fig. 2.20(b) shows a strong Faraday effect at the distance of 0.3 cm from the center of the wire array. The Faraday rotation depends on both electron density and magnetic field strength. However the magnetic field strength decreases slowly as a function of radius. The reason for the localized peak at 0.3 cm is because that area has a large electron plasma gradient, which causes a larger Faraday effect than the nearby areas. The drop-off from 0.3 to 0.35 cm is due to a higher opacity and refraction in that region, which limits the effectiveness of the Faraday diagnostic. The cutoff for the Faraday rotation analysis is therefore chosen at the peak of the intensity ratio curve to limit contributions from opacity and refraction to the Faraday rotation measurements.

Equation 2.22 is used to calculate the can be used to calculate the Faraday angle β from the intensity profiles. A complementary UV interferogram provides the electron density measurement for the region with the Faraday effect. This can limit the choice of

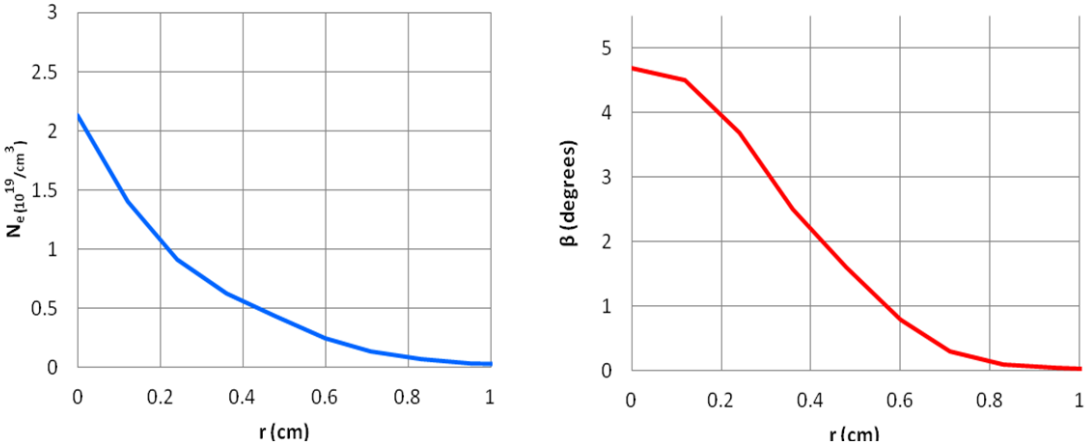


Figure 2.21.Shot #2947 Electron density profile from interferogram and calculated Faraday rotation angle.

regions that can be explored with Faraday rotation, since the diagnostic requires both high electron density and magnetic field strength to get a large Faraday effect, and a clean interferogram in the same area to measure the electron density. The calculated electron density profile from the laser interferometry and the calculated Faraday rotation angle for shot #2947 is shown in Figure 2.21. The origin is defined as the peak of the Faraday effect, with the radius extending away from the opaque plasma column.

After finding the Faraday rotation angle $\beta(r)$ and electron density $n_e(r)$, equation 2.17 can be used to measure the magnetic field strength. As seen earlier with the interferometry, the necessary smoothing of the electron density $n_e$ and Faraday rotation angle $\beta$ and the imposed cylindrical symmetry for Abel-inversion of the data create a ~30% error, which makes the diagnostic only appropriate for simple models of current distribution during the Z-Pinch. In addition, areas of low electron density can lead to large distortions in the calculated magnetic field, and regions with a large electron density gradient can refract or absorb the probing laser beam, making the area not suitable for processing. These regions unsuitable for processing are shown in the left and right shaded boxes in Figure 2.22(a). The left darker-shaded region is the region of high gradient, and the second lightly-shaded region is the area of low electron density.

In Fig. 2.22(a) the magnetic field strength profile has been created using Abel inversion (blue line). Also included is a simple model of a uniform cylinder of current, with strength 0.6 MA and a radius of 0.08 cm (red line). Two shaded region The portion of the pinch being studied has two columns overlapping in a 3-star configuration, as can be seen by the double structure in the wires on the right side in the reference image seen

in Figure 2.22(b) and the diagram in Figure 2.22(c). Assuming ~ 1-MA of current is evenly distributed between the 3 columns, roughly 0.6 MA would be on the right column,

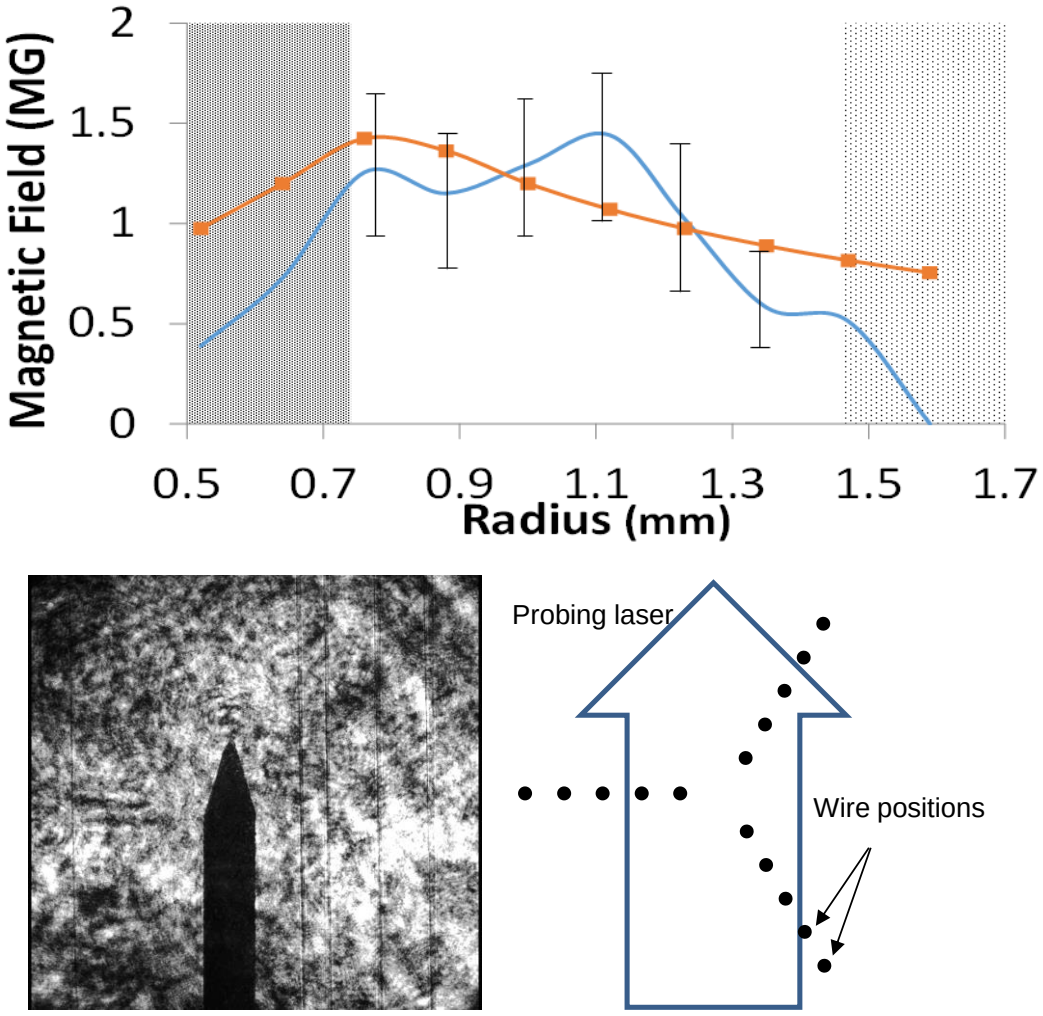


Fig. 2.22. Shot #2947 (a)Reconstructed magnetic field (blue line) and simple model of a uniform cylindrical 0.6 MA current with radius 0.08 cm (red line). Shaded area on left represents area of high gradient, and shaded area on right represents area of low electron density. (b) reference image showing wire positons and center of the array (needle) (c) schematic showing pre-shot wire positons.

and the magnetic field strength is consistent with expected results. We note that Figure 2.22 shows the first direct measurement of the current distribution in the 1-MA wire array Z-Pinch at the implosion stage.

# Chapter 3

# X-ray Imaging of the Ablation stage of the wire array Z-Pinch

The first application of the X-pinch for radiography of the Z pinch was presented in [Kalantar 1993]. A hot plasma spot of the X-pinch radiates a short X-ray burst with a duration ~0.1 ns in the keV range. X-pinch mounted to the return current system was applied for backlighting of wire arrays at the ablation stage in 1 MA pulsed power facilities at Cornell University [Pikuz 1999, Zier 2009, Ampleford 2008, Blesener 2009], Imperial College [Lebedev 2001a, 2001b], and at the 4 MA Angara-5 generator [Grabovskii 2004]. A small 3-5 μm size of the hot spot provides high spatial resolution of point-projection radiography based on the X pinch.

Fine details of the wire core structure in wire arrays at the ablation stage were studied in papers of [Lebedev 2001a, 2001b, Pikuz 1999, Zier 2009, Ampleford 2008]. It was found that the wire core has a foam-like liquid-vapor structure [Pikuz 1999]. A structure like a disc sequence was observed in the wire core in [Lebedev 2001a]. Development of instabilities on the wire core and correlation of instabilities at different wires in the wire array were studied in papers [Lebedev 2001b, Zier 2009]. Development of instability on the core of the modulated wire was investigated with X-pinch radiography in [Ampleford 2008]. Recently, the end-on X-pinch radiography was applied to the wire array at the Cornell University [Blessener 2009]. Laser-based radiography of Z pinches was developed at the Z machine [Sinars 2005]. Due to flexible delay of the laser pulse compared to the X-pinch pulse, Z pinches were backlighted at both the ablation and implosion stage.

The goal of our X-ray radiography is coupling of UV laser shadowgraphy/interferometry and X-ray probing to investigate Z pinches in a wide range of plasma density. We also note, that the laser-based X-ray radiography for wire arrays at the ablation stage was developed at NTF as the first step of the research program. In future, wire arrays at the implosion and stagnation stage will be investigated at the Zebra generator using this techniques and will be applied to different types of plasma objects.

## 3.1 Introduction for X-ray Imaging Radiography

X-ray imaging radiography was fielded as a diagnostic to measure the wire core radius during the ablation stage of a 1 MA wire array Z-Pinch. UV laser diagnostics are limited by the inverse Bremsstrahlung absorption of the plasma, which limits the maximum electron density to the order of (1-3) x $10^{20}$ electrons per $cm^3$. X-ray imaging is complementary to the UV laser diagnostic and allows for the measurement of plasmas up to the density of a solid. Low-density plasma is transparent to X-ray, so we can expect imaging only of the solid-liquid wire core at the ablation stage. We note that x-pinch radiography has been used at Imperial College and Cornell University for probing wire-array Z pinches at the ablation stage. X-pinches provide a small bright source of radiation but it can be used only at the ablation stage. Laser radiography is flexible for delay and spatial position to the Z pinch and may be applied to any stage of the pinch. Only a 26 MA pulsed power Z machine at Sandia National Laboratories has the capability for laser backlighting using the 5 kJ BEAMLET laser. X-ray imaging with bent spherical crystals allows for high resolution, time resolved measurements of the high density wire core structure of wires seen during the ablation stage.

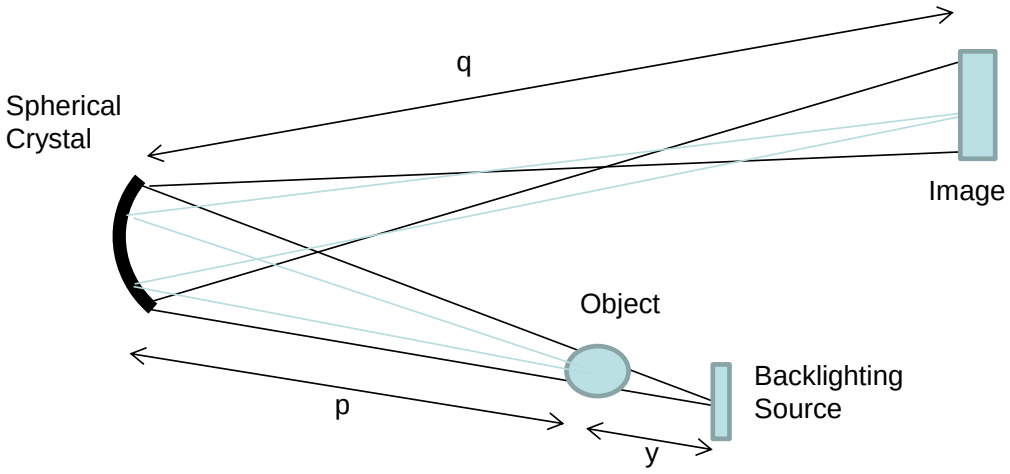


Figure 3.1. Optical schematic for X-ray imaging radiography using a spherically bent crystal.

The X-ray imaging scheme chosen for this purpose takes advantage of a spherically bent crystal's ability to create an image using a monochromatic X-ray backlighting source. Figure 3.1 shows a typical X-ray imaging schematic. The X-ray source creates an envelope of radiation which backlights an object, which in our case is a wire array Z-Pinch. The crystal images the shadow of the object onto a detector.

This scheme offers several advantages over other methods of X-ray imaging. It creates a large field of view, at the scale of ~1-3 centimeters, while maintaining high spatial resolution [Aglisky]. In addition, there is a spectral filtering from self-emission of the plasma being probed, allowing for the backlighting source to be orders of magnitude lower in luminosity in the probing wavelength and still remain effective.

The spherically bent crystal is aligned to satisfy the Bragg condition

$$2d \sin\theta = m\lambda , \qquad 3.1$$

where d is the inter-planar spacing for the crystal lattice, θ is the angle of incidence, m is the order and λ is the X-ray wavelength. The crystal has a high spectral selection Δλ/λ, which can be calculated using [Sinars 2003]

$$\frac{\Delta\lambda}{\lambda} = \frac{\Delta x}{R}\cot\theta\,, \tag{3.1}$$

where Δx is the width of the backlighting source, and R is the crystal bending radius. For a crystal of bending radius 20 cm – 50 cm at a Bragg angle greater than 80° and a backlighting source size of ~1 mm, the spectral selection is of order $10^{-4}$. This high spectral selection can isolate the backlighting source to within a single spectral line.

Optically, a bent spherical crystal essentially behaves like an off-axis dispersive spherical mirror. Since the imaged object, in our case a wire array Z-Pinch, is not located on the optical axis, third order astigmatism is the primary concern for resolution limits. This occurs because the focus length for the meridial and sagittal planes is different. For such a system, the lens equation for the meridial and sagittal planes are [Hecht 2002]

$$\frac{1}{p} + \frac{1}{q_m} = \frac{2}{R\sin\theta} \tag{3.1}$$

$$\frac{1}{p} + \frac{1}{q_s} = \frac{2\sin\theta}{R} \tag{3.2}$$

where R is the bending radius of the crystal, θ is the Bragg angle, p is the object to crystal distance, and $q_s$ and $q_m$ are the crystal-to-image distances for the sagittal and meridial planes, respectively. The astigmatism can be mitigated by choosing a Bragg angle > 80 degrees, thus minimizing the sin θ contribution from the astigmatism. The distance R/2 is known as the medial focus, as it splits the difference between the sagittal and meridial

focus distances, which happens to be the same focus for a spherical mirror normal to a source. This focus length is useful for achieving the best balance for optical resolution in the sagittal and meridial plans.

Therefore, the location for the focal plane for the X-ray imaging scheme can be approximated using the lens formula for a spherical mirror,

$$\frac{1}{p}+\frac{1}{q}=\frac{2}{R}, \tag{3.3}$$

where p and q are the object-to-mirror and mirror-to-image distances, and R is the bending radius of the crystal.

The magnification M of the system can be adjusted by choosing the distances p and q according to the formula

$$M=\frac{q}{p}. \tag{3.4}$$

Large magnification is useful for imaging the small structure of the wire cores, which is shown to typically be 4-8 times the initial wire diameter, or several tens of microns. However, increasing the magnification is offset by decreasing the Field-Of-View (FOV) for the X-ray imaging system, which can be calculated by the equation [Sinars 2003]

$$FOV=L\frac{y}{p+y}, \tag{3.5}$$

where y is the distance from the backlighting source to the wire array and L is the width of the crystal.

Spatial resolution, σ, can also be approximated, using the equation [Sinars 2003]

$$\sigma = \frac{\Delta x \cdot p}{y}\frac{(M+1)(1-\sin^2\theta)}{M}. \quad 3.6$$

This spatial resolution typically underestimates the actual spatial resolution by a considerable factor.

### 3.2 X-ray Imaging Diagnostic Design

The X-ray imaging scheme is designed to accommodate conditions found within the Zebra chamber. The Zebra chamber has a radius of 30 centimeters, and the different elements must fit inside with enough space to prevent contact with the chamber walls and facilitate loading and unloading. Within this limit, we sought to increase the magnification as much as possible.

The spherically bent crystal used in the experiments was made of quartz 1011, with a bending radius of 25 cm. The object must be located at a distance

$$\frac{R}{2} < p < R\,. \quad 3.7$$

For distance p's that are shorter than R/2, the focal plane is imaginary. For p's larger than R, the focal plane lies between the object and the crystal, and the small angle separating the incoming and reflected light makes data collection impossible. For crystal with a bending radius of 25 cm, this limits the distance between object to crystal to between 12.5 cm and 25 cm.

In addition to this constraint, it is necessary to limit the crystal-to-image distance, q, so that the image is located within the experimental chamber. The radius of the Zebra chamber is 30 cm, and using the lens equation

$$\frac{1}{p}+\frac{1}{q}=\frac{2}{R} \qquad 3.8$$

and requiring that the image is located inside the chamber, the object-to-crystal distance must be greater than 17 cm, giving a final range of 17 cm to 25 cm between the crystal and the wire array load.

One final consideration is determining an appropriate backlighter-to-object distance y. To this end, the Rowland circle makes a useful reference point for evaluating the placement of the backlighting source. The Rowland circle, which is circle with diameter equal to the bending radius R of the crystal, has the property that if a spherically or cylindrically bent crystal is placed tangentially on the Rowland circle, an X-ray source originating at a point on the circle will have its focus also located on the Rowland circle.

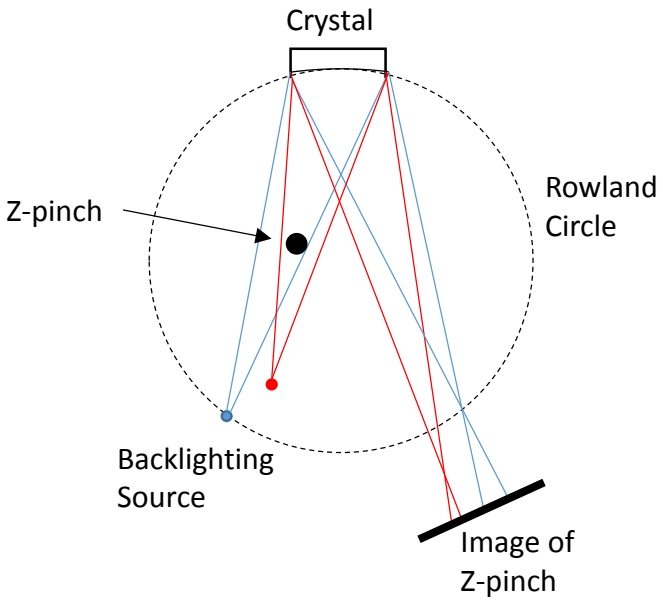


Figure 3.2. Comparison of backlighting sources on the Rowland circle (blue) and inside the Rowland circle (red) offset for visibility. The backlighting source moved inside the Rowland circle has a larger collection angle but the image has a smaller field of View.

Equation 3.7 shows that the wire array Z-Pinch must be located inside the Rowland circle formed by the spherically bent crystal, making locating the backlighting source at the Rowland circle a convenient starting location. Figure 3.2 shows a spherically bent crystal placed tangentially on a Rowland circle with two backlighting sources, one on the Rowland and one placed further inside. If the backlighting source is placed inside the Rowland circle, the intensity of the backlighter will be amplified due to a larger collection angle, at the cost of a small reduction in spatial resolution and reduced field of view. Outside the Rowland circle, the intensity of the backlighter will be lower, but the spatial resolution and field of view slightly improved. A compromise between the intensity, field of view and resolution must be made.

There are additional concerns involving the protection of the optical elements inside the chamber. The Z-Pinch itself creates approximately 1 kJ of 1 keV or higher emission. This background radiation could drown out the backlighting source if not properly shielded. In addition, debris from the dissipating Z-Pinch can damage the optical elements, in particular the bent spherical crystal and the film cassette. Finally, there is an approximate 200 g shock from the imploding Z-Pinch that can also cause damage to elements in the chamber.

To address the large X-ray burst caused by the Z-Pinch, a lead plate wrapped in copper is inserted between the pinch and the film cassette, blocking the radiation and debris emitting from the Z-Pinch. In addition, two collimators are placed along the X-ray imaging beam path, geometrically blocking additional background radiation and plasma debris from the spherically bent crystal and film cassette. In addition, a beryllium filter is

placed in front of the spherically bent crystal, which allows X-rays to pass through unhindered but acts as a screen for any additional debris not blocked by the collimator. The angle of incidence for the X-rays on the crystal allows for the incoming and outgoing optical paths to pass through the same filter. The shock from the Z-Pinch is mitigated by mounting the optical elements on foam which helps absorb shock.

For these experiments, the spherically bent crystal used was a Quartz 1011 crystal with a bending radius of 25 cm. The crystal lattice structure has an inter-planar 2d spacing of 6.685 Å. The Si He-α spectral line has a wavelength of 6.65 Å and is a bright spectral line, which makes it ideal as a backlighting source for this crystal. The associated Bragg angle for this spectral line is 83.9°. This schematic allows a spatial resolution ~ 10 μm [Sinars 2003].

A setup of the Zebra vacuum chamber with backlighting is shown in Figure 3.3. The backlighting source of X-rays is generated by the Leopard laser (Chapter 1.5). A small silica target is placed inside the chamber, and is struck by the Leopard laser, creating a laser plasma which emits the Si He-α X-rays along with many other spectral lines. The Si He-α are isolated by the high spectral selection of the system.

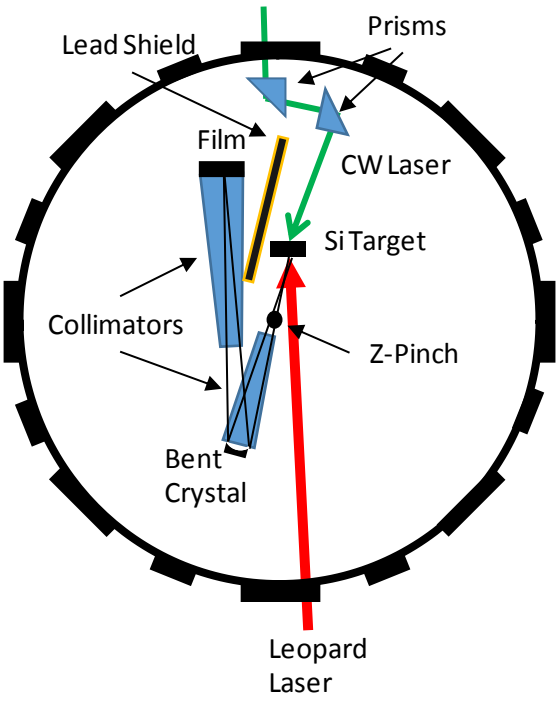


Figure 3.3. Schematic of X-ray imaging diagnostic inside the Zebra chamber.

Alignment of the Leopard laser is performed by first aligning the X-ray imaging system with a CW laser. A pair of prisms located inside the chamber align the beam to transverse through the Si target (which is replaced by a glass slide), the wire array and the spherical crystal. Once all three elements are properly aligned, the spherical crystal is rotated by the Bragg angle and the film cassette is aligned. The Leopard laser is then aligned to precisely intersect the CW laser at the Leopard laser target. Figure 3.3 shows the alignment with the CW alignment laser at 532 nm.

## 3.3 Initial X-ray Imaging Experiments

Two series of shots were performed at the Zebra generator with backlighting by the Leopard laser. Initial experiments were performed to test the viability of the system. The first tests used Leopard only shots inside the Zebra chamber. These shots were performed without the presence of the Z-Pinch in order to check if wires were visible using the X-ray imaging diagnostic and test the spatial resolution of the system experimentally. Figure 3.4(a) shows an image taken during these Leopard only shots. Wires with diameters as small as 7.6 micron were visible with a field of view of 2 mm.

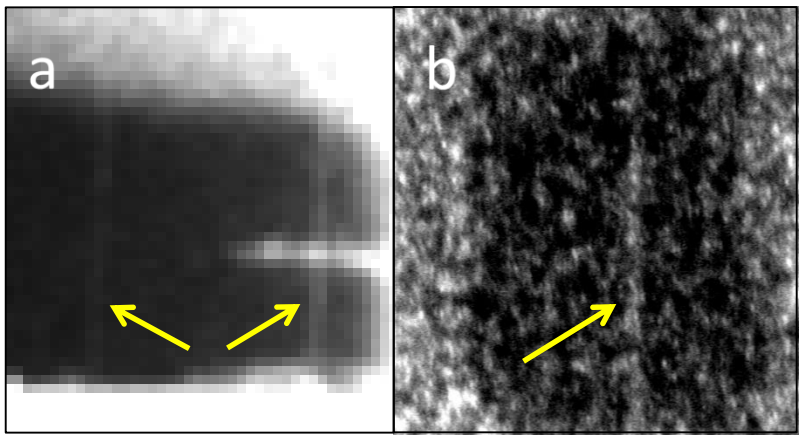


Figure 3.4. (a) 7.6 μm Ni wires imaged using X-ray imaging during a Leopard only shot. (b) 7.6 Ni wires during a test shot using X-ray imaging during a Zebra-Leopard coupled shot. Large amounts of background noise is present.

Experimental shots coupled with the Z-Pinch were then performed. These shots were all performed during the ablation stage, where the dense wire is still present. The wires are still visible, but these experimental shots showed large amounts of background noise. The source of the background noise was determined to be created by secondary radiation from the Z-Pinch. The radiation from the Z-Pinch can cause the metal in the

Zebra chamber to fluorescence, producing additional sources of radiation in the chamber. The next phase of experiments used an addition collimator placed in front of the film cassette to combat the background noise caused by secondary sources of radiation.

## 3.4 X-ray Imaging and UV Probing Experiments of the ablation

The next set of experiments studied the ablation stage of the wire array Z-Pinch using X-ray imaging radiography, and in addition a number shots were also performed with UV laser probing. Coupling these two diagnostics allows for the study of the high density wire core with the X-ray imaging, and the surrounding ablating plasma using UV interferometry in order to generate an electron density profile. The schematic for this system is shown in Figure 1(a), with the 266 nm probing laser traveling in a region of empty space between the two collimators to probe the Z-Pinch.

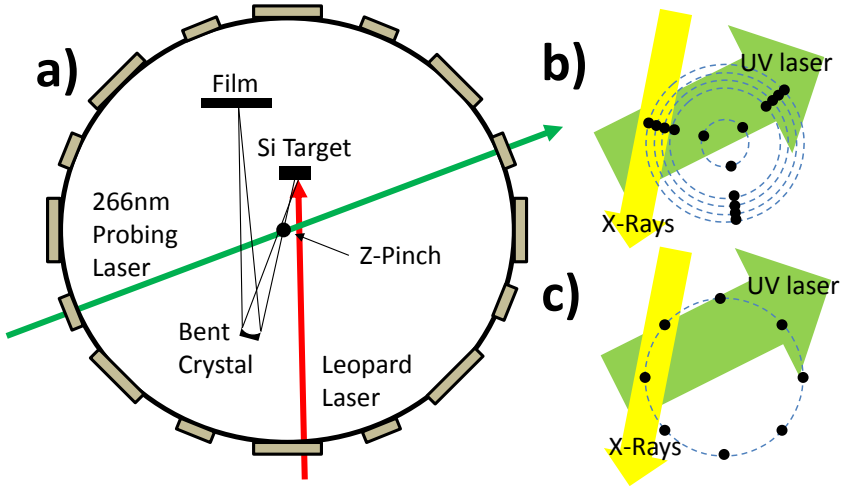


Figure 3.5 (a) Experimental Schematic for simultaneous 266nm laser probing and X-ray imaging. Experiments were performed by (b) star-like wire array and (c) cylindrical wire arrays with 20mm diameters.

Experiments were performed using two types of wire array loads. The star-like

wire arrays had 3 radially extending rays with 4 or 5 wires each, for a total of 12 or 15 wires. The distance from the wires to the center of the pinch wires in each ray are 10/9.25/8.5/7/3 mm for 15 wire arrays and 10/9.25/8.5/3 for 12 wire arrays. The X-ray imaging diagnostic is perpendicular to the direction of one array, and aligned to the outermost wires as illustrated in Figure 3.5(b). 8-wire cylindrical wires were also used, with a diameter of 20 mm. Both arrays are made out of aluminum 5056. These wire arrays generate 5-8 kJ of X-ray energy.

An X-ray backlit image of a 15-wire Al star-like wire array from Zebra-Leopard shot #3349 is shown in Figure 3.6. The image is of the 3 outer wires in a single radial ray, as shown in Figure 3.5b. The image was processed by measuring the average Full-Width Half-Max (FWHM) of the wire cores. The outer wire has a diameter of 87 microns, while the inner wires have diameters of 77 microns each. This result is

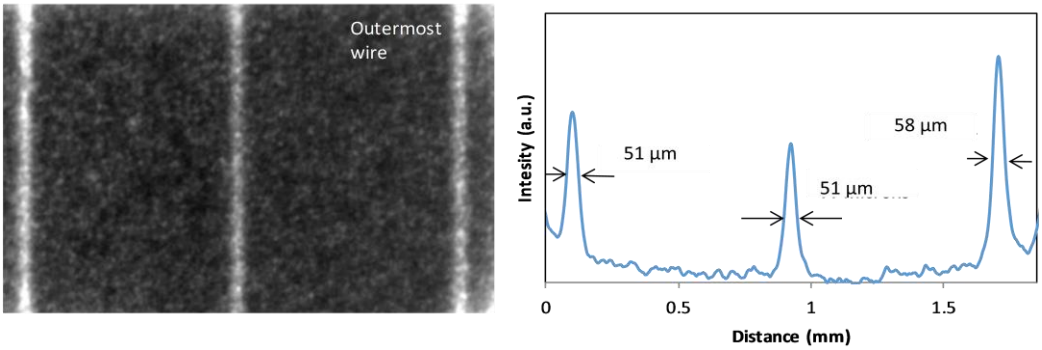


Figure 3.6. Shot #3349 X-ray imaging radiography of a star-like wire array during ablation stage at 170 kA of current.

consistent with previous work done with star-like wire arrays [Ivanov 2007b]. As outlined in section 1.3.2, star-like arrays feature a cascading implosion, where the outer wires ablate first, and implode while the inner wires are still in the ablation stage. The

outer wire is further advanced in the ablation stage and would be expected to have a larger wire core. Spatial resolution was determined to be ~15 μm.

Eight experimental shots were measured to determine the wire expansion rate. Figure 3.7 shows the FWHM of a number of Al cylindrical and star-like wire arrays. Blue triangles represent the wire core diameter for the outer wires in star-like arrays, and red triangles represent the wire core diameters for cylindrical arrays. Green circles represent the wires for the inner wires of a star-like array. Wire core expansion in the wires appears to be insensitive to initial wire diameter, but does depend on load

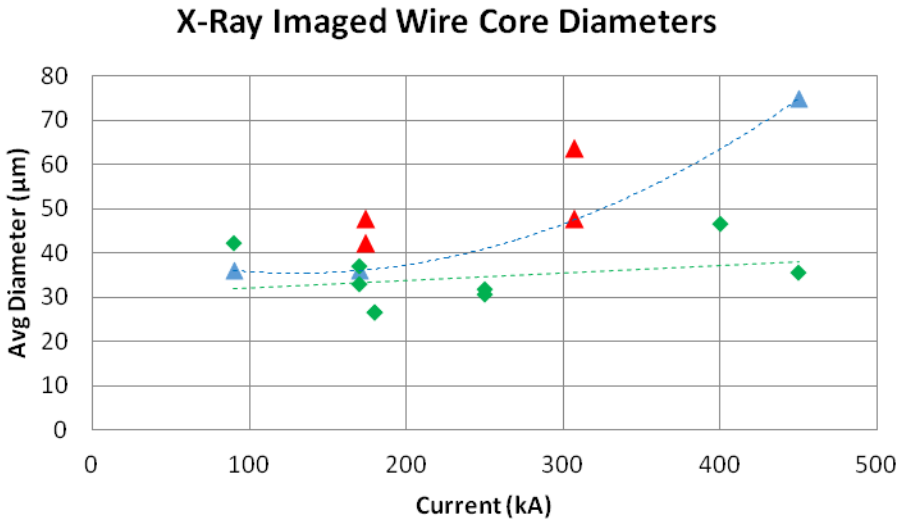


Figure 3.7 Wire core diameters as a function of current. Red triangles represent wire cylindrical loads. 12 and 15 wire Star-like loads are represented by the blue triangles for the outermost wires, and green diamonds for the inner wires

geometry. The outer wires in the star-like loads expand at a rate similar to the cylindrical loads, at roughly 1.5 μm/ns, or 1.5 x $10^5$ cm/s. This rate is similar to the rate of expansion seen in Chapter by the 2-frame UV interferometry of 2.0 x $10^5$ cm/s. However, the inner wires in a star-like appear to have little to no expansion. This is

expected due to the characteristics of a cascading implosion. Implosion in star wire arrays starts in the outermost wires but the innermost wires are not intact up to the moment when main implosion material hits the next wire. After that, the second wire become the outermost wire. Additional current switch to these wires, heats plasma and the core begins to expand at this time.

The UV shadowgraphy and interferometry was coupled to the X-ray imaging radiography for a number of shots. The UV laser interferometry is processed using the methodology outlined in Chapter 2. Figure 3.7 (a-c) shows a UV shadowgram and interferogram, and accompanying X-ray backlit image, respectively, for an 15 8-wire Al

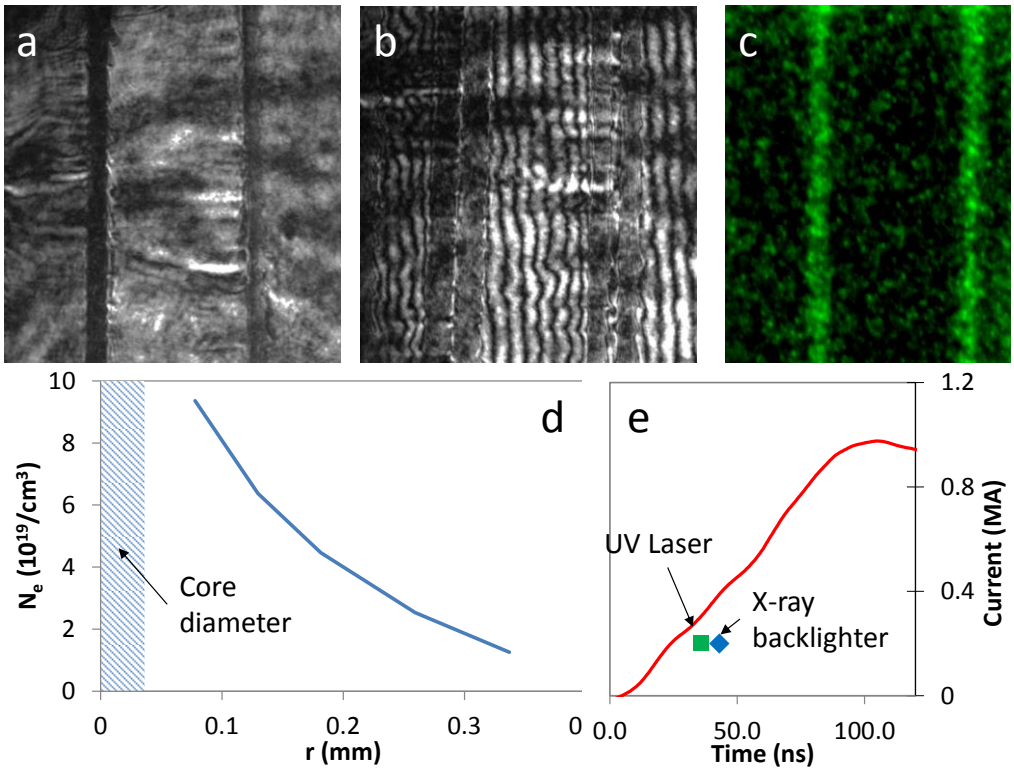


Figure 3.8. Shot #ZL3357 with (a) UV shadowgraphy, (b) UV interferometry and (c) X-ray backlighting. (d) Electron density profile of the outer wire core from UV, and inner solid-liquid wire core diameter from X-ray backlighter. (e) Timing diagram for UV laser, X-ray backlighter and Zebra current

cylindrical load. The X-ray imaging reveals an average wire core radius of 24 microns, and the UV laser interferometry measures a peak electron density of 9.4 x $10^{20}$ cm-3 at 78 microns from the center of the wire core, as shown in Figure 3.8(d). The X-ray backlighter was triggered with a 7 ns delay after the UV laser probe. The coupling of these two diagnostics allows for the investigation of the dense plasma and wire cores in a wide range of plasma conditions.

A flexible delay of our laser backlighting to the Z pinch gives an opportunity to investigate implosion and stagnation stages. Plasma of the imploding Z pinch is probably not dense enough for the X-ray probing but the internal structure of other objects at the Zebra pulsed power generator can be investigated. For example, 1-2mm rods loads were developed and studied at UNR [Awe]. For these loads even UV laser probing is not effective due to the high density and large size of the object.

# Chapter 4

# Absorption Spectroscopy of wire-array plasma at the ablation stage

## 4.1 Introduction to Absorption Spectroscopy

Absorption spectroscopy has been a powerful tool for the investigation of plasma. Laser-produced plasma is widely studied with absorption spectroscopy to measure plasma parameters, study plasma opacity and the spectral features of plasma in different conditions [Schott 2003, Audebert 2005]. It has also been used at the Z-machine at Sandia National Laboratories to measure Fe opacity at conditions relevant to solar physics applications [Bailey 2007]. Nevertheless, absorption spectroscopy has not been applied to diagnose Z-Pinch plasmas before our work. In this section we present the first experimental application of laser-based absorption spectroscopy technique to the 1-MA Z wire-array pinch at the University of Nevada, Reno. Later, absorption spectroscopy was also developed in the Cornell University using bremsstrahlung radiation of the X-pinch for backlighting of the 2-wire array model.

X-ray spectroscopy is a common diagnostic for studying the electron temperature and density of Z-Pinch plasmas. During the stagnation stage, regular well-developed X-ray emission spectroscopy methods can be used with K-shell and M-shell radiation to determine electron temperature and density using computer simulations involving atomic codes. However, during the ablation and implosion stages, K-shell emission spectroscopy cannot be used to measure the electron density and temperature, as the

electron temperature of the plasma is too low to sufficiently ionize the plasma to get K-shell emissions which usually needs ionization >9 in Al plasma. Measuring the parameters of wire-array plasmas at these early stages is important for studying the formation of Z-Pinches at the stagnation stage.

In order to measure the electron temperature at the non-radiative ablation stage, X-ray absorption spectroscopy can be used instead of X-ray emission. A continuum or quasi-continuum X-ray spectra backlights the plasma, and is absorbed by the bound electrons in the plasma. The absorption spectra is determine the energy difference between quantum states of the atom. The K-shell absorption lines are useful for determining the electron temperature, due to higher separation between atomic transition levels. The absorption cross-section for the plasma can be determined by using collisional-radiative and spectral atomic codes, such as a PrismSPECT program for atomic simulations.

. We performed a laser based backlighter using the Leopard laser at the Nevada Terawatt Facility. This offers several advantages. The Leopard laser offers flexible timing, and allows for a variety of target materials. This is in contrast to using X-pinch as a backlighting source, which diverts current from the main Z-Pinch and which requires careful calibration of the wire material and thickness and has a limited window for timing. However, one major concern is that the X-ray emission for the backlighting laser plasma, with approximately 0.1 J of X-ray emissions, is dwarfed in comparison to the X-ray emission from the stagnated Z-Pinch at the Zebra generator at NTF, which typically generate up to 0.5 - 1 kJ emissions in a keV range with total X-ray energy of 5-8 kJ.

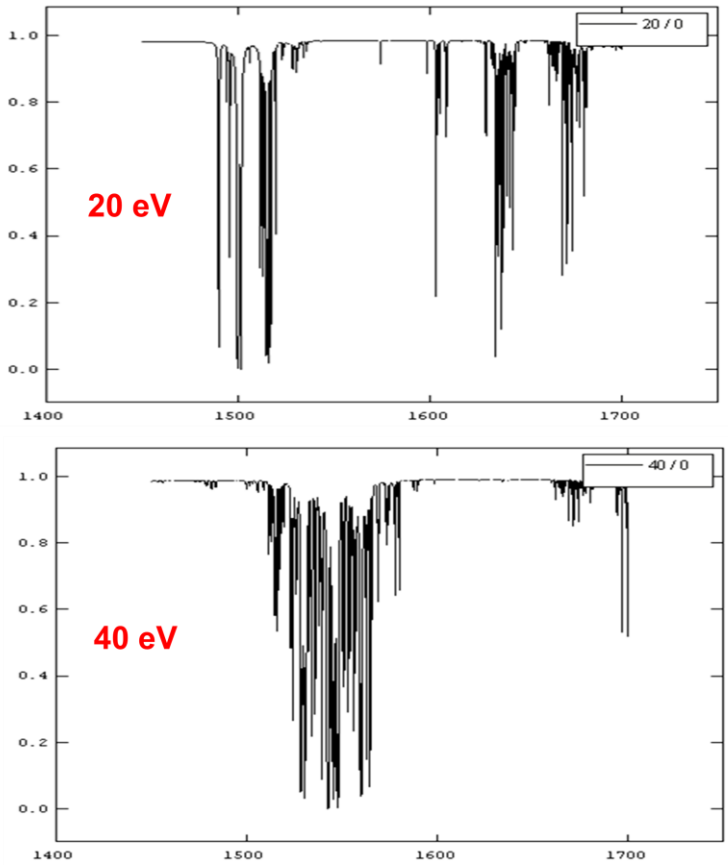


Figure 4.1. PrismSPECT absorption spectra for Al plasmas at two different temperatures

Preparation first came from using of theoretical simulations to reveal potentially strong absorption lines during the ablation and implosion stage for aluminum wire array Z-Pinches. The ablation and implosion stage typically has electron temperatures in the range of 5-50 eV. This range was investigated with simulations performed with PrismSPECT and ATOKIN (T. Durmaz) atomic codes. As shown in Figure 4.1 strong absorption lines were discovered in the region of 1.4-1.8 keV (6.9-8.85 Å), especially the 1.45-1.55 keV range. The absorption spectra in the 5-50 eV range occupies a different spectral range than the emission of the 400 eV stagnating Z-Pinch plasma. This allows spectral separation of absorption and emission spectra. The PrismSPECT program is also

available at NTF. Figure 4.2 presents our simulations of transmission in cold Al plasma with the electron temperature of 5 and 15 eV and resolution of the spectrometer of R=300.

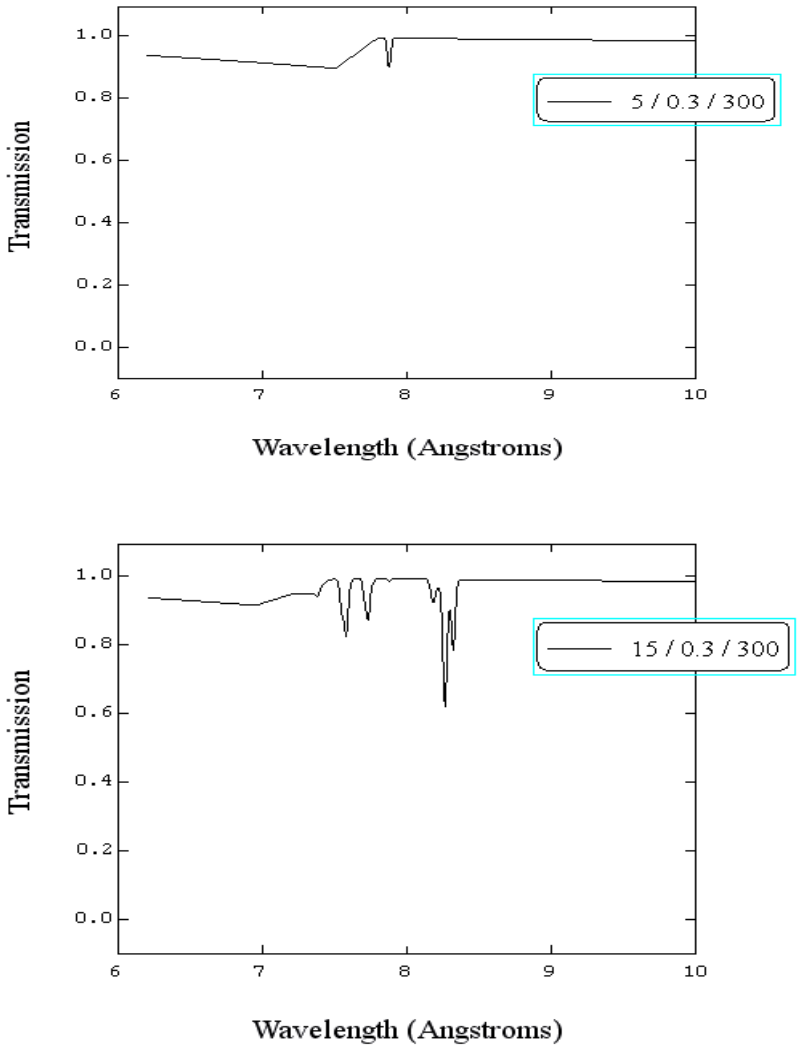


Figure 4.2. PrismSPECT simulations of transmission in Al plasmas at two different temperatures 15 and 5 eV, resolution of the spectrometer of R=300, and density of 0.3 mg/cm$^3$

## 4.2 X-ray Absorption Spectroscopy Experimental Set-up at the Zebra Generator

A 50-TW Leopard laser was used for backlighting of wire arrays at the Zebra generator. Preliminary laser-only experiments were carried out at NTF. The Leopard laser consists of the Tsunami master oscillator, Offner stretcher, Ti:Sapphire regenerative amplifier, amplifiers with mixed phosphate/silicate Nd:glass, and a two-pass gratings compressor. The wavefront of the laser beam is corrected with an adaptive mirror. A chirped laser pulse with a central wavelength of 1056 nm and duration of 0.8 ns is amplified in rod and disc amplifiers with the output apertures of 94 mm. This pulse is compressed in the gold-coated grating compressor to the pulse duration of $\Delta t = 0.35$ ps. The intensity contrast ratio is $>10^6$ in the nanosecond range. Intensity of the laser beam is $I > 10^{19}$ W/cm$^2$ in the sub-picosecond regime. The Leopard laser can also operate in the sub-nanosecond regime, $\Delta t = 0.6$ ns with energy up to 40 J in which case the compressor is bypassed.

Several materials were tested as sources of broadband X-ray emission for backlighting in both the sub-picosecond and the sub-nanosecond laser regimes. Experiments were performed in the Phoenix vacuum chamber in a series of Leopard laser experiments. The goal is to have a continuum or quasi-continuum in the spectral range of 1.45 to 1.55 keV. The materials tested include Al, Sm, Ge, and W. It was also determined experimentally that more X-rays were created when Leopard has a 0.6 nanosecond pulse duration compared to sub-picosecond regime. At this regime, the intensity of the Leopard laser at the focal spot is (0.8-1.4) x $10^{15}$ W/cm$^2$.

Figures 4.3 (a) and (b) shows spectra of Ge and Sm plasma recorded with a cylindrical Von Hamos spectrometer 3 cm in diameter [Shevelko 2002] with a spectral resolution of ~300. Later high resolution study of Ge plasma showed that it consists of multiple closely located lines and Sm spectrum is smoother compared to Ge. For this reason a samarium target was selected for backlighting of Al plasma in the wavelength range of 8.0-8.5 Å.

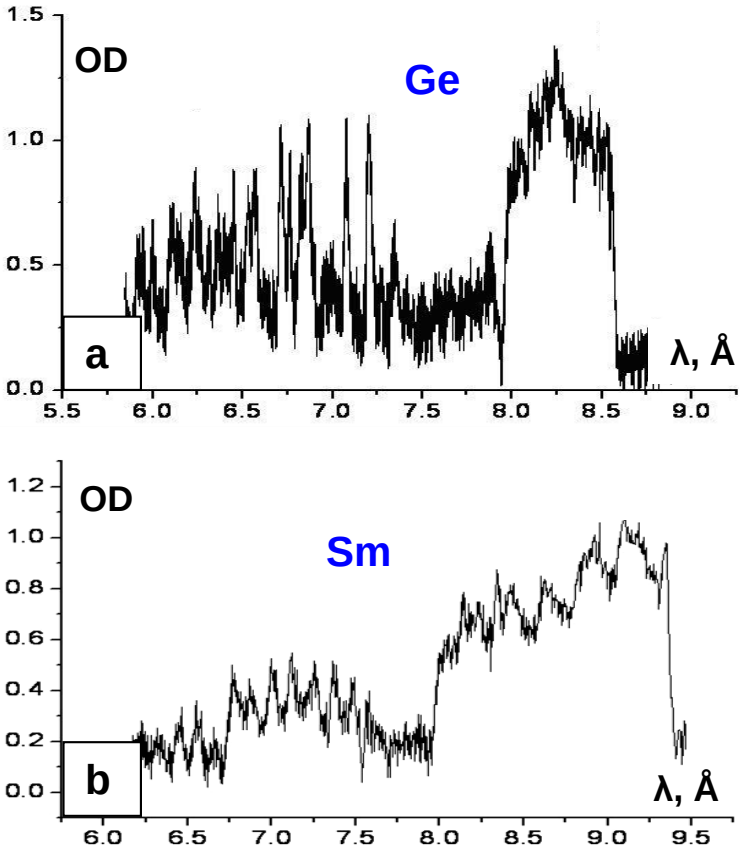


Fig. 4.3. Spectra of Ge (a) and Sm (b) laser-produced plasmas in the range of 6.0-9.5 Å.

The simplified schematic for the X-ray absorption spectroscopy diagnostic is shown in Figure 4.4. The Leopard laser beam is focused onto a 25 Sm μm-thick foil target, with a spot-size 25 μm in diameter. Two conical Van-Hamos spectrometers are

labeled S1 and S2. The spectrometers are aligned so that S1 measures the spectra as it passes through one leg of the star-like wire array, and S2 measures the backlighting spectra directly. Comparing the two allows one to measure the absorption from the plasma. Two collimators are placed in front of the conical spectrometers to geometrically block the X-ray burst of the stagnated Z-Pinch from contaminating the film. 2-frame laser shadowgraphy at the wavelength of 532 nm is used to view plasma conditions during the experiment. The first frame is simultaneous with the timing of the Leopard

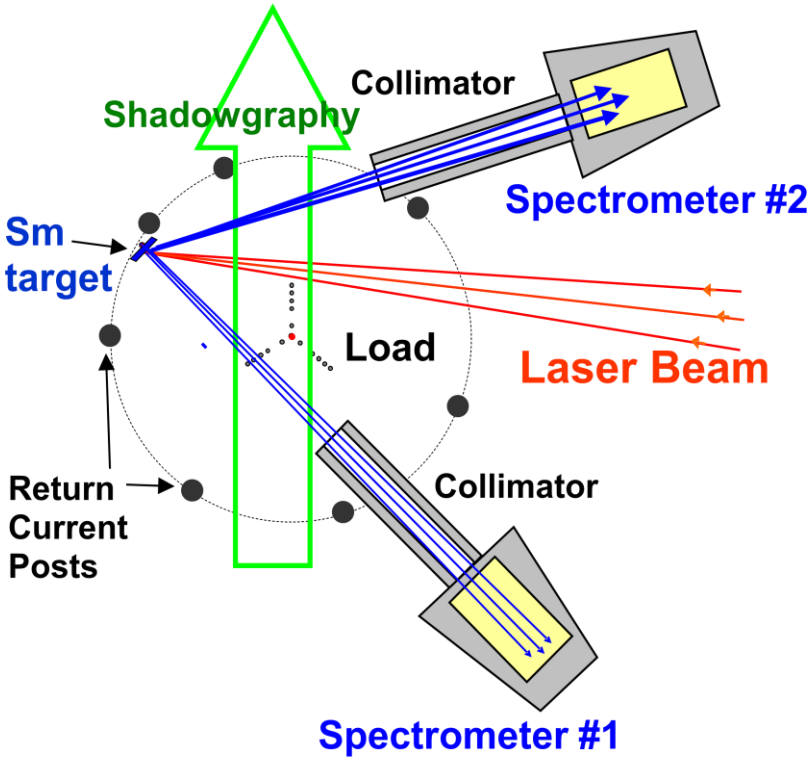


Figure 4.4. Schematic of absorption spectroscopy diagnostic using two conical spectrometers and shadowgraphy

laser shot to determine the plasma conditions, and the second frame is time 25 ns later to

study the evolution of the plasma. A picture of the experimental setup in the Zebra vacuum chamber is shown in Figure 4.5.

Van-Hamos conical X-ray spectrometers feature high efficiency in a wide spectral range, due to a large solid angle collecting radiation and then focusing it onto a focal axis. The focusing geometry of the Van-Hamos spectrometer provides high intensity of

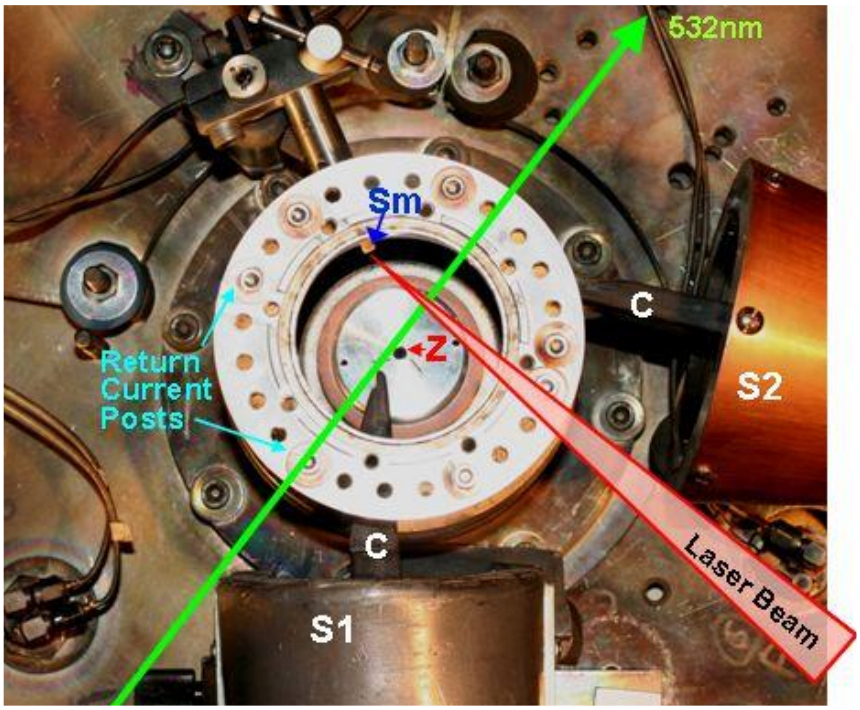


Fig. 4.5. A load area of in the vacuum chamber of the Zebra generator during coupled shots (only a bottom part of the load is installed). S1 and S2 are X-ray conical spectrometers shielded with collimators C. Z is a position of the Z-pinch during the stagnation stage. Sm is the samarium laser target. A line indicates a direction of probing for the two-frame shadowgraphy at the wavelength of 532 nm.

collected X-ray K-shell radiation in the focus line on recording film. This helps prevail the background scattered multi-kJ radiation of the main Z pinch in the vacuum chamber of the Zebra generator. A crystal plate, in this case mica (2d=19.94Å) with a thickness of 20-30 μm, is bent to the shape of the conical

spectrometer, and creates a spectral dispersion using Bragg diffraction, which as a reminder from Equation 1.8 is given as

$$m \cdot \lambda = 2d \sin\theta \tag{4.1}$$

The source of the X-rays and the detector plane lie on the axis of the conical spectrometer. The spectral dispersion for a conical spectrometer is given as

$$x = \left(\frac{D}{2\tan\alpha} + d\right)\left(\frac{\tan\alpha\,[1 - \tan\alpha\tan\beta]}{\tan\alpha + \tan\varphi}\right) - \frac{D}{2\tan\alpha} + L \tag{4.2}$$

where the parameters are given by the conical crystal spectrometer schematic given in Figure 4.6. The higher-order Bragg reflections are negligible, as the laser is not able to heat the plasma to high enough temperatures to create significant amounts of 1.6-2.8 keV X-rays. For the mica crystal, the spectral resolution $\Delta\lambda/\lambda$ is in the range of 250-300.

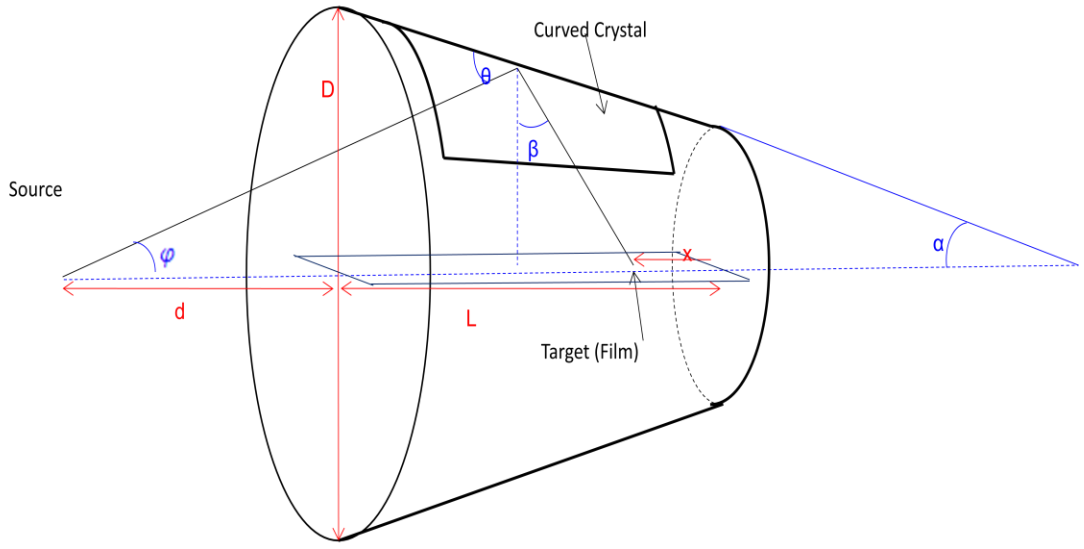


Figure 4.6. Schematic of Conical spectrometer.

The conical Van-Hamos was chosen for this experiment, as the inclined angle of

the cone contributes to the Bragg diffraction angle, effectively allowing the spectrometer to be placed further from the source when compared to a cylindrical Van-Hamos spectrometer. In this particular case, a cylindrical Van-Hamos spectrometer would need to be placed ~3 cm from the source of the X-ray emission to record the spectra being investigated by absorption spectroscopy, which is not possible due to space constraints in the Zebra chamber.

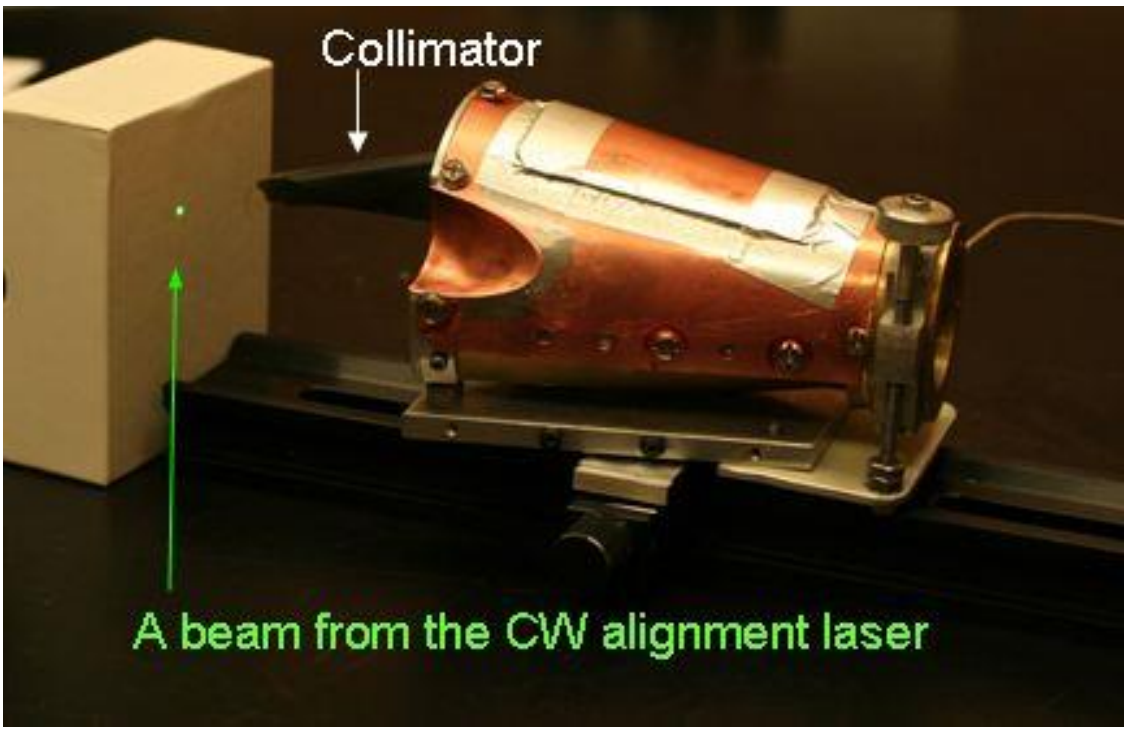


Figure 4.7. Alignment of conical spectrometer to backlighting target is performed with a CW laser inserted in the back of the spectrometer.

Spectrometers are aligned onto the focal spot of the Leopard laser using a CW laser which slides into the central cavity of the conical spectrometer as shown in Figure

4.7. After alignment, the CW laser is replaced with a film cassette containing Biomax X-ray film for recording spectra.

Cheap split sheets of mica crystal were used. The crystal was damaged by plasma debris and changed to another one every shot.

## 4.3 Initial Experiments

Star-like wire loads with 3 rays were studied during the ablation stage which typically has a 50-60 ns duration. In this stage, the wires in the array stay at the initial

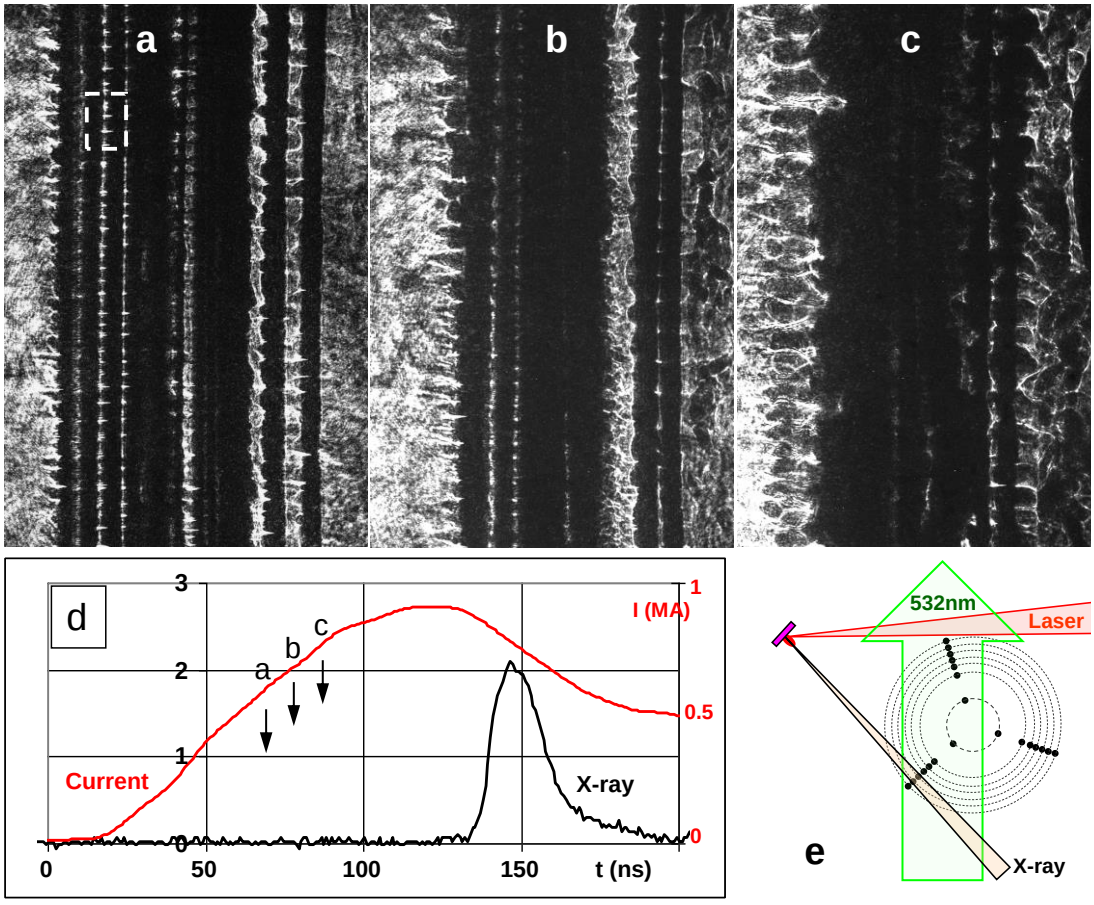


Fig. 4.8. Plasma conditions in star wire arrays at three times at the ablation stage. (a-c) Shadowgrams of wire arrays at the wavelength of 532 nm. (d) The timing diagram. (e) Direction of probing of one ray of the load.

position. Shadowgrams in Figure 4.8 present plasma of one ray of the wire array at three different currents. Plasma between wires expands and feel the gap at the later time.

Sm laser produced plasma was experimentally determined to have the best backlighting in the 1.45-1.55 keV range. The emission spectra of Sm and Al plasmas measured with a conical Van Hamos spectrometer in calibration shots as shown in Figure 4.9. A scale for backlighting spectrum was modeled using the dispersion relation in Equation 4.2. In addition calibration shots were also performed to test the backlighting spectrum in the working position of the spectrometers. Figure 4.9(a) gives the calibration of the backlighting X-rays from the Sm target with K-shell emissions from Al and Mg. The two spectra are formed by taking a Leopard-only laser shot, then shifting the Leopard laser focus 1 mm to the side and repeating the shot. Figure 4.6(b) shows the shot-to-shot variation in the spectra, measured by taken two laser only shots. At 7.95 Å, the mica crystal has a characteristic region of poor reflectivity, which can easily be seen in the spectra.

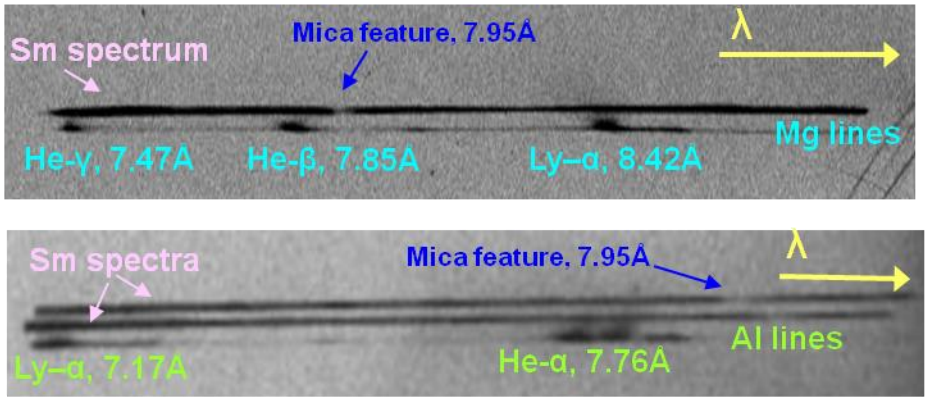


Figure 4.9. Calibration of Sm X-ray spectrum with Al and Mg spectral lines from Al 5056 alloy. Spectra also revealing shot-to-shot variation in Sm backlighting

Filters were placed on the spectrometers in order to attenuate X-ray radiation. The filters used were 10 micron Mylar coated with 0.3 microns of Al film. The transmission rates of filters were calculated using online data of the Center for X-ray Optics, LBL.

In addition, calibration was also done before each Zebra-Leopard coupled shot. Each spectrometer has a Leopard laser-only reference spectrum, and a Zebra-Leopard coupled shot spectrum, for a total of four spectra. Figure 4.10 shows a Leopard only and Zebra-Leopard coupled spectra. The coupled spectrum from S1 is the absorption spectrum, while S2 provides an addition in-shot reference spectrum to record shot-to-shot spectral variations for the backlighting source.

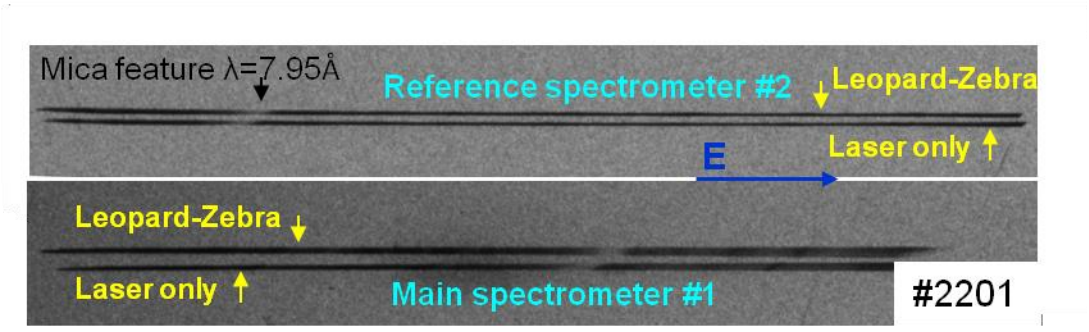


Figure 4.10. Spectra from spectrometers S1 and S2. Each film has a laser only reference spectrum and experimental Leopard-Zebra coupled spectrum

### 4.4. K-Shell Absorption Spectroscopy applied to Star-like Wire Arrays during the Ablation Stage

Star-like wire arrays with three rays and 18 total wires were investigated using the X-ray absorption spectroscopy. The wires are made of aluminum alloy 5056 and have a

diameter of 12.7 μm. The six wires in each ray, were located 10/9.25/8.5/7.75/7/3 mm from the center of the load. Wire arrays were 2 cm tall. We used wire-array loads which radiated 5-8 kJ of the total X-ray energy [Ivanov 2012]. This makes experiments very complicated due to strong X-ray background in the vacuum chamber of the Zebra generator. However, the plasma conditions like the electron density and temperature in our experiments are relevant to real high-energy Z pinches.

The wire arrays were studied during the ablation stage when the wire locations remain stationary. The S1 spectrometer was aligned to investigate the plasma in one ray of the star wire array, while the S2 was aligned to avoid the wire array and measure the backlighting reference spectra directly. This spectrum was used to estimate the shot-to-shot variations in backlighting spectra.

Figure 4.11 shows optical and X-ray data from shot 2204. The timing diagram in

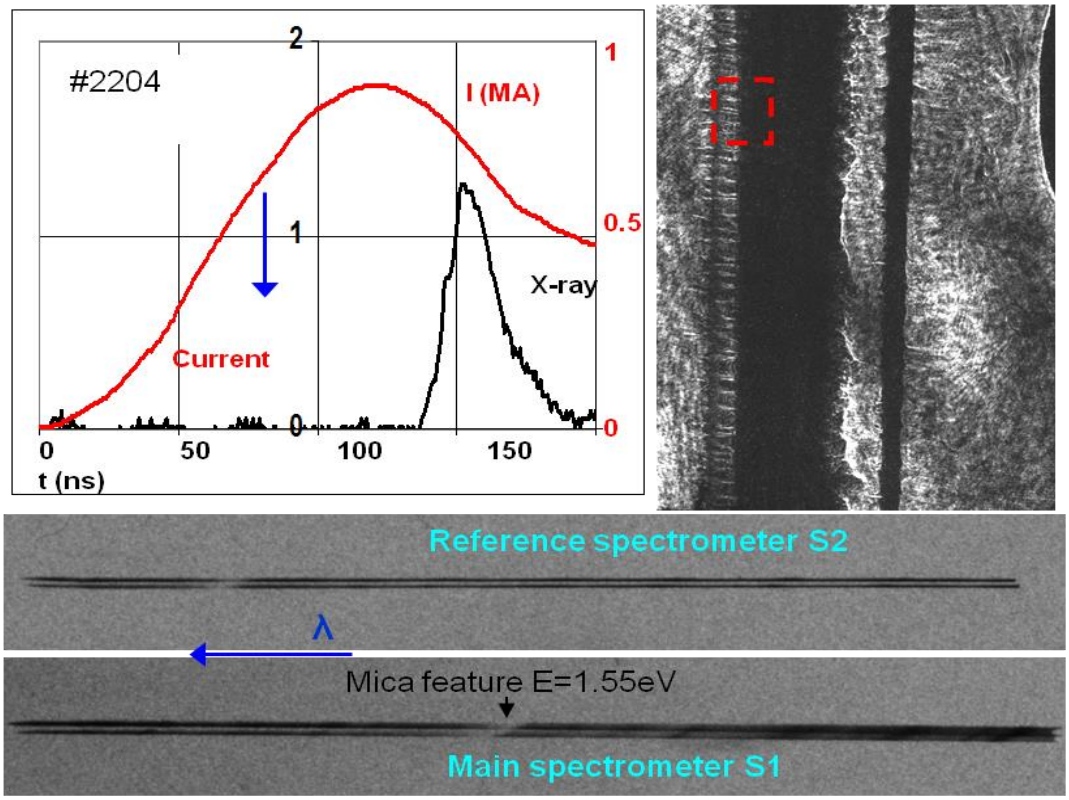


Figure 4.11. (a) Shot #2204 Timing diagram showing current (red), stagnated Z-pinch X-ray pulse (black) and timing of Leopard laser and shadowgraphy (arrow). (b) Shadowgraph taken at the time of Leopard pulse showing plasma conditions and (c) spectra recorded by conical spectrometers.

Figure 4.11(a) shows the current pulse of the Zebra generator (red), X-ray pulse from the Z-Pinch (black), and the timing of the laser shadowgraphy and Leopard laser (arrow). The shadowgram in Figure 4.11(b) shows the plasma structure at the time. The red box illustrates the FOV measured by the X-ray absorption spectroscopy, which is 1.1 mm in the horizontal direction. Figure 4.11(c) shows the spectra recorded by two conical spectrometers. Both the reference spectrometer and main spectrometer record spectra

from the laser-only shot and spectra from the Coupled Zebra-Leopard shot. Sm spectrum was calibrated using data from [Louzon 2009] shown in Figure 4.12.

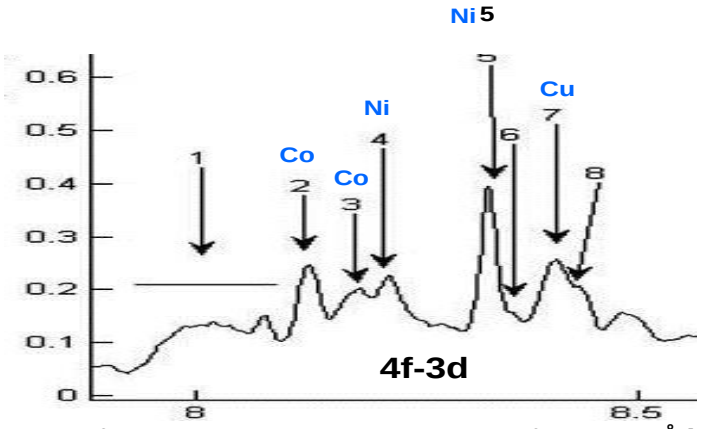


Fig. 4.12. Spectrum of Sm laser-produced plasma spectra from 8-8.5 Å [Louzon 2009].

Two lines on each film represent the reference Leopard-only shot and the Zebra-Leopard coupled experimental shot. Background intensity is removed during the processing of the spectra. Figure 4.13 shows the processed spectra for experimental shot #2204. Spectrum from S2 spectrometer shows a small variation between the Leopard only and Zebra-Leopard coupled shots. A comparison of the reference and experimental spectra from S1 shows absorption in the region of 8.3-8.5 Å, or 1450-1500 eV.

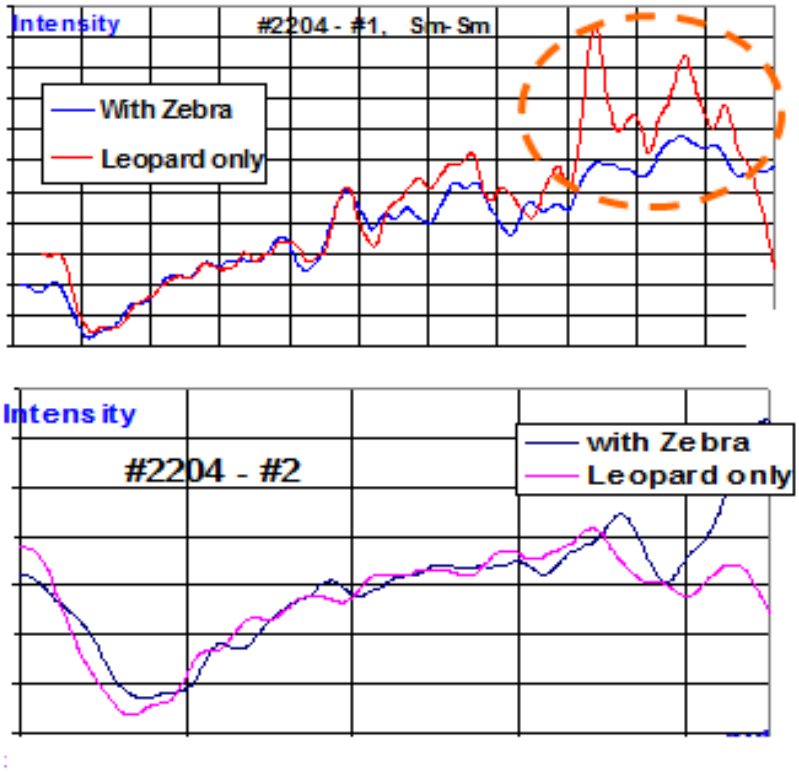


Figure 4.13. Reference and experimental spectra from absorption spectrometer S1 (top) and reference spectrometer S2 (bottom). Reference spectrometer S2 shows a small enough shot-to-shot variation, while S1 shows absorption highlighted by red circle.

Figure 4.14 shows the transmission for shot #2204 and #2207 averaged together. The absorption red line correspond to the F, O, N, and C spectral lines for K-shell of Al plasma. The experimental transmission was the base for atomic simulations which were carried out in the research group of Prof. R. C. Mancini using PrismSPECT and Spect3D programs. The spectrum is integrated for the 1.1 mm box shown in Figure 4.11(b). This includes both the dense wire cores and the coronal plasma. A single-temperature model is shown in dotted blue for Figure 4.14. The one-temperature model does not fit adequately the F-like and C-like absorption lines. It was then determined that the spectra represented

a distribution of electrons temperatures and could not be successfully modeled with a single temperature. A two-temperature model was introduced, with effective electron temperatures $T_{e1}$ and $T_{e2}$. A two temperature model with 14 eV and 30 eV is plotted as the black line in Figure 4.9. The model consists of 84% of the lower 14 eV plasma, and 16% of the 30 eV plasma. The calculated areal density is $1.4 \times 10^{18}$ $cm^{-2}$. This does not include contributions from plasma not involved in the absorption.

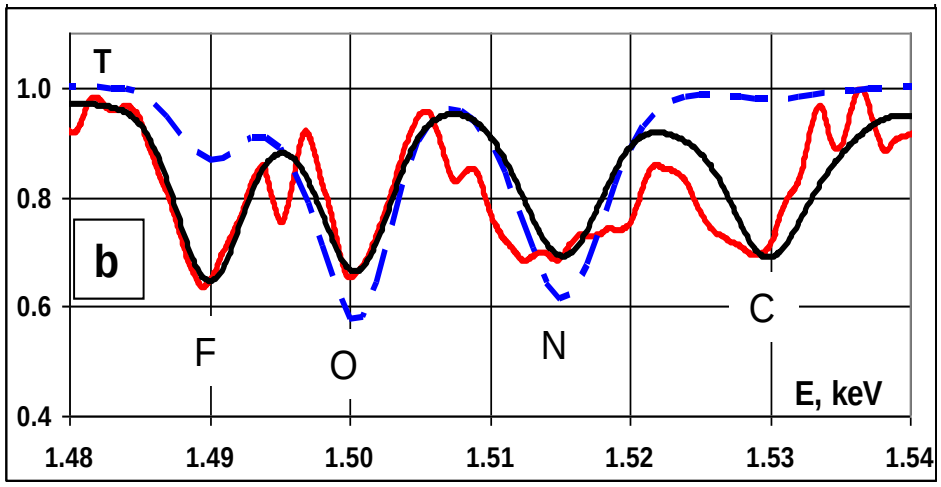


Figure 4.14. Averaged experimental absorption spectra for shots #2204 and #2207 (red). A one temperature model (blue) cannot account for all spectral lines. A two temperature model with 14 eV and 30 eV plasma is used instead (black)

Another experimental shot, #2282, was also investigated, and is shown in Figure 4.15. Figure 4.15 shows the experimental transmission rates for the reference spectrometer S2 (green line, top) and experimental spectrometer S1 (red line, bottom). The transmission in the reference spectrometer reveals a 10% error, of which shot-to-shot variation for the background spectra is the major cause.

Atomic simulations (Prof. R.C. Mancini) with a two-temperature plasma model were applied to model the experimental absorption spectrum seen in spectrometer S1.

Simulations fit experimental curve if plasma consists of 15 eV plasma and 26 eV plasma, with the cooler 15 eV comprising of 84% of the total plasma. The areal density of the ions is calculated to Ni= 2.1 x $10^{18}$ under the assumption that 70% of the coronal plasma stays within 4 mm of the wire core over the course of the probing.

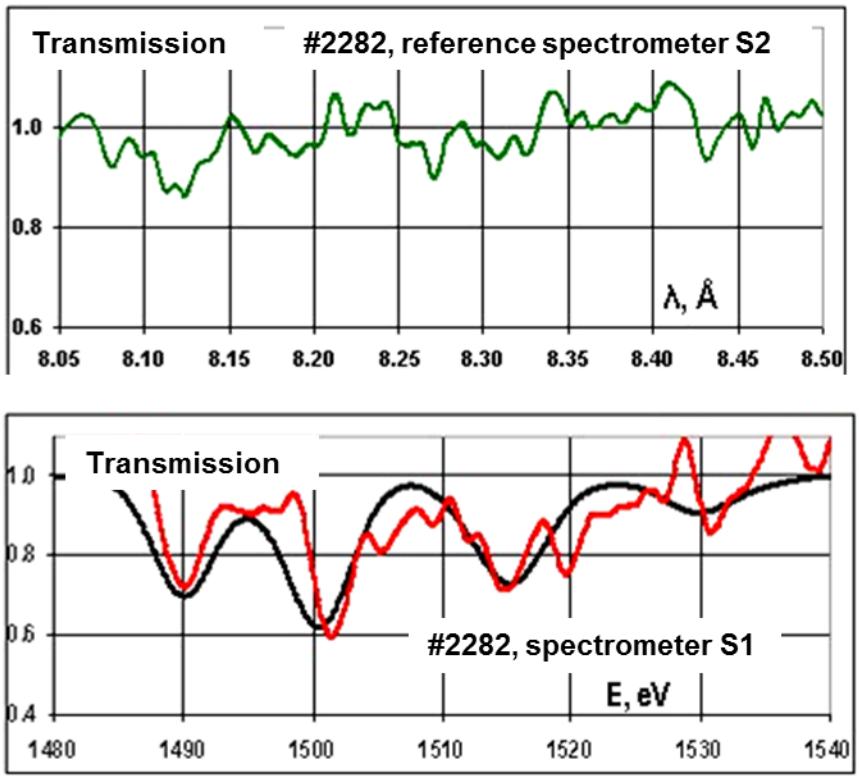


Figure 4.15. Shot #2282. Transmission for reference spectrometer (top) and absorption spectrometer. Error in reference transmission is caused by shot-to-shot variations in backlighting spectra. The experimental absorption spectrum (red) is modeled using two temperature plasmas, 15 eV and 26 eV (black)

### 4.5 MHD Modeling of the Ablation Stage of Star-like Wire Arrays

MHD modelling of plasma in our star wire arrays were performed in the group of Prof. J. Chittenden in Imperial College, London. This modelling approved the plasma parameters derived with atomic models. The 3D MHD program Gorgon was used to simulate the ablation stage of an Al wire array Z-Pinch to compare with experimental data. Gorgon is a 3D resistive MHD code, which was used in 2D geometry with 20 micron spatial resolution. Figure 4.16 shows the wire array plasma during the ablation stage. The mass density reveals the location of the wire cores and reveals some structure from the ablating plasma. The second image is a top-down cross-section view of the electron temperature. Cool plasma can be seen in the inner regions, surrounded by the hotter coronal plasma on the outside.

The temperature and density of wire-array plasma from the MHD modelling were post-processed with a Spect3D program to compare it with experimental data. Photons were across the ablating wire array along the dotted arrow in Figure 4.16. The transmission for each energy photon was calculated along path along the arrow and then integrated together. The measured transmissions were broadened to the spectral resolution seen in the experimental instrumentation. Absorption is still dominated along the F, O, and N spectral lines for K-shell Al. Like experimental data, a two-temperature effective model was created to model the plasma. The two effective electron temperatures used to model the absorption spectra were 14 eV and 27 eV. This post-processing of the Gorgon code calculated the plasma areal density as $1.9 \times 10^{17}$ $cm^{-2}$, of which 94% 14 eV and 6% to the 27 eV plasma [Ivanov 2011b].

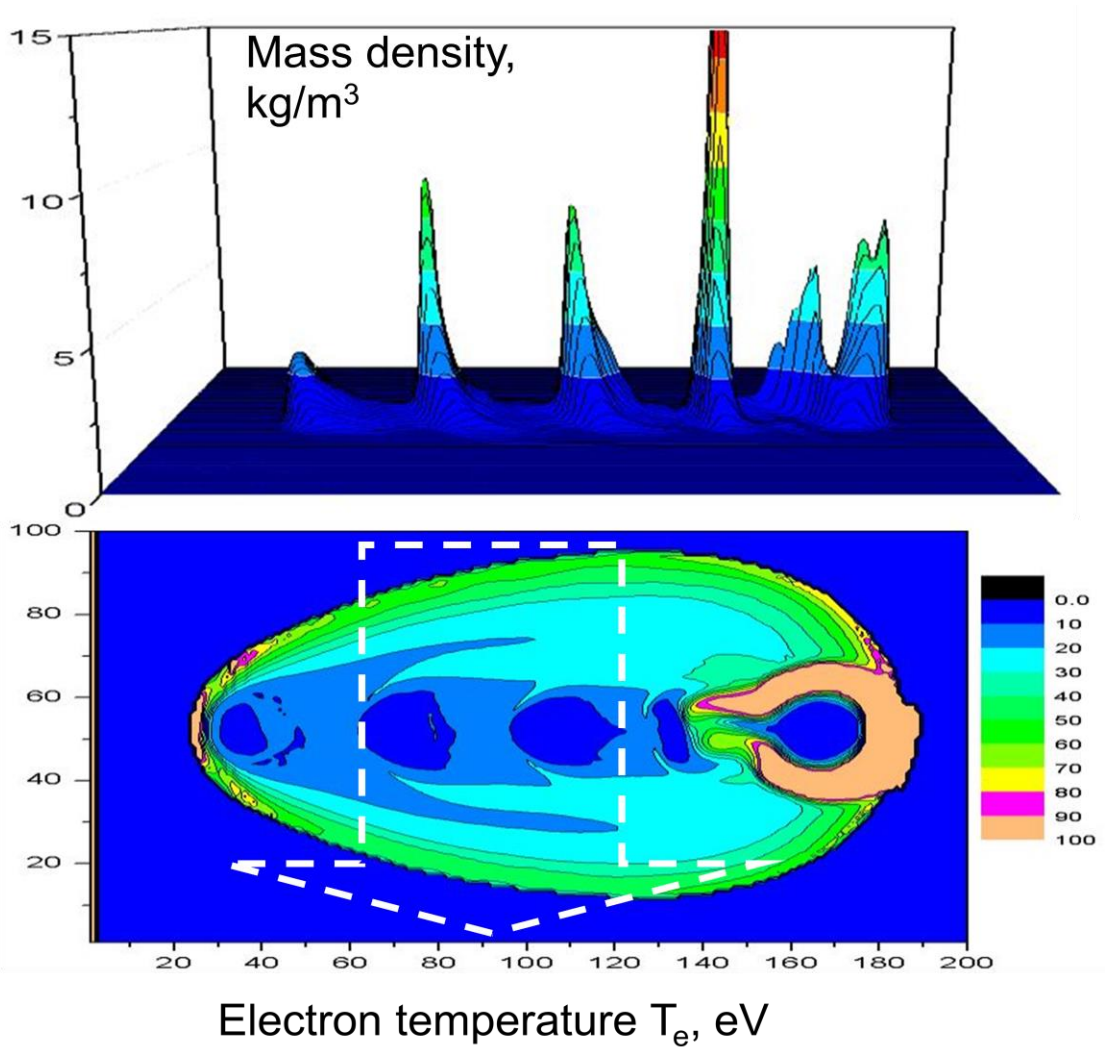


Figure 4.16. 2D Gorgon MHD modeling of mass density and electron temperature for a single ray in a star-like array during ablation stage. Cooler temperature plasma is surrounded by a layer of less-dense, higher-temperature plasma.

The simulated spectra are in an agreement with the experimental results. The absorption reveals the majority of the plasma consists of low temperature plasma, with a smaller contribution from higher temperature plasma. The plasma columns seen in the shadowgram in Figure 4.11(b) reveal larger plasma in the interwire gaps than seen in the

MHD simulation in Figure 4.16, which could contribute to the different proportions between the low and high temperature plasmas seen in the two-temperature models.

This work signifies the first successful use of absorption spectroscopy to measure the electron temperature and areal density of plasma during the ablation stage of the 1 MA wire array Z-Pinch. Simultaneous fielding of laser shadowgraphy allows for the understanding of plasma structure at the timing of the absorption spectroscopy. The experimental work was carried in a close collaboration with a research group for atomic modelling (Prof. R. C. Mancini, UNR) and a group for MHD simulations of wire array plasma (Prof. J. Chittenden, Imperial College). These allowed for a full analysis of experimental data and measuring plasma parameters in wire arrays at the non-radiative ablation stage.

# Chapter 5

# Conclusion

Wire arrays in the ablation and implosion stage were studied using UV laser and X-ray diagnostics. The upgraded 266 nm UV laser offers several advantages over the 532 nm laser. The shorter wavelength reduces Bremsstrahlung absorption and refraction from plasma electron density gradients. For application in laser interferometry diagnostic, the UV laser phase shift is less sensitive to electron density, allowing it to measure denser plasma than the 532 nm laser probe. Similarly, the Faraday rotation of the laser beam as it travels through a magnetized plasma is also reduced, allowing it to measure stronger magnetic fields or denser plasmas, or a combination of both.

UV interferometry at the wavelength of 266 nm was used to measure the electron plasma density $N_e$ during ablation and implosion stages of the Z-Pinch. In shot #2883, UV interferometry was used to measure the electron density profile of aluminum wires in a cylindrical wire array during the ablation stage. This was the first direct measurement of plasma density in the ablating wire core. The analysis used Abel inversion, which assumed a cylindrically symmetric plasma column. The UV laser was able to measure up to a maximum density of (1-3) x $10^{20}$ $cm^{-3}$. One wire was transparent to UV laser, allowing us measure the electron density for almost the entire wire core. Two-frame interferometry was applied to investigate the expansion rate of plasma from the wire array, which revealed plasma with electron density of $10^{20}$ $cm^{-3}$ expanding at a rate of 2.4 x $10^5$ cm/s. This is

similar to the expansion rate of 2 x $10^5$ cm/s the dense wire core measured by Lebedev using X-ray radiography [Lebedev 2000].

During the implosion stage of shot #2816, an aluminum linear wire array, fingers of trailing plasma left behind by the inhomogeneous implosion were investigated using UV interferometry. It revealed the presence of lower electron density plasma of $10^{18}$ to $10^{19}$ $cm^{-3}$ in the regions between the denser plasma bubbles. This low density plasma may serve as an alternate pathway for the current to switch to and implode the trailing mass.

UV Faraday rotation diagnostics with an accompanying interferogram and shadowgram measured the magnetic field strength of a star-like wire array with three rays extending radially. A strong Faraday effect was seen along two imploding plasma columns formed by two overlapping plasma columns from two of these ray. The plasma electron density and rotation angle were measured from the shadowgram, interferogram, and reference images. Abel inversion was applied to reconstruct the magnetic field in the imploding plasma. This magnetic field profile can be analyzed with a simple model of 0.6 MA current with a uniform cylindrical current with radius 0.8mm. This is first measurement of current distribution during the implosion stage in 1-MA wire-array Z-Pinches.

X-ray imaging was used to investigate the dense solid-liquid wire cores during the ablation stage. A 50-TW Leopard laser was used as a backlighter in coupled experiments with the Zebra pulsed power generator. Laser-based radiography allows for a flexible delay and can be applied to any stage of wire-array Z-Pinch. A spherically-bent quartz 1011 crystal successfully imaged the wire cores with ~15 micron resolution. Wires in a

cylindrical wire array and the outermost wires in a star-like load revealed a wire core expansion of 1 x $10^5$ cm/s. This expansion is slightly slower than the expansion of the densest plasma measurable by the UV interferometry. X-ray radiography delivered data which is complementary to data derived by UV interferometry. Coupled X-ray imaging and UV shadowgraphy/interferometry provide a complementary diagnostic set which allows the investigation of a wide range of plasma electron densities.

X-ray absorption spectroscopy was applied, at the first time, to wire-array Z pinches. A Leopard laser was used for broadband X-ray backlighting of star wire arrays at the ablation stage. Optimal materials for the laser target were selected in preliminary experiments. Laser-produced plasma from Sm foil provided X-ray probing in the range of 8 - 8.5 Å. The electron temperature and areal density were measured, using two conical Von Hamos spectrometers with mica crystals which recorded absorption and reference spectra with each shot. Combined with shadowgraphy from probing lasers, one can acquire detailed information about the morphology and detailed state of the plasma. Absorption was seen in the region between 8.2 and 8.4 Å. Experimental data were processed in the group of Prof. R. C. Mancini (UNR) using modern atomic codes. MHD simulations were carried out with a Gorgon code in the group of Prof. J. Chittenden (Imperial College, London). It was found, that absorption spectra could not be adequately described using single temperature models, and so a two-temperature model was used instead. For the averaged spectra for shots #2204 and #2207, calculations gave a total areal density 1.4 x $10^{18}$ $cm^{-2}$, which was modeled using a combination of two plasmas with an electron temperature of 14 eV plasma (84%) and 30 eV plasma (16%). Another shot, #2282 also had absorption, which was modeled using a two temperature plasma

with 84% 15eV plasma and 16% 26 eV plasma. These temperatures are in general agreement with post-processed two-temperature modeling of simulations performed with the Gorgon resistive MHD code, which predicted a total areal density of $1.9 \times 10^{17}$ $cm^{-2}$ characterized by 15 eV plasma (94%) and 27 eV plasma (6%). The lower areal density seen in the Gorgon simulation could be contributed by the non-participated plasma in the experiment. Also shadowgrams reveal larger wire core diameters than those seen in Gorgon simulations.

# Bibliography

**[Aglitskiy 1999]** Aglitskiy, Y., T. Lehecka, S. Obenschain, C. Pawley, C. M. Brown, and J. Seely. "X-ray Crystal Images for Inertial Confinement Fusion Experiments (invited)." Review of Scientific Instruments 70, 1 (1999).

**[Ampleford 2008]** Ampleford, D. J., B. Jones, S. C. Bott, S. V. Lebedev, S. N. Bland, G. N. Hall, and J. B. A. Palmer. "Radiography of Modulated Wire Array Z-Pinches." IEEE Transactions on Plasma Science 36, 4 (2008).

**[Audebert 2005]** P. Audebert, P. Renaudin, S. Bastiani-Ceccotti, et al., Phys. Rev. Lett. 94 (2005) 025004.

**[Bailey 2007]** J.E. Bailey, G.A. Rochau, C.A. Iglesias, et al., Physical Review Letters 99 (2007) 265002.

**[Bauer 1999]** Bauer, B. S., V. L. Kantsyrev, N. Le Galloudec, R. Presura, G. S. Sarkisov, A. S. Shlyaptseva, S. Batie, W. Brinsmead, H. Faretto, B. Le Galloudec, A. Oxner, M. Al-Shorman, D. A. Fedin, S. Hansen, I. Paraschiv, H. Zheng, and D. McCrorey. "Two-Terawatt Zerbra Z-Pinch at the Nevada Terawatt Facility." Pulsed Power Conference, 1999. Digest of Technical Papers. 12th IEEE International 2 (1999): 1045-047.

**[Bennett 1934**] Bennett, W.H. "Magnetically Self-Focusing Streams." Physical Review 45 (1934): 890-97.

**[Blesener 2009]** Blesener, I. C., J. B. Greenly, S. A. Pikuz, T. A. Shelkovenko, S. Vishniakou, D. A. Hammer, and B. R. Kusse. "Axial X-ray backlighting of wire array Z-Pinches using X pinches." Review of Scientific Instruments 80, 123505 (2009).

**[Chuvatin 2009]** A. S. Chuvatin, V. L. Kantsyrev, L. I. Rudakov, M. E. Cuneo, A. L. Astanovitskiy, R. Presura, A. S. Safranova, A. A. Esaulov, W. Cline, K. M. Williamson,

I. Shrestha, M. F. Yilmaz, G. C. Osborne, M. Weller, T. Jarrett, B. LeGalloudec, V. Nalajala, T. D. Pointon, and K. A. Mikkelson, “Design and Testing of a Load Current Multiplier on Zebra Facility”, AIP Conference Proceedings 1088, 253 (2008)

**[Cuneo 2001]** M. E. Cuneo, R. A. Vesey, J. L. Porter, Jr., G. A. Chandler, D. L. Fehl, T. L. Gililand, D. L. Hanson, J. S. McGurn, P. G. Reynolds, L. E. Ruggles, H. Seamen, R. B. Spielman, K. W. Struve, W. A. Stygar, W. W. Simpson, J. A. Torres, D. F. Wenger, J. H. Hammer, P. W. Rambo, D. L. Peterson and G. C. Idzorek "Development and characterization of a Z-Pinch-driven hohlraum high-yield", Physics of Plasmas 8, 2257 (2001)

**[Cuneo 2012]** Cuneo M. E., M. C. Herrmann, D. B. Sinars, S. A. Slutz, W. A. Stygar, R. A. Vesey, A. B. Sefkov, G. A. Rochau, G. A. Chandler, J. E. Bailey, J. L. Porter, R. D. McBride, D. D. Rovang, M. G. Mazarakis, E. P. Yu, D. C. Lamppa, K. J. Peterson, C. Nakhleh, S. B. Hansen, A. J. Lopez, M. E. Savage, C. A. Jennings, M. R. Martin, R. W. Lemke, B. W. Atherton, I. C. Smith, P. K. Rambo, M. Jones, M. R. Lopez, P. J. Christenson, M. A. Sweeney, B. Jones, L. A. McPherson, E. Harding, M. R. Come, P. F. Knapp, T, J. Awe, R. J. Leeper, C. L. Rui, G. W. Cooper, K. D. Hahn, J. McKenney, A. C. Owen, G. R. McKee, G. T. Leifeste, D. J. Ampleford, E. M. Waisman, A. Harvey-Thompson, R. J. Kaye, M. H. Hess. S. E. Rosenthal, and M. K. Matzen. “Magnetically Driven Implosions for Inertial Confinement Fusion at Sandia National Laboratories.” IEEE Transactions on Plasma Science 40, 12 (2012).

**[Deeney 1998]** Deeney, C., M. R. Douglas, R. B. Spielman, T. J. Nash, D. L. Peterson, P. L'Eplattenier, G. A. Chandler, J. F. Seamen, and K. W. Struve. "Enhancement of X-ray Power from a Z Pinch Using Nested-Wire Arrays." Physical Review Letters 81, 22 (1998).

**[Grabovskii 2004]** Grabovskii, E. V., K. N. Mitrofanov, G. M. Oleinik, and I. Yu. Porofeev. "X-ray Backlighting of the Periphery of an Imploding Multiwire Array in the Angara-5-1 Facility." Plasma Physics Reports 20, 2 (2004): 121-127.

**[Haines 2011]** Haines, M. G. "A Review of the Dense Z-Pinch." Plasma Physics and Controlled Fusion 53 (2011): 093001.

**[Hecht 2002]** *Optics*, Addison-Wesley, 2002 Print

**[Hutchinson 2002]** I. H. Hutchinson, Principles of Plasma diagnostics, 2nd. ed. (Cambridge University Press, Cambridge, UK, 2002)

**[Ivanov 2006a]** Ivanov, V. V., V. I. Sotnikov, G. S. Sarkisov, T. E. Cowan, S. N. Bland, B. Jones, C. A. Coverdale, C. Deeney, P. J. Laca, A. L Astanovitskiy, and A. Haboub. "Dynamics of Mass Transport and Magnetic Fields in Low-Wire-Number-Array Z Pinches." Physical Review Letters 97 125001 (2006).

**[Ivanov 2006b]** Ivanov, V. V., G. S. Sarkisov, P. J. Laca, V. I. Sotnikov, V. L. Kantsyrev, B. M. Jones, A. Coverdale, D. LePell, C. Deeney, K. W. Struve, A. L Astanovitskiy, D. A. Fedin, B. Le Galloudec, V. Nalajala, I. Shrestha, and T. E. Cowan. "Investigation of Magnetic Fields in 1-MA Wire Arrays and X-Pinches." IEEE Transactions on Plasma Science 34, 5 (2006).

**[Ivanov 2007a]** Ivanov, V. V., V. I. Sotnikov, G. S. Sarkisov, A. L Astanovitskiy, P. J. Laca, T. E. Cowan, B. Jones, C. Deeney, B. V. Oliver, and T. A. Mehlhorn. "Experimental Study of the Dynamics of Large- and Small-Scale Structures in the Plasma Column of Wire Array Z-Pinches." IEEE Transactions on Plasma Science 35, 4 (2007).

**[Ivanov 2007b]** Ivanov, V. V., V. I Sotnikov, A. Haboub, G. E. Sarkisov, R. Presura, and T. E. Cowan. "Investigation of ablation and implosion dynamics in linear wire arrays." Physics of Plasmas 14, 032703(2007).

**[Ivanov 2008]** Ivanov, V. V., V. I. Sotnikov, A. Haboub, A. P. Shevelko, A. L. Astanovitskiy, A. Morozov, E. D. Kazakov, and S. D. Altemara. "Mitigation of the Plasma-Implosion Inhomogeneity in Starlike Wire-Array Z Pinches." Physical Review Letters 100, 025004 (2008).

**[Ivanov 2009]** V. V Ivanov, V. I. Sotnikov, J. M. Kindel, P. Hakel, R. C. Mancini, A. L. Astanovitskiy, A. Haboub, S. D. Altemara, A. P. Shevelko, E. D. Kazakov, and P. V. Sasorov, "Implosion dynamics and X-ray generation in small-diameter wire-array Z pinches", Physical Review E 79, 056404 (2009)

**[Ivanov 2011a]** V.V. Ivanov, J.P. Chittenden, S.D. Altemara, N. Niasse, P. Hakel, R.C. Mancini, D. Papp, A.A. Anderson, Study of the Internal Structure and Small-Scale Instabilities in the Dense Z Pinch, Physical Review Letters 107, 165002 (2011)

**[Ivanov 2011b]** V. V Ivanov, P. Hakel, R.C. Mancini, J.P. Chittenden, A. Anderson, A.P. Shevelko, P. Wiewior, T. Durmaz, S.D. Altemara, D. Papp, A.L. Astanovitskiy, V. Nalajala, O. Chalyy, O. Dmitriev, "X-ray absorption spectroscopy for wire-array Z-Pinches at the non-radiative stage", High Energy Density Physics 7, 383-390 (2011)

**[Ivanov 2012]** Ivanov, V. V., J. P. Chittenden, R. C. Mancini, D. Papp, N. Niasse, S. D. Altemara, and A. A. Anderson. "Investigation of plasma instabilities in the stagnated Z pinch." Physical Review E 00, 006400 (2012).

**[Ivanov 2014]** Ivanov, V. V., A. A. Anderson, D. Papp, B. R. Talbot, J. P. Chittenden, N. Niasse, and I. A. Begishev. "UV Laser-Probing Diagnostics for the Dense Z Pinch." ." IEEE Transactions on Plasma Science 42, 5 (2014).

**[Johnson 1973]** T.W. Johnson, J.M. Dawson, “Correct values for high-frequency power absorption by inverse bremsstrahlung in plasma”, Physics of Fluids 16, 5, p. 722, May 1973

**[Kalantar 1993]** Kalantar, D. H., and D. A. Hammer. “Observation of a Stable Dense Core within an Unstable Coronal Plasma in Wire-Initiated Dense Z-Pinch Experiments.” Physical Review Letters 71, 23 (1993).

**[Lawson 1957]** Lawson J D Proceedings of the Physical Society of London 6, 870 1957

**[Lebedev 1999]** Lebedev, S.V., R. Aliaga-Rossel, S. N. Bland, J. P. Chittenden, A. E. Dangor, M. G. Haines, I. H. Mitchell. “The dynamics of wire array Z-Pinch implosions”, Physics of Plasma 6, 5 (1999)

**[Lebedev 2000]** Lebedev, S. V., F. N. Beg, S. N. Bland, J. P. Chittenden, A. E. Dangor, M. G. Haines, S. A. Pikuz, and T. A. Shelkovenko. "Effect of Core-Corona Plasma Structure on Seeding of Instabilities in Wire Array Z Pinches." Physical Review Letters 85, 1 (2000).

**[Lebedev 2001a]** Lebedev, S. V., F. N. Beg, S. N. Bland, J. P. Chittenden, A. E. Dangor, M. G. Haines, K. H. Kwek, S. A. Pikuz, and T. A. Shelkovenko. "Effect of Discrete Wires on the Implosion Dynamics of Wire Array Z Pinches." Physics of Plasmas 8, 8 (2001).

**[Lebedev 2001b]** Lebedev, S. V., F. N. Beg, S. N. Bland, J. P. Chittenden, A. E. Dangor, M. G. Haines, M. Zakaullah, S. A. Pikuz, T. A. Shelkovenko, and D. A. Hammer. “X-ray backlighting of wire array Z-Pinch implosions using X pinch.” Review of Scientific Instruments 72, 1 (2001).

**[Lebedev 2002]** Lebedev, S. V., F. N. Beg, S. N. Bland, J. P. Chittenden, A. E. Dangor, and M. G. Haines. "Snowplow-like behavior in the implosion phase of wire array Z pinches." Physics of Plasmas 8, 5 (2002).

**[Martin 1970]** Martin J C 1970 Nanosecond pulse technique AWE Aldermaston International Report SSWA JCM/704/49

**[Martinolli 2004]** Martinolli, E., M. Koenig, J. M. Boudenne, E. Perelli, D. Batani, and T. A. Hall. "Conical crystal spectrograph for high rightness X-ray Kα spectroscopy in subpicosecond laser-solid interation." Review of Scientific Instruments 75, 6 (2004).

**[Pikuz 1999]** Pikuz, S. A., T. A. Shelkovenko, D. B. Sinars, J. B. Greenly, Y. S. Dimant, and D. A. Hammer. "Multiphase Foamlike Structure of Exploding Wire Cores." Physical Review Letters 83, 21 (1999).

**[Sanford 1996]** Sanford, T. W. L., G. O. Allshouse, B. M. Marder, T. J. Nash, R. C. Mock, R. B. Spielman, J. F. Seamen, J. S. McGurn, D. Jobe, T. L. Gilliland, M. Vargas, K. W. Struve, W. A. Stygar, M. R. Douglas, M. K. Matzen, J. H. Hammer, J. S. De Groot, J. L. Eddleman, D. L. Peterson, D. Mosher, K. G. Whitney, J. W. Thornhill, P. E. Pulsifer, J. P. Apruzese, and Y. Maron. "Improbed Symmetry Greatly Increases X-ray Power from Wire-Array Z-Pinches." Physical Review Letters 77, 25 (1996).

**[Sanford 2007]** Sanford, T. W. L., C. A. Jennings, G. A. Rochau, S. E. Rosenthal, G. S. Sarkisove, P. V. Sasorov, W. A. Stygar, L. F. Bennett, D. E. Bliss, J. P. Chittenden, M. E. Cuneo, M. G. Haines, R. J. Leeper, R. C. Mock, T. J. Nash, and D. L. Peterson. "Wire Initiation Critical for Radiation Symmetry in Z-Pinch-Driven Dynamic Hohlraums." Physical Review Letters 98, 065003 (2007).

**[Sarkisov 1996]** Sarkisov, G. S. "Shearing Interferometer with an Air Wedge for the Electron Density Diagnostics in a Dense Plasma." Instruments and Experimental Techniques 39, 5 (1996): 727-31.

**[Sarkisov 2007]** G. S. Sarkisov, S. E. Rosenthal, K.W. Struve, T. E. Cowan, T. Presura, A. L. Astanovitskiy, A. Haboub, and A. Morozov, "Initiation of aluminum wire array on the 1-MA ZEBRA accelerator and its effect on ablation dynamics and X-ray yield", Physics of Plasmas 14, 112701 (2007)

**[Schott 2003]** R. Schott, F. Philippe, P. Angelo, et al., J. Quant. Spectrosc. Radiat. Transf. 81
(2003) 441.

**[Shevelko 1998]** Shevelko, A. P., "X-ray spectroscopy of laser-produced plasmas using a von Hamos spectrograph" SPIE 3406, (1998)

**[Shevelko 2002]** Shevelko, A. P., Yu. S. Kasyanov, O. F. Yakushev, and L. V. Knight. "Compact focusing von Hamos spectrometer for quantitative X-ray spectroscopy." Review of Scientific Instruments 73, 10 (2002).

**[Sinars 2003]** Sinars, D. B., G. R. Bennett, D. F. Wenger, M. E. Cuneo, and J. L. Porter. "Evaluation of bent-crystal X-ray backlighting and microscopy techniques for the Sandia Z machine." Applied Optics 42 19 (2003).

**[Sinars 2005]** Sinars, D. B., M. E. Cuneo, B. Jones, C. A. Coverdale, T. J. Nash, M. G. Mazarakis, J. L. Porter, C. Deeney, D. F, Wenger, R. G. Adams, E. P. Yu, D. E. Bliss, and G. S. Sarkisov. "Measurements of the mass distribution and instability growth for wire array Z-Pinch implosions driven by 14-20 MA." Physics of Plasmas 12 (2005): 056303.

**[Spielman 1995]** R. B. Spielman, “Diamond photoconducting detectors as high power zpinch diagnostics”, Review of Scientific Instruments 66, p. 867 (1995)

**[Wiewior 2010]** Wiewior, P. P., V. V. Ivanov, and O. Chalyy. “Development of the 50 TW laser for joint experiments with 1 MA Z-Pinches.” Journal of Physics: Conference Series 244 (2010): 032013.

**[Zier 2009]** Zier, J. C., J. D. Douglass, I. C. Blesener, K. S. Blesener, D. A. Chalenski, R. M. Gilgenbach, J. B. Greenly, D. A. Hammer, P. F. Knapp, B. R. Kusse, Y. Y. Lau, R. D. McBrode, W. Syed, and E. P Yu. “Azimuthally correlated ablation between Z-Pinch wire cores.” Physics of Plasmas 16, 102702 (2009).

# Appendix I - Publications

A.A. Anderson, V.V Ivanov, D. Papp, Visualization of the Magnetic Field and Current Path in Z-pinch and X-Pinch Plasmas, High Energy Density Physics (submitted)

V.V. Ivanov, A.A. Anderson, D. Papp, B.R. Talbot, J.P. Chittenden, N. Niasse, I.A. Begishev, UV laser-probing diagnostics for the dense z-pinch, IEEE TPS 42, 1123 (2014)

A.A. Anderson, V.V. Ivanov, D.Papp, B.R.Talbot, Study of Ablation and Implosion Stages of 1 MA Wire Array Z-Pinches Using UV Laser Diagnostics, Pulsed Power Conf. proc., 19th IEE 952-955 (2013)

V.V. Ivanov, D. Papp, A.A. Anderson, B.R. Talbot, A.L. Astanovitskiy, V. Nalajala, O. Dmitriev, J.P. Chittenden, N.Niasse, S.A. Pikuz, T.A. Shelkovenko, Study of micro-pinches in wire-array Z pinches Physics of Plasma 20, 112703 (2013)

S.D. Altemara, D. Papp, V.V. Ivanov, A.A. Anderson, A.A. Astanovitskiy, V. Nalajala, High-resolution UV Laser Diagnostics on the 1-MA Zebra Generator, IEE TPS 40, 3378 (2012)

V.V. Ivanov, J.P. Chittenden, R.C. Mancini, D.Papp, N. Niasse, S.D. Altemara, A.A. Anderson, Investigation of plasma instabilities in the stagnated Z Pinch, Physical Review E 00, 006400 (2012)

D. Papp, V.V. Ivanov, B. Jones, A. Haboub, A.A. Anderson, S.D. Altemara, B.R. Talbot, Physics of Plasmas 19, 092704 (2012)

V.V. Ivanov, P. Hakel, R.C. Mancini, J.P. Chittenden, A.A. Anderson, T. Durmaz et al., Measurement of the Ionization State and Electron Temperature of Plasma during the Ablation Stage of a Wire-Array Z Pinch Using Absorption Spectroscopy, Physical Review Letters 106, 225005 (2011)

V.V. Ivanov, P. Hakel, R.C. Mancini, J.P. Chittenden, A.A. Anderson, A.P. Shevelko, P. Wiewior, et al., X-ray absorption spectroscopy for wire-array Z-pinches at the non-radiative stage, High Energy Density Physics 7, 383-390 (2011)

V.V. Ivanov, J.P. Chittenden, S.D. Altemara, N. Niasse, P. Hakel, R.C. Mancini, D. Papp, A.A. Anderson, Study of the Internal Structure and Small-Scale Instabilities in the Dense Z Pinch, Physical Review Letters 107, 165002 (2011)

## Appendix II - Presentations

A.A. Anderson, V.V. Ivanov, A.L. Astanovitskiy, P. Wiewior, O. Chalyy, Study of the Ablation Stage Structure of 1-MA Wire Arrays with X-ray and UV Diagnostics, Oral Presentation at 9th International Conference on Dense Z-Pinches, Napa Valley CA, August 7th 2014

A.A. Anderson, V.V. Ivanov, D. Papp, B.R. Talbot, A.L. Astanovitskiy, Study of Ablation and Implosion Stages of 1-MA Wire Array Z-Pinch using X-ray Laser-Based Backlighting, Poster Presentation at 55th APS-DPP Annual Meeting, Denver CO, November 12th 2013

A.A. Anderson, V.V. Ivanov, D. Papp, B.R. Talbot, Study of Ablation and Implosion Stage of 1 MA Wire Array Z-Pinches using UV Laser Diagnostics, Oral Presentation at IEEE Pulsed Power & Plasma Science PPPS, San Francisco CA, June 19th 2013

A.A. Anderson, V.V. Ivanov, D. Papp, B.R. Talbot, Study of Ablation and Implosion Stages of Wire Array Z-Pinches using X-ray Imaging and UV Laser Diagnostics, Poster Presentation at Radiation of High Energy Density Plasmas International Workshop, Tahoe NV, April 3rd 2013

A.A. Anderson, D.Papp, S.D. Altemara, V.V. Ivanov, Study of Implosion in Wire Arrays with UV interferometry and Faraday Rotation Diagnostics, Poster Presentation at 54th Annual Meeting of the Division of Plasma Physics, Providence RI, October 30th 2012

A.A. Anderson, V.V. Ivanov, P. Hakel, R.C. Mancini, T. Durmaz, P. Wiewior, S.D. Altemara, D.Papp, A.L. Astanovitskiy, O. Chalyy, Development of Absorption Spectroscopy for Wire-Array Z-Pinches, Poster at Radiation from High Energy Density Plasmas Workshop, Reno NV, March17th 2011

A.A. Anderson, V.V. Ivanov, P. Hakel, R.C. Mancini, P. Wiewior, T. Durmaz, A.L. Astanovitskiy, O. Chalyy, S.D. Altemara, D.Papp, E. McKee, Development of absorption spectroscopy for wire-array Z-pinches, Poster Presentation at 52nd APS-DPP Annual Meeting, Chicago IL, Nov 10th 2010